Universität Hamburg
DER FORSCHUNG | DER LEHRE | DER BILDUNG

ALFRED-WEGENER-INSTITUT
HELMHOLTZ-ZENTRUM FÜR POLAR- UND MEERESFORSCHUNG

Master Thesis

Multi-Sensor Analysis of the Spatial and Temporal Variability of Snow-Free Land Surface Albedo on Disko Island, Greenland

vorgelegt von Jannika Gottuk

am 09.02.2024

Fakultät für Mathematik, Informatik und Naturwissenschaften
Fachbereich Erdsystemwissenschaften
Studiengang: M.Sc. Geographie
Matrikelnummer: 7075166

Angemeldeter Titel:

Multi-Sensor Analysis of the Spatial and Temporal Variability of Snow-Free Land Surface Albedo on Disko Island, Greenland

Betreuung am AWI:

Prof. Dr. Julia Boike

Dr. Simone M. Stuenzi

I acknowledge that I was able to conduct fieldwork on the ancestral land of the People of *Kalaallit Nunaat*, past and present and honour with appreciation the land itself and the *Kalaallit* People.

Abstract

Albedo – the reflectivity of a surface - is an important component in the energy budget, impacting the local to global climate. Data from nadir-viewing satellites can be combined with bidirectional reflectance distribution function (BRDF) data from multi-angular observation platforms to achieve realistic albedo values that acknowledge anisotropy. In my thesis, I evaluated how the land surface albedo varied on spatial and temporal scales during the snow-free period on Disko Island, Greenland. I examined how the albedo differed among the vegetation classes. Concerning the methodology, I assessed how the combination of MODIS BRDF data with Landsat 8 (L8) or Sentinel-2 (S2) influenced the albedo. The study area was located at the southern tip of Disko Island (69.27 °N, -53.47 °W) in West Greenland and covered a wetland and a range of tundra vegetation. I analysed automatic weather station (AWS) data from 2013 to 2022 and conducted mobile albedo measurements in August and September 2022 to examine the temporal and spatial variability. For the period from June to September 2022, I derived the L8 and S2 based albedo with inclusion of MODIS BRDF and narrow to broadband conversion and analysed their variability with regard to vegetation classes. In the snow-free period, the albedo increased from a monthly mean of 0.16 in June to 0.19 in September in the AWS data. The mobile measurements ranged from < 0.10 above bare soil and water to > 0.23 above areas dominated by lichen, *Salix glauca* or *Equisetum arvense*. The satellite-based albedo revealed temporally variable, significant correlations to normalised difference vegetation and moisture indices that reached values > 0.5 in the fen and wet heath class on several days. The albedo of shrubs was not notably smaller than other vegetation types but partly 0.01-0.05 above them in both the mobile measurements and the satellite-derived albedo. This finding challenges the assumption that shrubification causes climate forcing in all circumstances. The albedo of L8 and S2 differed to each other and the local data (root-mean-square error 0.04-0.14). The BRDF correction increased the albedo by 0.01 on average compared to nadir reflectance. L8 was better in reproducing the expected temporal and spatial variability of albedo than S2, which displayed less variability. S2 seemed to be more sensitive to atmospheric effects of haze and clouds influencing albedo. Thus, L8 seemed more suitable to calculate albedo in the study area. Though there were some methodological limitations, this thesis highlights aspects that should be considered when analysing albedo or jointly using L8 and S2 in high latitude regions.

Zusammenfassung

Die Albedo - das Reflexionsvermögen einer Oberfläche - ist eine wichtige Komponente im Energiehaushalt, die sich auf das lokale bis globale Klima auswirkt. Daten von Nadir-Satelliten können mit Daten der bidirektionalen Reflexionsverteilungsfunktion (engl. BRDF) von multi-angularen Beobachtungsplattformen kombiniert werden, um realistische Albedowerte zu erhalten, die Anisotropie berücksichtigen. In meiner Masterarbeit habe ich untersucht, wie sich die Albedo der Landoberfläche während der schneefreien Zeit auf der Disko Insel in Grönland räumlich und zeitlich verändert hat. Ich habe untersucht, wie sich die Albedo zwischen den einzelnen Vegetationsklassen unterscheidet. Was die Methodik betrifft, so bewertete ich, wie die Kombination von MODIS BRDF-Daten mit Landsat 8 (L8) oder Sentinel-2 (S2) die Albedo beeinflusste. Das Untersuchungsgebiet befand sich an der Südspitze der Insel Disko (69,27 °N, -53,47 °E) in Westgrönland und umfasste ein Feuchtgebiet und eine Reihe von Tundravegetation. Ich analysierte die Daten der automatischen Wetterstation (AWS) von 2013 bis 2022 und führte im August und September 2022 mobile Albedomessungen durch, um die zeitliche und räumliche Variabilität zu untersuchen. Für den Zeitraum von Juni bis September 2022 habe ich die L8- und S2-basierte Albedo unter Einbeziehung der MODIS BRDF und der Schmal-zu-Breitband-Konvertierung abgeleitet und ihre Variabilität in Bezug auf die Vegetationsklassen analysiert. In der schneefreien Zeit stieg die Albedo in den AWS-Daten von einem Monatsmittelwert von 0,16 im Juni auf 0,19 im September an. Die mobilen Messungen reichten von < 0,10 über vegetationslosem Boden und Wasser bis > 0,23 über von Flechten, *Salix glauca* oder *Equisetum arvense* dominierten Flächen. Die satellitengestützte Albedo zeigte zeitlich variable, signifikante Korrelationen zu normalisierten differenzierten Vegetations- und Feuchtigkeitsindizes, die in der Klasse der Niedermoore und feuchten Heiden an mehreren Tagen Werte > 0.5 erreichten. Die Albedo von Sträuchern war nicht nennenswert geringer als die anderer Vegetationstypen, sondern lag teilweise 0,01-0,05 darüber, sowohl bei den mobilen Messungen als auch bei der von den Satelliten abgeleiteten Albedo. Dieser Befund stellt die Annahme in Frage, dass die Strauchbildung unter allen Umständen eine Klimaerwärmung verursacht. Die Albedo von L8 und S2 wich voneinander und von den lokalen Daten ab (Wurzel des mittleren quadratischen Fehlers 0,04-0,14). Die BRDF-Korrektur erhöhte die Albedo im Durchschnitt um 0,01 im Vergleich zur Nadir-Reflexion. L8 reproduzierte die erwartete zeitliche und räumliche Variabilität der Albedo

besser als S2, das eine geringere Variabilität aufwies. S2 schien empfindlicher auf atmosphärische Effekte wie Dunst und Wolken zu reagieren, die die Albedo beeinflussen. Daher schien L8 für die Berechnung der Albedo im Untersuchungsgebiet besser geeignet zu sein. Obwohl es einige methodische Einschränkungen gab, zeigt diese Arbeit Aspekte auf, die bei der Analyse der Albedo oder der gemeinsamen Verwendung von L8 und S2 in Regionen mit hohen Breitengraden berücksichtigt werden sollten.

Contents

List of Figures

List of Tables

List of Abbreviations

6S Second Simulation of the Satellite Signal in the Solar Spectrum

ALG Atmospheric Look-up table Generator

AOI area of interest

AOT aerosol optical thickness

AppEEARS Application for Extracting and Exploring Analysis Ready Samples

ARTMO Automated Radiative Transfer Models Operator

ASTER Advanced Spaceborne Thermal Emission and Reflection Radiometer

AVHRR Advanced Very High Resolution Radiometer

AWS automatic weather station

BRDF bidirectional reflectance distribution function

DSM digital surface model

EROS Earth Resources Observation and Science

ESA European Space Agency

ETM+ Enhanced Thematic Mapper Plus

FoV field of view

GEM Greenland Ecosystem Monitoring

GlobAlbedo Global Land Surface Albedo from Satellite Data

GNSS global navigation satellite system

GOES Geostationary Operational Environmental Satellite

IPA International Permafrost Association

IPCC Intergovernmental Panel on Climate Change

IQR interquartile range

L8 Landsat 8

LAADS DAAC Level-1 and Atmosphere Archive & Distribution System Distributed Active Archive Center

LP DAAC Land Processes Distributed Active Archive Center

MERIS Medium Resolution Imaging Spectrometer

Meteosat Meteorological Satellite

MISR Multiangle Imaging SpectroRadiometer

MODIS Moderate Resolution Imaging Spectroradiometer

MSIL2A MultiSpectral Instrument Level 2A

NASA National Aeronautics and Space Administration

NDMI normalised difference moisture index

NDVI normalised difference vegetation index

NDWI normalised difference water index

NIR near-infrared

POLDER Polarization and Directionality of Earth's Reflectances

RMSE root-mean-square error

S2 Sentinel-2

SAGA System for Automated Geoscientific Analyses

SALSA Satellite Atmosphere correction & Land Surface Applications

SPOT Satellite pour l'Observation de la Terre

SWIR shortwave infrared

SWR shortwave radiation

SZA solar zenith angle

TDR time domain reflectometry

TOA top of atmosphere

TM Thematic Mapper

USGS United States Geological Survey

UTM Universal Transverse Mercator

VIS visible

vwc volumetric water content

WGS84 World Geodetic System 1984

List of Symbols

Footprint of Pyranometers

$\varnothing$ diameter

h pyranometer height

Satellite Products

b_i band number

lan Landsat

m MODIS

sen Sentinel

Spectral and Directional Parameters

$\bar{\alpha}$ albedo to nadir ratio

dir direct solar radiation fraction

R reflectance

ϕ relative azimuth in radians

ξ scattering angle in radians

Θ_s solar zenith angle in radians

SR surface reflectance

Θ_v view zenith angle in radians

λ wavelength

BRDF related Quantities

f BRDF parameter

geo geometric

iso isotropic

K kernel

vol volumetric

Albedo

α albedo

bl blue sky

bs black sky

ws white sky

Statistics

d mean absolute deviation

1 Introduction

Albedo – the reflectivity of a surface - is an important component in the energy budget, impacting the local to global climate. In the cryosphere, where the albedo ranges from < 0.1 for water to > 0.9 for fresh snow, it influences the energy budget of permafrost soils in complex ways (HUISSTEDEN 2020c; QIN et al. 2021b). During the snow-free period, the albedo is influenced by surface characteristics, e.g. soil moisture, water bodies and vegetation (HUISSTEDEN 2020c) and by external factors such as topography, clouds and SZA (QIN et al. 2021b). The proceeding climate change – rising temperatures and changing precipitation patterns – impacts surface characteristics and by that the albedo temperature feedback, which can amplify climate change (WALSH 2021).

In the remote Arctic, in-situ observations are limited but satellite remote sensing offers nearly continuous observations. Ready-to-use satellite albedo products are available for a low spatial resolution, e.g. from Moderate Resolution Imaging Spectroradiometer (MODIS) with 500 m resolution (SCHAAF and WANG 2021), which does not represent the albedo variability of snow-free heterogeneous landscapes. Currently, freely available satellite imagery with higher resolution such as Landsat 8 (L8) (30 m) and Sentinel-2 (S2) (10-20 m) are near nadir-viewing (European Space Agency (ESA) 2015; United States Geological Survey (USGS) 2019). Using only these observations would assume a Lambertian, isotropic reflectance, which is not realistic and leads to biases, especially in high-latitude regions with low sun elevation angles (TOMASI et al. 2020). To solve the problem of missing anisotropy information, SHUAI et al. (2011) developed an approach which combines MODIS bidirectional reflectance distribution function (BRDF) data with Landsat Enhanced Thematic Mapper Plus (ETM+) reflectance data in order to calculate albedo in Landsat resolution. Other authors applied this method globally and with newer Landsat generations or S2. Additionally, the combination of Landsat and Sentinel became of increasing interest to produce longer time series (FENG et al. 2023) or higher spatiotemporal resolutions (WILLIAMSON et al. 2018).

Most studies of albedo in the Arctic focus on snow and ice albedo. To my knowledge, no study compared the albedo of snow-free tundra landscapes of L8 and S2 in combination with MODIS BRDF yet. This thesis fills this gap and contributes to the understanding of albedo processes in heterogeneous Arctic landscapes characterised by a high SZA and frequent cloud cover. It tackles the general questions *How does land surface albedo*

vary on spatial and temporal scales during the snow-free period in the most southern tip of Disko Island, Greenland? and *How do L8 and S2 based albedo combined with MODIS BRDF data contribute to our understanding of albedo in a low Arctic region?*. For that, I investigate the following questions:

1. How does albedo vary interseasonally and interannually in the automatic weather station (AWS) data and how does the cloud cover influence the albedo in the snow-free period?
2. How does albedo change with varying vegetation cover (colour, structure, composition) in the Albedometer data?
3. Which temporal and spatial patterns of albedo can be detected with the satellite data and to what extent can these patterns be explained by remote sensing vegetation and moisture indices?

Based on the research questions, I expect that the albedo shows a strong interseasonal variability in the AWS data linked to snow cover and a smaller variability in the snow-free period, which is biased by cloud cover. Though small interannual changes of albedo over time might occur, I expect those to be not significant in the limited data. As the landscape is characterised by wetland and different vegetation, I presume the albedo of the field data and satellite imagery to be in the range of < 0.1 to > 0.2 with a median < 0.2. I expect that the L8 and S2 based albedo follow the seasonal pattern of the AWS data and display spatial differences influenced by vegetation and moisture, which can be explained by remote sensing indices to a limited extent. I expect that the BRDF correction slightly increases albedo. However, I hypothesise that the L8 and S2 based albedo display differences due to deviant sensor specifications and spatial resolution, where I expect L8 to vary less due to its lower spatial resolution.

This thesis is structured as follows. Chapter 2 gives background information on Arctic permafrost, how albedo influences the climate and how it is influenced by environmental factors, and what methodological aspects are important. In Chapter 3, I introduce the study area and explain my methodology. This includes the AWS data set, the data collection of mobile measurements, the workflow of the satellite-derived albedo and the statistical analysis. Then, I present the results in Chapter 4 and interpret and discuss these in Chapter 5, including methodological limitations. In the end, I draw a conclusion in Chapter 6.

2 State of the Art

2.1 Permafrost in the Arctic

The Arctic can be defined and described under various aspects. In a formal way, it is the region polewards of the northern polar circle at approximately 66.5 °N (SERREZE and BARRY 2014) and thus characterised by the presence and absence of sun light for at least one day during the year, called polar day and polar night, respectively. Their lengths increase towards the pole and influence the climate conditions. However, arctic conditions are also present south of 66.5 °N, so that other, less strict definitions are commonly used, e.g. the transition zone of the treeless tundra to the boreal forest, also called tundra-forest ecotone, which correlates with the 10 °C July isotherm (SERREZE and BARRY 2014; HUISSTEDEN 2020a).

In general, the Arctic has a large seasonal and spatial climatic variability but is broadly divided into the High and Low Arctic. As part of the cryosphere, snow and ice cover play an important role in the climate. Since this thesis approaches the albedo of snow-free land surfaces, the focus of the thematic background is on the snow-free season and land surface. The High Arctic or polar desert is characterised by extremely cold temperatures, a lack of moisture and thus only very little vegetation (SERREZE and BARRY 2014). The Low Arctic has less extreme conditions and allows tundra vegetation. The generally increasing temperature gradient from the north pole to the south influences the possibility of permafrost by reducing the spatial coverage, displayed in Figure 1.

Permafrost, a composite of permanent and frozen, as defined by the International Permafrost Association (IPA) refers to ”ground [...] that remains at or below 0 °C for at least two consecutive years” (IPA n.d.). It is estimated that 12.8 - 17.8 % of the northern hemisphere land area are underlain by permafrost with the largest share in the Arctic, followed by the Tibetan Plateau and several mountain ranges (ZHANG et al. 2000; HUISSTEDEN 2020a). Due to regular freeze-thaw processes, Arctic permafrost regions are associated with specific surface features, e.g. mudboils, hummocks and patterned ground (HUISSTEDEN 2020a). Large wetlands can form in flat terrain, because the frozen layer hinders draining (SERREZE and BARRY 2014). As a subsurface feature, satellite remote sensing cannot detect permafrost directly. However, it can be assessed indirectly by identifying typical surface features or analysing physical variables that are

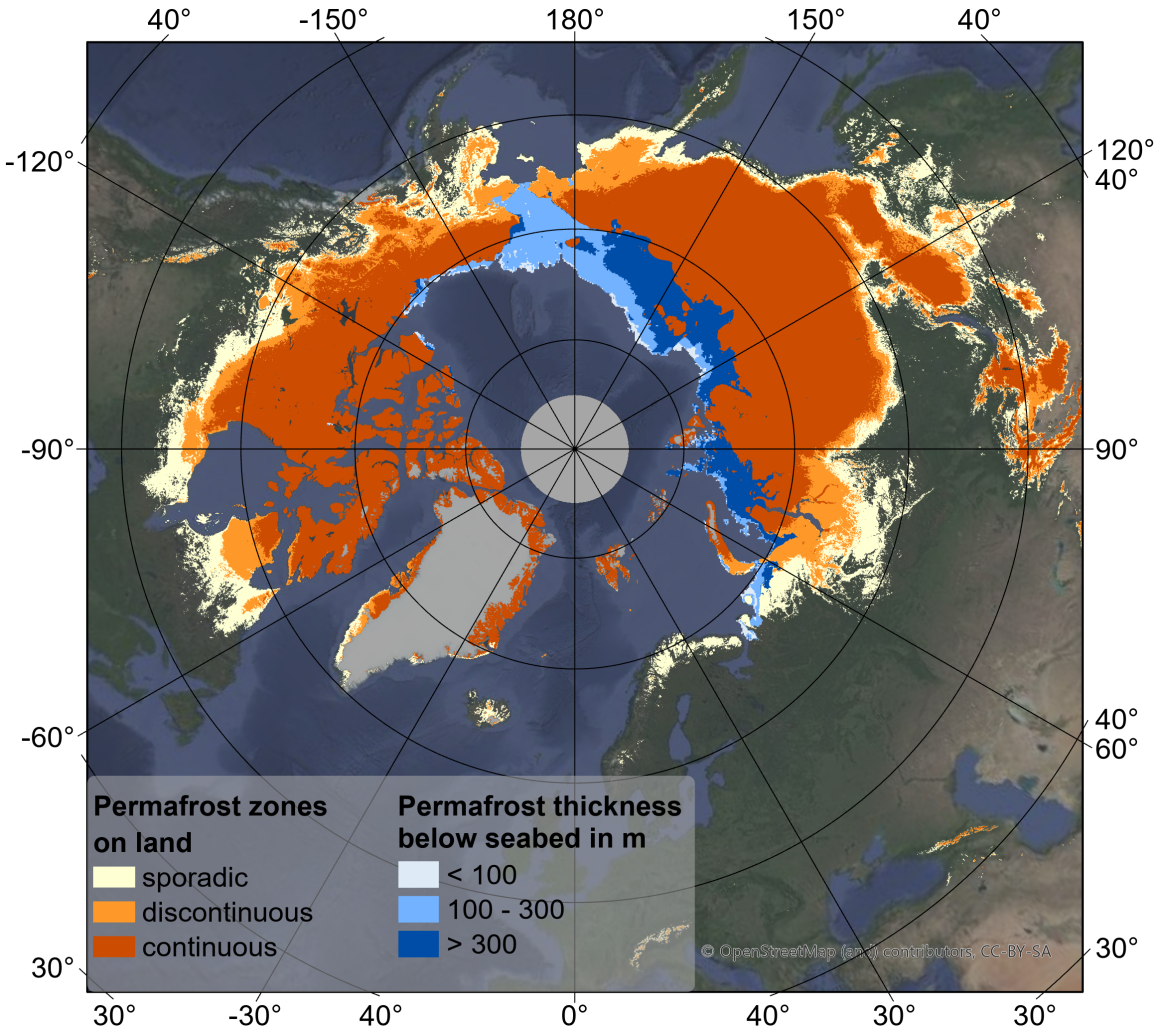

Figure 1: Modelled permafrost in the Arctic. In the style of GRID-ARENDAL/NUNATARYUK (2020). The permafrost zones on land by OBU et al. (2018) are classified based on the share underlain by permafrost: sporadic 10 - 50 %, discontinuous 50 - 90 % and continuous > 90 %. Submarine permafrost zones from OVERDUIN et al. (2020) < 100 m are uncertain, between 100 and 300 m probable and > 300 m confident. Basemap: GOOGLE EARTH and OPENSTREETMAP CONTRIBUTORS (2023).

linked to permafrost (WESTERMANN et al. 2015).

The extent of permafrost currently depends on the heat energy penetrating into the ground. Permafrost is overlain by the active layer that thaws and refreezes during the year (HUISSTEDEN 2020a). The depths of both layers are a result of the energy balance of the soil, which depends on various elements: the radiation balance and latent, sensible and convective heat fluxes at the surface, the insulating properties of vegetation and snow cover as well as ground and lateral heat fluxes in the soil column (HUISSTEDEN 2020c). The surface albedo influences how much of the solar radiation is available to heat the ground. The net effects of latent, sensible and convective heat

fluxes are influenced by the availability of water, surface roughness and atmospheric conditions (HUISSTEDEN 2020c). Generally, vegetation has a cooling effect, while snow has a warming effect on the soil (HUISSTEDEN 2020c). The strength of ground and lateral heat fluxes is influenced by soil thermal properties and lateral heterogeneity of the soil column (HUISSTEDEN 2020c). Taking all these elements into account, permafrost is not stable but vulnerable to climate change.

Climate change is present in the Arctic. Various studies imply that the region has warmed two to nearly four times faster than the global average, also referred to as Arctic Amplification (RANTANEN et al. 2022). This warming led to changes in vegetation composition and permafrost thaw with a temperature increase of $0.39 \pm 0.15\,°C$ in the arctic permafrost layer of the continuous zone between 2007 and 2016 (BISKABORN et al. 2019). Vegetation changes include shrub expansion (shrubification) and greening and browning trends meaning an increase and decrease in vegetation coverage above ground, respectively (HUISSTEDEN 2020d). Of global concern are greenhouse gases that are released when the ground thaws and microbial activity decomposes organic matter. However, the carbon storage in permafrost is spatially heterogeneous (HUISSTEDEN 2020b) and the effects of greenhouse gas release from permafrost are sometimes exaggerated in the media. Based on assessments from the Intergovernmental Panel on Climate Change (IPCC), there are large uncertainties when and to what extent greenhouse gases from permafrost will contribute to warming in the 21st century and it is expected that the amount is rather small compared to anthropogenic emissions (CANADELL et al. 2021). For the local population it is more acute that the thawing permafrost affects the stability of the ground and thus causes erosion, thaw slumps and infrastructure damage (HUISSTEDEN 2020a; SERREZE and BARRY 2014).

2.2 Land Surface Albedo in the Energy Budget

The term albedo is used for different specific parameters. It is generally defined as the ratio of outgoing to incoming radiation fluxes. In many cases, the term albedo is used for the broadband shortwave blue sky albedo, referencing to the reflectivity of combined direct and diffuse radiation for the shortwave spectrum. The exact spectral range varies in the literature, but lies between 0.25 -0.4 µm and 2.5 -5 µm (KOKHANOVSKY 2021; LIANG 2001; LUCHT et al. 2000). Radiation fluxes outside this range are very small and can be

neglected for the calculation of albedo. The characteristics of the spectral albedo at narrow wavelengths vary for different surfaces (LIANG 2001). Thus, it can be interesting to look at the visible (VIS) (0.3 - 0.7 µm) or infrared (0.7 - 5 µm) albedo separately (LUCHT et al. 2000). The blue sky albedo is the combination of the directional hemispherical reflectance (black sky albedo) and the diffuse bihemispherical reflectance (white sky albedo) based on the proportion of direct and diffuse radiation (SALOMON et al. 2006). In this thesis, I use the term albedo for the broadband shortwave blue sky albedo if not specified otherwise.

The albedo of a surface is an important component in the energy budget of the Earth, thereby impacting the local to global climate. In the research fields of climate and the cryosphere, albedo is most commonly studied in the context of the snow and ice albedo feedback. Because snow- and ice-covered surfaces have higher albedo compared to snow- and ice-free surfaces, snow and ice alter the energy absorption of a surface significantly (QIN et al. 2021a). According to modelling results of PITHAN and MAURITSEN (2014) the snow and ice albedo feedback is the second largest contributor to Arctic Amplification. As the feedback is sometimes overemphasised or cited as the main contributor, I want to highlight that the feedback only acts when sunlight is present and that various model runs showed that Arctic Amplification also occurred when this feedback was eliminated (PITHAN and MAURITSEN 2014; PREVIDI et al. 2021).

The linkage of albedo of snow- and ice-free surfaces and climate is more complex and associated with large uncertainties. In the last decade, this was increasingly investigated in the Arctic and in high latitude boreal forests with a focus on vegetation changes (JUSZAK et al. 2014; WANG, ERB, et al. 2016; STUENZI and SCHAEPMAN-STRUB 2020; PLEKHANOVA et al. 2022). On a local scale, vegetation changes above ground showed a strong correlation with the normalised difference vegetation index (NDVI), but only small correlations were found with albedo (JUSZAK et al. 2014; PLEKHANOVA et al. 2022). Vegetation disturbances such as fires led to seasonal increases of albedo (WANG, ERB, et al. 2016; STUENZI and SCHAEPMAN-STRUB 2020) with an annual negative forcing in boreal forests (STUENZI and SCHAEPMAN-STRUB 2020). On a pan-Arctic scale, most areas (82 %) did not change significantly in mid-summer albedo based on a MODIS analysis for 2000-2021, while 14 % increased and 4 % decreased (PLEKHANOVA et al. 2022). However, land surface models failed to depict the observed seasonal trends

and changes (ZHANG et al. 2019; PLEKHANOVA et al. 2022). And though fires led to increased albedo with negative forcing, they could cause further processes with higher climate forcing potential (STUENZI and SCHAEPMAN-STRUB 2020). Thus, it is relevant to understand the complex interaction of snow- and ice-free surfaces, albedo and climate forcing at various spatial scales in order to properly depict and integrate albedo in models and climate management decisions (STUENZI and SCHAEPMAN-STRUB 2020; PLEKHANOVA et al. 2022).

Besides vegetation, there are further surface characteristics and factors independent from the surface that affect the albedo of snow- and ice-free surfaces. The albedo of vegetated areas varies depending on colour, height, canopy complexity and leaf area of the vegetation (JUSZAK et al. 2014; STUENZI and SCHAEPMAN-STRUB 2020; PLEKHANOVA et al. 2022). In areas without or with only sparse vegetation, water cover and soil type, colour and moisture mainly influence the albedo (QIN et al. 2021b). A surface, which is assumed to have a constant albedo dependent only on surface characteristics, is referred to as a Lambertian surface (WANG, ERB, et al. 2016). However, most surfaces in nature reflect anisotropically, meaning dependent on the illumination geometry including view zenith angle and SZA (WANNER et al. 1997), where SZAs > 70 ° cause higher uncertainties (WANG et al. 2012). Both angles affect the path of the solar radiation through the atmosphere and how it is scattered and absorbed. Thus, also clouds, the atmospheric state as well as surface roughness and slopes influence the albedo (GRENFELL 2011; GALLET et al. 2011).

2.3 Measuring and Calculating Albedo

As a radiation parameter, albedo can be measured or approximated with remote sensing. Its basic principle is that a sensor receives a signal, which allows a conclusion about the properties of the object, without being physically in contact with it (TEDESCO 2015). These sensors are installed or operated in the field or collect data attached to air- or spaceborne observation systems. Satellite remote sensing is a common technique in meteorological and geoscientific research. In remote places, such as the Arctic, satellite remote sensing has the advantage of offering nearly continuous observations of a larger area with relatively little effort and costs needed. The number of satellites in orbit has increased and their technical possibilities developed greatly since the launch

of the first weather satellite in 1959 (WENDISCH et al. 2021). However, satellite data are biased and do not reflect reality. Thus, field measurements are useful and necessary for validating satellite-based albedo (SALOMON et al. 2006).

In the field, albedo can be measured with two identical pyranometers facing up- and downwards in order to receive signals for incoming and outgoing radiation (HUKSEFLUX 2002). Measurements should be made over a flat surface without obstacles because objects between the sun and sensors and topographic features influence the radiation that reaches the sensors (WORLD METEOROLOGICAL ORGANIZATION 2018). Pyranometers can be part of an AWS and record data regularly, which is useful for the analysis of temporal variability. Working with data from already established AWS pyranometers, e.g. from the Baseline Surface Radiation Network from the World Radiation Monitoring Center (ALFRED WEGENER INSTITUTE, HELMHOLTZ CENTRE FOR POLAR AND MARINE RESEARCH 2022) has the advantage of low costs and effort being necessary. Furthermore, the chances of having ”good”, clear-sky data increase when a time series is available. This time series can be analysed for e.g. hourly, daily, seasonal and interannual variability. However, AWS data do not offer insight into the spatial variability of an area, which can be achieved by mounting the pyranometers on a mobile system. This has the disadvantage of costs and time effort needed and the dependence on weather conditions. Therefore, the combination of stationary AWS data over time with spatially distributed measurements is advantageous to analyse the albedo of a region.

There are a number of ready-to-use satellite-based albedo data products. Examples include the Satellite Application Facility on Climate Monitoring from the *Deutscher Wetterdienst* based on Advanced Very High Resolution Radiometer (AVHRR) and Meteorological Satellite (Meteosat) data (DEUTSCHER WETTERDIENST 2021), the Global Land Surface Albedo from Satellite Data (GlobAlbedo) project from the ESA based on Medium Resolution Imaging Spectrometer (MERIS) and VEGETATION instruments on board Satellite pour l’Observation de la Terre (SPOT) (ESA 2020) and MODIS from National Aeronautics and Space Administration (NASA) (SCHAAF and WANG 2021). However, their spatial resolution with at least 500 m is low and not suitable for research questions at the landscape scale. Satellite missions with higher spatial resolution, such as L8 and S2, have a sun-synchronous orbit and are near-nadir viewing. This means that they are aligned to the Earth’s surface with an inclination

angle close to 90 ° and overfly each point at a similar local time with consistent lighting conditions (ESA 2015; USGS 2019). Therefore, analysing albedo solely with L8 or S2 does not yield realistic results, because anisotropy cannot be assessed with the lack of multi-angular observations (LI et al. 2018).

One approach to account for anisotropy effects is the BRDF, which models the reflectance as a function of illumination and viewing geometry. The kernel-driven BRDF model used by MODIS is described as

$$R_\lambda(\Theta_s, \Theta_v, \phi) = f_{iso,\lambda} + f_{vol,\lambda} \cdot K_{vol}(\Theta_s, \Theta_v, \phi) + f_{geo,\lambda} \cdot K_{geo}(\Theta_s, \Theta_v, \phi) \tag{1}$$

where the reflectance (R) at a wavelength (λ) can be calculated for varying SZA (Θ_s), view zenith angle (Θ_v) and relative azimuth (ϕ) (SHUAI et al. 2011). In the model, R is the sum of three scattering types represented as kernel (K) (STRAHLER et al. 1999). The BRDF parameters (f) describe the isotropic (iso) scattering component and the volumetric (vol) and geometric (geo) coefficients for the kernel. The effects that different surfaces can exert on reflection and scattering are displayed schematically in Figure 2.

SHUAI et al. (2011) developed a workflow that combines MODIS BRDF data with Landsat ETM+ surface reflectance for the retrieval of surface albedo in Landsat spatial resolution. Since then, the approach has been applied to and tested with L8 and S2 (LI et al. 2018; SONG et al. 2021; YANG et al. 2021). The basic assumption is, that the albedo to nadir ratio ($\bar{\alpha}$) of anisotropy-including albedo and surface reflectance at nadir view is approximately identical for all satellite platforms MODIS (m), Landsat (lan) and Sentinel (sen)

$$\bar{\alpha}_\lambda \approx \frac{\alpha_{m,\lambda}}{R_{m,\lambda}} \approx \frac{\alpha_{lan,\lambda}}{R_{lan,\lambda}} \approx \frac{\alpha_{sen,\lambda}}{R_{sen,\lambda}} \tag{2}$$

(SHUAI et al. 2011). Thus, the spectral albedo in L8 and S2 spatial resolution can be derived by multiplying their surface reflectance with $\bar{\alpha}_{m,\lambda}$ at L8 or S2 overpass time (SHUAI et al. 2011).

Based on the spectral albedo, many studies (SHUAI et al. 2011; TRAVERSA et al. 2021; WANG, ERB, et al. 2016; BONAFONI and SEKERTEKIN 2020; LI et al. 2018) apply a method called narrow to broadband conversion to compute the broadband albedo, which has been tested extensively by LIANG (2001). With radiative transfer simulation, for several atmospheric conditions and 256 surface reflectance spectra of differ-

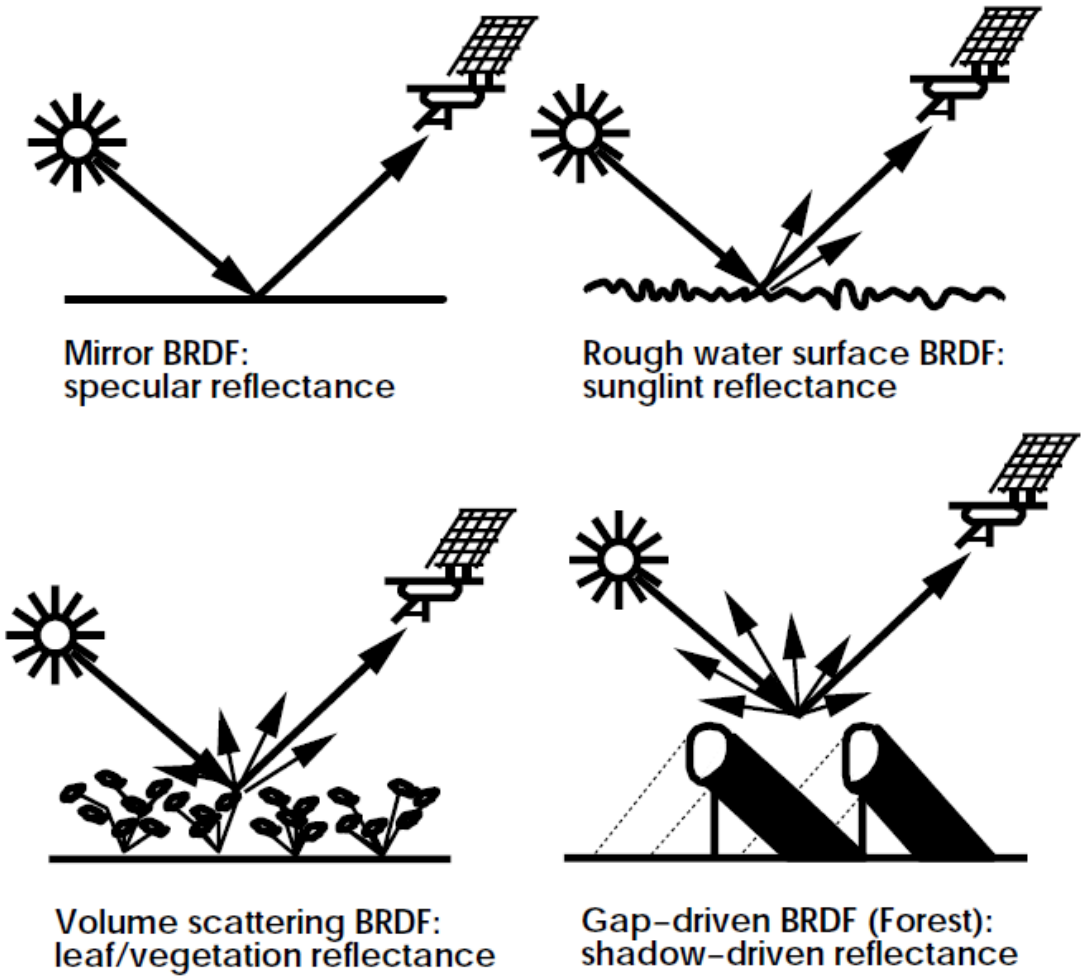

Figure 2: Reflection and scattering of different surfaces (STRAHLER et al. 1999, p. 45).

ent surfaces, LIANG (2001) calculated linear regression coefficients for several satellite platforms. When applying the linear conversion formula to the spectral albedo, the satellite bands are weighted according to the empirical relationship found in the simulations. MODIS yielded the best results in the narrow to broadband conversion, followed by Landsat ETM+, in comparison with Advanced Spaceborne Thermal Emission and Reflection Radiometer (ASTER), AVHRR, Geostationary Operational Environmental Satellite (GOES), Multiangle Imaging SpectroRadiometer (MISR), Polarization and Directionality of Earth's Reflectances (POLDER) and the VEGETATION instruments on board SPOT (LIANG 2001). Since then, other studies computed narrow to broadband conversion coefficients for newer Landsat platforms and S2 for snow-covered and snow-free surfaces (WANG, ERB, et al. 2016; LI et al. 2018).

3 Methodology

In my thesis, I used several software. I analysed the AWS, Albedometer and satellite imagery data with own code scripts in a RStudio environment version 2022.12.0.353 (POSIT TEAM 2022) with R version 4.2.1 (R CORE TEAM 2022). For the satellite imagery processing and the spatial analysis, I used the software System for Automated Geoscientific Analyses (SAGA) (CONRAD et al. 2015), version 9.2.0, which I executed through own code scripts in R with the RSAGA package (BRENNING et al. 2022). The determination of the share of direct radiation involved the 6S code (VERMOTE et al. 1997), version 2.1 provided by Satellite Atmosphere correction & Land Surface Applications (SALSA), which I executed through the Atmospheric Look-up table Generator (ALG) graphical user interface software (VICENT et al. 2020), version 3.2.2 provided by Automated Radiative Transfer Models Operator (ARTMO). I created all maps with ArcGIS Pro (ENVIRONMENTAL SYSTEMS RESEARCH INSTITUTE 2024), version 3.1.0, and all other figures in the results section in R.

3.1 Study Area

The AOI is located in the south of Disko Island in West Greenland (69.23 – 69.30 °N, 53.42 – 53.63 °W). It encompasses the Arctic Station (University of Copenhagen, arktiskstation.ku.dk) and Østerlien in the east of Qeqertarsuaq and the south of *Kuup Ilua*, also called Blæsedalen Valley (Figure 3). Disko Island has a volcanic origin and its geology is influenced by basaltic rock (CHALMERS et al. 1999) so that the soil is dark.

Disko Island is underlain by discontinuous permafrost and hosts a comparably high biodiversity for polar conditions. The vegetation of *Kuup Ilua* is characterised by dwarf birch (*Betula nana*), grayleaf willow (*Salix glauca*), bog blueberry (*Vaccinium uliginosum*, hereafter *Vaccinium*), black crowberry (*Empetrum nigrum*), Arctic white heather (*Cassiope tetragona*, hereafter *Cassiope*), mosses and lichens. Only in few areas, vegetation height exceeds 0.5 m. In contrast to many Arctic places, the island offers a good water supply for Flora and Fauna through rivers fed by melt water and springs. The hydrology of the AOI is influenced by the river *Kuussuaq* (also called red river) flowing through it from north to south and a lake and wetland north of Transect 1.

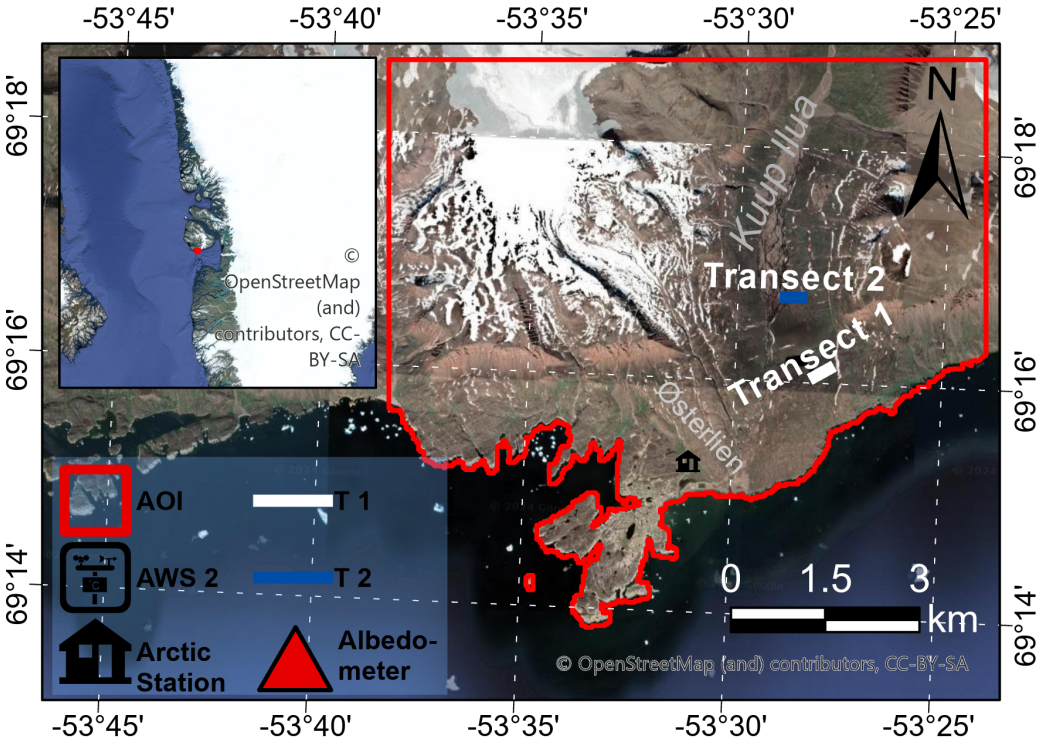

(a) Overview of the study sites *Kuup Ilua* North and South and the Arctic Station in the southern part of Disko Island. The inset map shows the AOI location within Greenland.

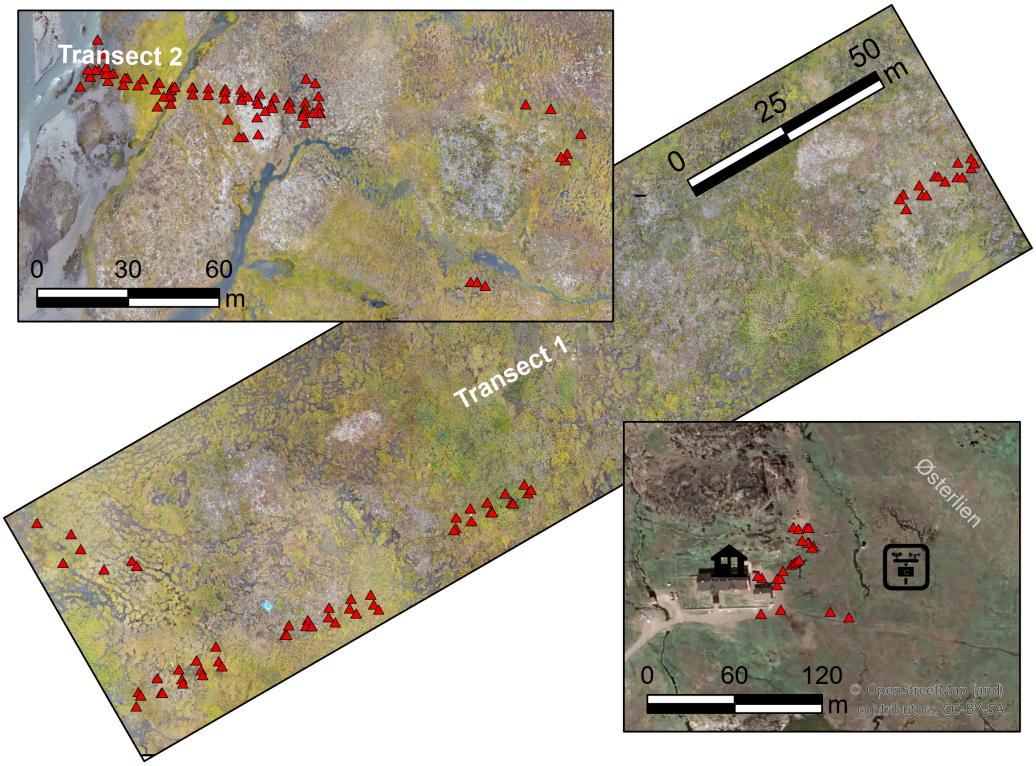

(b) Location of the Albedometer measurements at the study sites.

Figure 3: The study sites on Disko Island, Greenland. Basemaps: (a) and Arctic Station in (b): GOOGLE EARTH and OPENSTREETMAP CONTRIBUTORS (2023); Transects: drone imagery recorded on 7th (T2) and 8th (T1) September 2022 (SIMONE M. STUENZI and JENNIKA HAMMAR, orthoimage created with Pix4D).

Disko Island has a low-arctic, maritime climate. The mean annual air temperature measured at the Arctic Station AWS1 was - 3.0 $\pm$ 1.8 °C for 1991-2017 (ZHANG et al. 2019). The seasonal mean temperatures varied between - 12.5 $\pm$ 3.9 °C in winter (December-February) and 6.8 $\pm$ 1.3 °C in summer (June-August) (ZHANG et al. 2019). The snow period usually lasts from October to May, with a large interannual variation of snow thickness and timing of snow onset and melt (HOLLESEN et al. 2015). Due to the high latitude, the sunshine duration varies throughout the year with a long daily duration at low sun elevation angles in summer time. From 1994 to 2006, the measured mean annual rainfall was 273 $\pm$ 100 mm, which was estimated as roughly 60 % of the total precipitation (HOLLESEN et al. 2015).

Climatic changes have been recorded on the island. In the period of 1991-2017, ZHANG et al. (2019) observed a significant increase in annual air temperature of 1.6 °C per decade with a more pronounced warming in winter (3.2 °C per decade) than in summer (1.1 °C per decade). The mean annual precipitation decreased by 24% from the period 1991-2000 to 2008–2017 (ZHANG et al. 2019). For the people of Qeqertarsuaq, changes became perceptible through decreasing sea ice cover duration and stability as well as increasing extreme weather conditions, which led to aggravated access to the island and limited and more dangerous hunting opportunities (FORD and GOLDHAR 2012). In 2022 for example, the summer and autumn periods were unusually rainy in the Disko Bay area with 288.1 mm liquid precipitation measured at the Teleø AWS in Qeqertarsuaq in September, compared to a monthly average of 34.3 $\pm$ 20.5 mm in September of 2010-2021 (Data: Greenland Ecosystem Monitoring (GEM) 2023a). The response of the vegetation and soil to climate change was studied extensively with gas flux measurements and warming experiments in *Kuup Ilua*. In experiments from D'IMPERIO et al. (2018), summer warming led to an increase in the quantity and length of roots, while increased winter precipitation was followed by a decreased root diameter indicating that climatic changes might lead to altered species composition. *Betula nana* growth was correlated positively with temperature in the last century, especially with winter and spring soil temperatures (HOLLESEN et al. 2015). Thus, the species could benefit from early snow melt and contribute to Arctic greening.

3.2 Local Albedo Data

Automatic Weather Station Data

The GEM programme currently operates one AWS, called AWS2, which measures both incoming and outgoing SWR and is located about 100 m east of the Arctic Station. The CNR4 net radiometer (field of view (FoV): upwards 180 °, downwards 150 ° (CAMPBELL SCIENTIFIC 2024)) is mounted 3 m above the surface (SIGSGAARD 2022) with low heath vegetation, dominated by grasses, *Betula nana* and *Salix glauca* (Figure 4). A SR50 Sonic sensor records snow depth as a point measurement (SIGSGAARD 2022; GEM 2023d). The data are logged in 30-minutes intervals. At the time of my analysis, AWS2 data were available from November 2012 to December 2022. Cloud cover data were available from June 1993 until April 2020. The visual cloud observations were conducted from the Arctic Station at 7 am, 12 pm and 5 pm (GEM 2023b). I downloaded

(a) AWS2 near the Arctic Station. The pyranometer in (b) is mounted on the right end of the horizontal pole, 15th September 2023.

(b) Pyranometer of AWS2: CNR4 net radiometer, 15th September 2023.

(c) *Betula nana* with green leaves, 24th August 2022.

(d) *Betula nana* with red leaves, 8th September 2022.

(e) *Betula nana* with reddish brown leaves, 8th September 2022.

Figure 4: The AWS2 (a) and its pyranometer (b) in Østerlien. The ground is partly covered by *Betula nana* that changes its colours markedly in autumn. Photos (c) to (e) depict these different colours, which the species had in the study area around the time of the Albedometer measurements.

the data from the GEM website after registration (GEM 2023c) and processed it in R. I excluded the winter months in 2012 as the year was incomplete. A data gap of 5 days due to maintenance in September 2022 did not influence my evaluation because it was not during the period of my satellite data analysis.

Collection of Field Data with the Albedometer

Between 29th August and 8th September 2022, I collected albedo data with a mobile Albedometer along two transects and around the Arctic Station (Figure 3). The field work took place in the broader context of the project MOMENT (Permafrost Research Towards Integrated Observation and Modelling of the Methane Budget of Ecosystems). Table 1 lists details of measurement sites and observation dates. I estimated the SZA with the solar calculator from the National Oceanic and Atmospheric Administration (NATIONAL OCEANIC AND ATMOSPHERIC ADMINISTRATION GLOBAL MONITORING LABORATORY 2024). In total, I conducted 1434 measurements at 170 data points. Additional field data collected at selected points included characteristics of soil and vegetation, soil temperature and time domain reflectometry (TDR) measurements (TDR, HydroSense II, Campbell Scientific Ltd.) of soil volumetric water content (vwc). For two days, the weather condition of total cloud cover was unfavorable for measuring albedo.

The portable Albedometer was designed by William Cable. It recorded the location with a global navigation satellite system (GNSS) module and measured incoming and outgoing SWR with two SRA01 Hukseflux sensors. The GNSS antenna and the sensors were linked to the logger box containing the battery and data logger with a pole.

Table 1: Overview of the collected albedo field data from Disko Island, Greenland in 2022.

Date	Site Name	Local Time (start/end)	SZA in ° (start/end)	Est. Cloud Coverage	Transect	Data Points
29. Aug	Arctic Station	12:05 12:57	61.8 60.3	100 %	-	24
30. Aug	*Kuup Ilua* North	15:17 16:24	62.7 66.3	< 5 %	2 -	45 34
8. Sep	*Kuup Ilua* South	12:28 14:22	64.5 64.3	100 %	1 -	60 7

A connected smartphone allowed me to view the current measurement and to edit the sample name and number. As second-class pyranometers, the SRA01 Hukseflux sensors were classified with the third highest accuracy in the ISO 9060 - 1990 standard “Solar energy - specification and classification of instruments for measuring hemispherical solar and direct solar radiation”, which is suitable for scientific research (HUKSEFLUX 2002). The sensors consisted of a black coated thermal sensor and a glass dome. The signal was received from a FoV angle of almost 180 °. The solar irradiance was calculated automatically as the quotient of the sensor voltage output and the sensitivity (HUKSEFLUX 2002). During measurements, I aligned the Albedometer horizontally with the aid of bubble levels with the sensors oriented between the sun and myself (Figure 5). The sensor was at a height of about 0.83 m. When I loaded the data into the software SAGA, I noticed an offset of the points in *Kuup Ilua* North compared to the Google Satellite basemap. Thus, I edited the x-coordinates and moved all points in *Kuup Ilua* North 12 m to the east.

(a) Albedo measurements at Transect 2, 30th August 2022.

(b) SRA01 sensors.

Figure 5: The Albedometer and its sensors for field data collection. Photo credit: (a) Niko Bornemann. (b) HUKSEFLUX (2002).

Footprint of Pyranometers

The sensing area (”footprint”) of the Albedometer and the AWS2 is assumed as a circle, whose diameter ($\varnothing_{footprint}$) is dependent on the pyranometer height (h) and FoV and can be approximated by Equation 3 (EICHLER 2022).

$$\varnothing_{footprint} = 2 \cdot h \cdot \tan(\frac{FoV}{2}) \tag{3}$$

With a height of 3 m and a FoV of 150 °, the AWS2 footprint had a maximum diameter of 22.39 m and a maximum area of 393.72 m². Likely, the footprint was smaller due to limitations in manufacturing (WU et al. 2018). However, I could not find the sensor's effective half FoV for both the AWS2 and Albedometer. Studies with other sensors with a downwards FoV of 180 ° assumed an effective half FoV of 81 ° (EICHLER 2022; SONG et al. 2019). For the Albedometer with a height of 0.83 m, this resulted in a footprint with a diameter of 10.48 m and an area of 27.46 m².

3.3 Derivation of Satellite-based Albedo and Indices

In this thesis, I combined L8 and S2 surface reflectance with MODIS BRDF data for the derivation of the albedo of snow-free land surfaces in L8 and S2 spatial resolution. All satellite data were available free of charge after registration at the respective websites. Because Landsat had the lowest temporal resolution, I began with the download of the L8 Collection 2 Level 2 data from the USGS EarthExplorer (USGS 2022). I selected several scenes from mid June to the end of September with the lowest cloud cover possible over the AOI based on visual inspection. Then, I downloaded the S2 MultiSpectral Instrument Level 2A (MSIL2A) from the Copernicus Open Access Hub (COPERNICUS 2022a) with dates close to the L8 data and visually-determined low cloud cover. In the summer months of 2023, the Copernicus Open Access Hub stopped its service and S2 data became fully available on the Copernicus Data Space Ecosystem (COPERNICUS 2022b), where I downloaded additional S2 data after extending the initial observation period. Table 2 gives an overview of the acquisition dates and the spatial resolution of the imagery data used. These L8 and S2 surface reflectance data were atmospherically corrected and came in Universal Transverse Mercator (UTM) projection. I chose existing narrow to broadband conversion coefficients that required all VIS, the near-infrared (NIR), and both shortwave infrared (SWIR) bands. Details of the spectral resolution and the band numbers of each satellite product are listed in the Appendix in Table 8.

The BRDF data were available for all L8 and S2 dates at NASAs Application for Extracting and Exploring Analysis Ready Samples (AppEEARS) website (NASA 2023a). The MODIS MCD43A1 product MODIS/Terra+Aqua BRDF/Albedo Model Parameters Daily L3 Global, version 6.1 offered the three BRDF parameters for all necessary bands

Table 2: Overview of the satellite imagery data with acquisition dates, SZA and spatial resolution (USGS 2019; ESA 2015; Land Processes Distributed Active Archive Center (LP DAAC) n.d.).

	L8	S2	MODIS	SZA
	DD.MM.YYYY		Day of Year	Θ_s in degree
	19.06.2022	19.06.2022	170	46.3 | 45.5
	28.06.2022	28.06.2022	179	46.4 | 45.6
	05.07.2022		186	47.0
		08.07.2022	189	46.5
	14.07.2022	14.07.2022	195	48.1 | 47.3
		15.07.2022	196	47.5
	16.07.2022		197	48.4
		31.07.2022	212	50.7
	01.08.2022		213	51.8
		03.08.2022	215	51.5
	24.08.2022		236	58.7
		28.08.2022	240	59.4
		04.09.2022	247	62.0
	07.09.2022		250	63.7
		16.09.2022	259	66.4
	25.09.2022		268	70.6
Spatial Resolution	30 m	20 m	500 m	

based on multi-angle observations of 16 days, where the reference date is the 9th day (SCHAAF and WANG 2021). I only downloaded MODIS data of the AOI in Figure 3. This data set came in sinusoidal projection. For the application of the 6S code, I required information about the state of the atmosphere, which I acquired from the Level-1 and Atmosphere Archive & Distribution System Distributed Active Archive Center (LAADS DAAC) website (NASA 2023b). The aerosol optical thickness (AOT)

at 550 nm was available in the MOD04_L2 product MODIS/Terra Aerosol 5-Min L2 Swath 10km (LEVY et al. 2015), ozone concentration and water vapor in the MOD08_D3 product MODIS/Terra Aerosol Cloud Water Vapor Ozone Daily L3 Global 1Deg CMG (PLATNICK et al. 2015).

My workflow (Figure 6) for the satellite imagery followed the methodological principles developed by SHUAI et al. (2011). As preprocessing, I extracted only ”good” pixels of the BRDF parameters. I applied a cloud mask to the L8 and S2 reflectance bands with data supplied in the product file bundles (MODIS: quality file for each band, L8: quality assessment pixels, S2: scene classification). This step increased the data quality but led to some spatial gaps. The L8 and S2 data were clipped to the AOI extent during import to SAGA and later to the land surface with coastline data from DANISH AGENCY FOR DATA SUPPLY AND INFRASTRUCTURE (2023). For the topographic correction of the reflectance data, I used the C-Correction method, which was recommended by TRAVERSA et al. (2021) for L8 albedo validation in Antarctica and Greenland, and a digital surface model (DSM) from the ArcticDEM project with a 2 m resolution (PORTER et al. 2018). The final preprocessing step was projecting the reflectance data to sinusoidal projection to match MODIS data.

The conversion of L8 or S2 reflectance to albedo needed land cover class-specific factors (green in Figure 6). As one main step, I determined the ”pure” class cells, where one MODIS cell was filled predominantly with one land cover class L8 or S2 (yellow in Figure 6). Thus, I conducted an unsupervised cluster analysis (k-means clustering) and created a land cover class grid in MODIS resolution, where data cells were covered with one class for at least 60 %. This resulted in further data gaps. For the computation of the albedo to nadir ratios (blue in Figure 3), a series of calculations were necessary, as follows.

According to SHUAI et al. (2011), I calculated the MODIS nadir reflectance in L8 or S2 sun view geometry based on the BRDF model in Equation 1, as

$$R_{\lambda,m}(\Omega_{lan/sen}) = R_{\lambda}(\Theta_s = \Theta_{s,lan/sen}, \Theta_v = 0, \phi = 0) \tag{4}$$

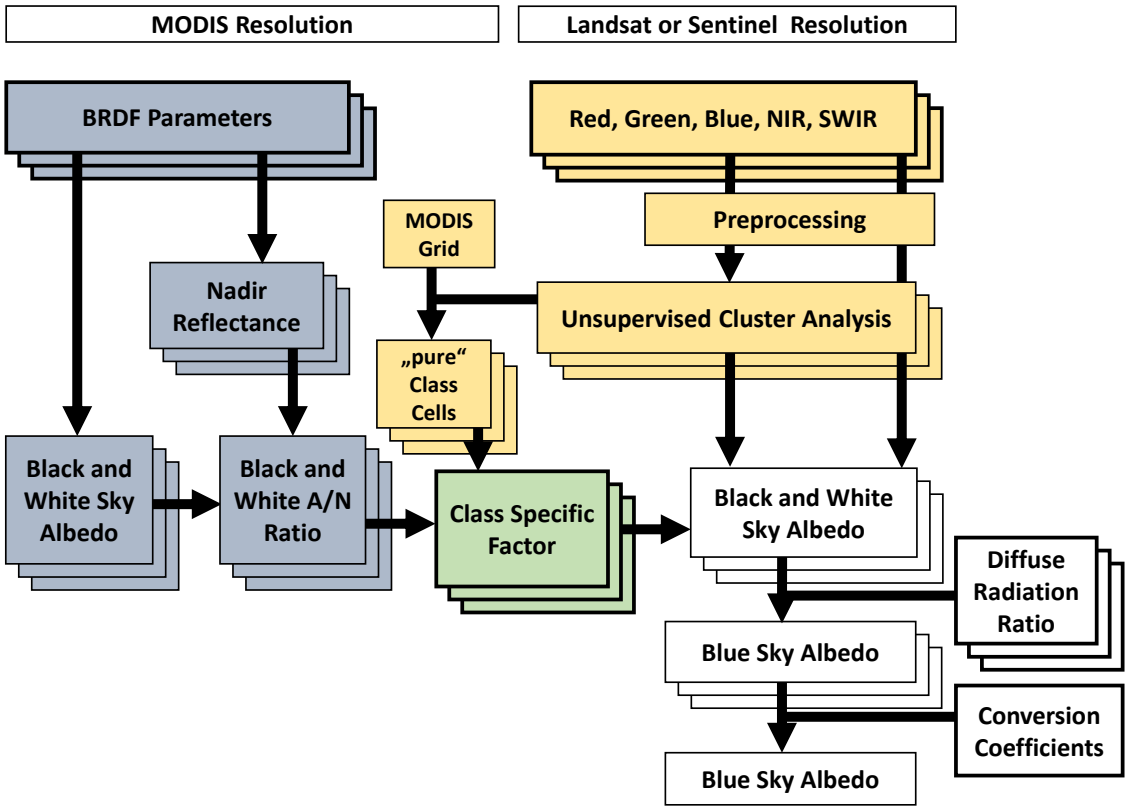

Figure 6: Workflow for the satellite-based albedo with MODIS BRDF and L8 or S2. Bold frames indicate relevant input data and the main interim results. Stacked boxes refer to band specific steps and data. The background colour clusters the main analysing steps. The calculation of the black and white sky albedo to nadir reflectance ratio (blue) and the determination of the ”pure” class cells (yellow) was performed independently. Based on these, I computed a class specific factor (green) that was necessary to convert the L8 and S2 reflectance into albedo (white).

with the RossThick kernel K_{vol}, the volumetric scattering from canopy as

$$K_{vol} = \frac{(\pi/2 - \xi)\cos\xi + \sin\xi}{\cos\Theta_s + \cos\Theta_v} - \frac{\pi}{4} \tag{5}$$

with the scattering angle (ξ) and

$$\cos\xi = \cos\Theta_s \cdot \cos\Theta_v + \sin\Theta_s \cdot \sin\Theta_v \cdot \cos\phi \tag{6}$$

according to ROUJEAN et al. (1992). Because the crown vertical to horizontal radius ratio was set to 1 as suggested by STRAHLER et al. (1999), I calculated the LiSparse

kernel K_{geo}, the geometric-optical surface scattering from shadow casting objects as

$$\begin{aligned} K_{geo} = O(\Theta_s, \Theta_v, \phi) - \sec\Theta_s - \sec\Theta_v \\ + \frac{1}{2} \cdot (1 + \cos\xi) \cdot \sec\Theta_s \cdot \sec\Theta_v \end{aligned} \tag{7}$$

with

$$O = \frac{1}{\pi} \cdot (t - \sin t \cdot \cos t) \cdot (\sec\Theta_s + \sec\Theta_v) \tag{8}$$

$$\cos t = \frac{h}{b} \cdot \frac{\sqrt{D^2 + (\tan\Theta_s \cdot \tan\Theta_v \cdot \sin\phi)^2}}{\sec\Theta_s + \sec\Theta_v} \tag{9}$$

$$D = \sqrt{\tan^2\Theta_s + \tan^2\Theta_v - 2 \cdot \tan\Theta_s \cdot \tan\Theta_v \cdot \cos\phi} \tag{10}$$

as derived by WANNER et al. (1995). I had to adapt the ratio of the center crown height to the crown vertical radius h/b to yield a mathematically solvable calculation. Divergent from the suggestion from STRAHLER et al. (1999) of $h/b = 2$, I reduced the relative height to 1.41, which is justifiable content-wise because the vegetation is rather low in the tundra WANNER et al. (1995).

I calculated the black (Equation 11) and white sky albedo (Equation 12) with the formulae, constants and estimates of white sky kernel (Table 3) supplied in the user guide of the current product version. The formulae are suitable to estimate these albedo types for any SZA with good accuracy (PROFESSOR CRYSTAL SCHAAF'S LAB 2023). The SZA was supplied in the L8 and S2 metadata.

$$\begin{aligned} \alpha_{bs,m,\lambda}(\Theta_{s,lan/sen}) = f_{iso,\lambda} \cdot (g_{0iso} + g_{1iso} \cdot \Theta^2_{s,lan/sen} + g_{2iso} \cdot \Theta^3_{s,lan/sen}) + \\ f_{vol,\lambda} \cdot (g_{0vol} + g_{1vol} \cdot \Theta^2_{s,lan/sen} + g_{2vol} \cdot \Theta^3_{s,lan/sen}) + \\ f_{geo,\lambda} \cdot (g_{0geo} + g_{1geo} \cdot \Theta^2_{s,lan/sen} + g_{2geo} \cdot \Theta^3_{s,lan/sen}) \end{aligned} \tag{11}$$

$$\alpha_{ws,m,\lambda} = f_{iso,\lambda} \cdot g_{iso} + f_{vol,\lambda} \cdot g_{vol} + f_{geo,\lambda} \cdot g_{geo} \tag{12}$$

Then, I calculated the black and white sky albedo to nadir rations with the results from Equations 4, 11 and 12 as in Equation 13 and 14.

$$\bar{\alpha}_{bs,m,\lambda}(\Omega_{lan/sen}) = \frac{\alpha_{bs,m,\lambda}(\Theta_{s,lan/sen})}{R_{m,\lambda}(\Omega_{lan/sen})} \tag{13}$$

Table 3: Constants for black sky and estimates of white sky kernel for albedo calculation (PROFESSOR CRYSTAL SCHAAF'S LAB 2023).

Albedo	Term	Isotropic (iso)	RossThick (vol)	LiSparseR (geo)
black sky	g_0	1.0	-0.007574	-1.284909
	g_1	0.0	-0.070987	-0.166314
	g_2	0.0	0.307588	0.041840
white sky	g	1.0	0.189184	-1.377622

$$\bar{\alpha}_{ws,m,\lambda}(\Omega_{lan/sen}) = \frac{\alpha_{ws,m,\lambda}}{R_{m,\lambda}(\Omega_{lan/sen})} \tag{14}$$

Based on these ratios and the "pure" class cells, I determined the land cover class-specific factor. For that, I averaged the black and white sky albedo to nadir ratios class-wise using the "pure" class cells only. This allowed the calculation of albedo in Landsat or Sentinel resolution (white boxes in Figure 6) with the assumption in Equation 2. Thus, I calculated the L8 and S2 black and white sky albedo as in Equation 15 and 16 with consideration of the unsupervised cluster analysis.

$$\alpha_{bs,lan/sen,\lambda} = \bar{\alpha}_{bs,m,\lambda}(\Omega_{lan/sen}) \cdot R_{lan/sen,\lambda} \tag{15}$$

$$\alpha_{ws,lan/sen,\lambda} = \bar{\alpha}_{ws,m,\lambda}(\Omega_{lan/sen}) \cdot R_{lan/sen,\lambda} \tag{16}$$

For the narrow blue sky albedo, I applied the Equation 17 as TOMASI et al. (2020). As such, the blue sky albedo is the sum of the weighted black and white sky albedo with the fraction of direct solar radiation (dir_λ) and diffuse solar radiation, calculated as ($1 - dir_\lambda$). The fraction of the direct solar radiation was simulated by the 6S code, which I ran in ALG with input variables concerning the sun view geometry of L8 and S2 acquisition time and the atmospheric state provided by MODIS data. In eleven cases MODIS did not offer good AOT data, which are marked in the Appendix in Table 9. Thus I entered 0.12, which is the global average AOT at 550 nm (KINNE 2019). Table 9 in the Appendix lists all relevant in- and output of these simulations.

$$\alpha_{lan/sen,\lambda} = \alpha_{bs,lan/sen,\lambda} \cdot dir_\lambda + \alpha_{ws,lan/sen,\lambda} \cdot (1 - dir_\lambda) \tag{17}$$

Finally, for the calculation of the broadband blue sky albedo, I conducted a narrow to broadband conversion. I applied existing coefficients for snow-free surfaces from WANG, ERB, et al. (2016) for L8 and from LI et al. (2018) for S2. Thus, I calculated L8 and S2 albedo as in Equations 18 and 19, respectively, where $_{bi}$ refers to the band numbers.

$$\begin{aligned}\alpha_{lan} = \alpha_{lan,b2} \cdot 0.2453 + \alpha_{lan,b3} \cdot 0.0508 + \alpha_{lan,b4} \cdot 0.1804 + \\ \alpha_{lan,b5} \cdot 0.3081 + \alpha_{lan,b6} \cdot 0.1332 + \\ \alpha_{lan,b7} \cdot 0.0521 + 0.0011\end{aligned} \tag{18}$$

$$\begin{aligned}\alpha_{sen} = \alpha_{sen,b2} \cdot 0.2688 + \alpha_{sen,b3} \cdot 0.0362 + \alpha_{sen,b4} \cdot 0.1501 + \\ \alpha_{sen,b8A} \cdot 0.3045 + \alpha_{sen,b11} \cdot 0.1644 + \\ \alpha_{sen,b12} \cdot 0.0356 - 0.0049\end{aligned} \tag{19}$$

For the analysis of the BRDF corrected albedo, I additionally calculated the albedo with the Lambertian assumption and several indices. Assuming a Lambertian surface, the albedo equals the nadir-viewing surface reflectance integrated over the spectrum. In the following, the term nadir reflectance refers to that albedo, whereas the BRDF corrected albedo is just called albedo. For the calculation of the nadir reflectance ($R(\Theta_v = 0)$), I applied existing narrow to broadband coefficients that assumed a Lambertian surface and combined them with the preprocessed surface reflectance bands (SR_{bi}) as in Equations 20 and 21. The coefficients for L8 came from LIANG (2001) and were developed for Landsat Thematic Mapper (TM) and ETM+ but have been tested for L8 (NAEGELI et al. 2017). The coefficients for S2 were developed by BONAFONI and SEKERTEKIN (2020).

$$\begin{aligned}R_{lan}(\Theta_v = 0) = SR_{lan,b2} \cdot 0.356 + SR_{lan,b4} \cdot 0.130 + SR_{lan,b5} \cdot 0.373 + \\ SR_{lan,b6} \cdot 0.085 + SR_{lan,b7} \cdot 0.072 - 0.0018\end{aligned} \tag{20}$$

$$\begin{aligned}R_{sen}(\Theta_v = 0) = SR_{sen,b2} \cdot 0.2266 + SR_{sen,b3} \cdot 0.1236 + SR_{sen,b4} \cdot 0.1573 + \\ SR_{sen,b8A} \cdot 0.3417 + SR_{sen,b11} \cdot 0.1170 + SR_{sen,b12} \cdot 0.0338\end{aligned} \tag{21}$$

The normalised difference moisture index (NDMI), NDVI and normalised difference water index (NDWI) were calculated as in Equations 22, 23 and 24. The indices were

designed to detect vegetation moisture, vegetation greenness and water surfaces, respectively (KARAMI et al. 2018; NITZE and GROSSE 2016). Though my research question focused on vegetation, I chose to use the NDWI because the study area included wetlands with both surface water and vegetation. The NDMI can assess moisture with the SWIR band and differentiate vegetation from water with the NIR band, where vegetation has a high and water a low reflectance. In the end, I projected all broadband albedo results and indices to World Geodetic System 1984 (WGS84) UTM 22N.

$$NDMI = \frac{NIR - SWIR1}{NIR + SWIR1} \tag{22}$$

$$NDVI = \frac{NIR - Red}{NIR + Red} \tag{23}$$

$$NDWI = \frac{Green - NIR}{Green + NIR} \tag{24}$$

3.4 Statistical Analysis

Analysis of AWS2 Data

Before the analysis, I excluded measurements with an incoming SWR of below 10 W/m² or below the outgoing SWR to reduce the risk of incorrect measurements. For the calculation of the daily mean albedo, I summed up the incoming and outgoing SWR per day and divided the outgoing sum by the incoming sum. With these daily mean values, I calculated the monthly mean. The daily albedo was above 0.4 at 10 days in the beginning of June or the end of September, which indicated the presence of some snow. Thus, I excluded outliers outside the range of the first quartile minus 1.5 * interquartile range (IQR) and the third quartile plus 1.5 * IQR. With that data, I approximated the seasonal trend with a smoothing function. To assess the effect of clouds, I estimated seasonal trends for all cloud conditions, for days with < 30 % cloud cover and for days with > 70 % cloud cover using the cloud cover at 12 pm local time.

Land Cover Classification Data

RUDD et al. (2021) created a land cover classification based on S2 imagery, a digital elevation model and ground reference data, which was kindly provided to me by them for this thesis. It came in WGS84 UTM 22N projection with a spatial resolution of 10 m, which I resampled with the majority method to the L8 and S2 resolution. During the

analysis, I calculated the descriptive statistics of the Albedometer and satellite albedo and the correlation with the indices per land cover class. The land cover classes dominated by vegetation in the study area were defined by KARAMI et al. (2018) as follows: fen (water logged, grasses and mosses), dry heath & grassland (mostly *Betula* and *Vaccinum*, rather low moisture in growing season), wet heath (*Betula*, *Vaccinum*, *Salix*, *Empetrum*, vegetation < 40 cm, wetter in the growing season compared to dry heath & grassland), copse & tall shrub (*Salix* and *Betula* > 40 cm, wet in growing season). To avoid bias from the town area, which was in various classes originally, I manually assigned pixels with visible buildings and road structure in Google Satellite to a new class ”town”.

Statistical Tests

To assess whether there were significant differences between dates, land cover classes or correlations to indices, I applied statistical tests to the Albedometer and satellite data. For latter, I excluded outliers as for the AWS2 data and land cover classes with < 1000 pixels in a scene to increase data representativity. As the applied narrow to broadband coefficients were designed for snow-free surfaces and the reflectance in shadows is not representative for that surface, I excluded the snow and shadow class from further analysis. At first, I tested whether the data followed a normal distribution with the Kolmogorov-Smirnov-Test. Because statistical tests can be sensitive to large sample sizes (LANTZ 2013), I additionally assessed this visually with Q-Q plots and histograms. As a normal distribution is a requirement for some statistical analyses, I report the result but do not discuss this further.

For the examination of relationships between albedo and indices, I calculated the Pearson correlation coefficient for normally distributed variables and Spearman’s rank correlation coefficient otherwise. Additionally, I executed Pearson correlation to the albedo and nadir reflectance and compared them to assess the effect of the BRDF correction. I tested for homogeneity of variances between dates with Bartlett’s Test if the albedo followed a normal distribution in that class. Otherwise, and to test for homogeneity of variances between classes, I applied Fligner-Killeen’s Test. To test for central tendencies, I used the Kruskal-Wallis Test and the Mann-Whitney-Wilcoxon-Test as a post-hoc analysis as the requierements of the Analysis of Variance were not fulfilled.

Assessment of non-changing Surfaces

During the observation period, the satellite-based albedo of vegetated areas could have varied due to actual surface changes or due to other influences such as viewing geometry and atmospheric effects. To assess how large the atmospheric effect was, I created polygons of selected areas, where the occurrence of surface changes was less likely based on the visual analysis of SAGA's Google Satellite base map. These surface areas needed to be larger than a L8 pixel and included the soccer field with artificial lawn, gravel areas near the Heliport, a large roof in town and rock dominated spots with little vegetation. For each scene, I calculated descriptive statistics per polygon and evaluated the variability.

Comparison of Sensors

I compared the albedo of all sensors as it was possible with the available data. For the satellite pixels at AWS2, I determined the root-mean-square error (RMSE) of the satellite-based albedo in comparison to the AWS2 daily mean as in Equation 25. In *Kuup Ilua* North, where I could collect field data during clear sky conditions, I determined the RMSE of the Albedometer data of 30th August and the satellite scenes from 24th August to 4th September.

$$RMSE = \sqrt{\frac{\sum_{i=1}^{n} (\hat{\alpha}_i - \alpha_i)^2}{n}} \tag{25}$$

with α_i being the albedo of AWS2 or the Albedometer at observation i, $\hat{\alpha}_i$ being the predicted albedo of the satellites at observation i and n as the number of suitable observations. To compare the Albedometer with AWS2, I calculated the mean absolute deviation d of the Albedometer measurements $\hat{\alpha}_i$ in the wet heath class to the AWS2 daily mean α_{AWS} of 29th August as in Equation 26.

$$d = \frac{\sum_{i=1}^{n} |\hat{\alpha}_i - \alpha_{AWS}|}{n} \tag{26}$$

I conducted a step-wise multiple regression analysis to examine whether albedo differences of L8 and S2 were be associated with a specific reflectance. For the July and August scenes, I subtracted the L8 scene with the closest acquiring date from a S2 scene. These six difference grids served as the dependent variable. I performed the

step-wise multiple regression analysis for each grid with the preprocessed surface reflectance bands of L8 and S2 as predictors separately. The surface reflectance bands did not contain the BRDF correction. Thus, I examined whether using the band-wise white sky albedo as predictors influenced the model quality to assess the effect of the BRDF correction on the L8 and S2 differences. As there were up to four days between the L8 and S2 scenes, the atmosphere changed and influenced the albedo. With this limitations the analysis cannot offer a robust explanation but might point towards circumstances that could be considered in future research.

4 Results

4.1 Temporal Variability of AWS Albedo

The monthly and daily mean albedo at AWS2 followed a seasonal pattern. The monthly descriptive statistics over all years are listed in Table 4. Averaged, November was the month with the highest mean albedo. No data were available for December and January. From February to April the albedo decreased slightly and then notably from April to June. The monthly albedo stayed at a similar level from June to September and increased in October. In Figure 7, the monthly mean albedo with the smoothed linear regression demonstrate that the interannual variability is more pronounced in the months October to May, which usually have snow. Over the study period, the monthly average of albedo and snow depth had a significant, strong correlation (Spearman's rho 0.85,

Table 4: Monthly descriptive statistics of albedo at AWS2 over the period from 2013 to 2022. No data were available for December and January. Data: GEM (2023c).

	Feb	**Mar**	**Apr**	**May**	**Jun**	**Jul**	**Aug**	**Sep**	**Oct**	**Nov**
Minimum	0.60	0.46	0.40	0.16	0.16	0.17	0.17	0.15	0.28	0.41
Median	0.81	0.80	0.69	0.29	0.16	0.18	0.18	0.19	0.47	0.86
Mean	0.79	0.76	0.64	0.35	0.16	0.18	0.18	0.19	0.50	0.81
Standard deviation	0.08	0.12	0.16	0.18	0.01	0.00	0.01	0.03	0.18	0.15
Maximum	0.88	0.85	0.84	0.63	0.19	0.19	0.20	0.25	0.80	0.95

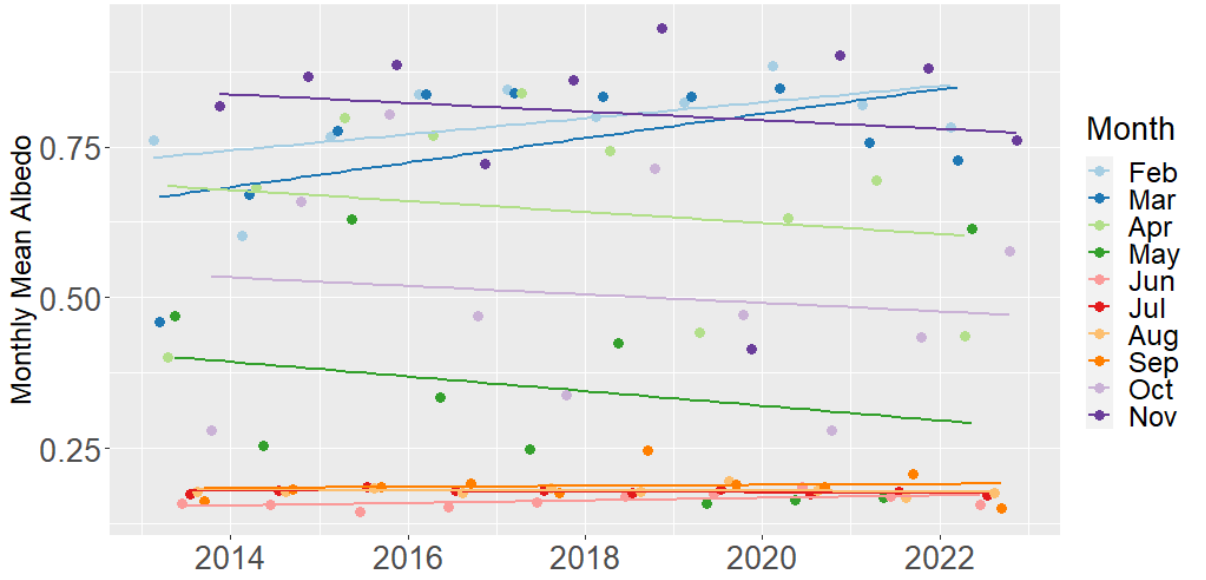

Figure 7: Monthly mean albedo at AWS2 from February 2013 to November 2022 including outliers. The lines represent the linear regression trends. No data were available for January and December. Data: GEM (2023c).

p-value < 2.2e-16). While the months June to September showed no trend, February and March displayed a slight positive trend and April, May, October and November a negative one. However, due to limited data availability, these were not significant ($p > 0.05$).

Though this was not visible in the monthly data, the daily mean albedo varied from June to September, when the study area was mostly snow-free. Before outlier removal, the albedo lay between 0.11 (21st June 2022) and 0.85 (26th September 2018) in these months, and the maximum albedo of July and August, when no snow was detected at AWS2 in the last decade, was 0.26 (12th July 2018). In Figure 8, the daily albedo without outliers is approximated by a quadratic function. Most years display an increase of albedo from June to the beginning of August and then a decrease. This is less evident in the years from 2018 to 2021. The deviation from the daily mean to the quadratic function as well as the differences between neighbouring days tend to increase over time within the vegetation period.

The seasonal progress of albedo changed with cloudiness. The Figure 19 in the Appendix displays the corresponding content of Figure 8 for days with a cloud cover < 30 % and > 70 %. The albedo increase in June and July could be observed in both the high and low cloud plots. However, for the days with a cloud cover < 30 %, the maximum of

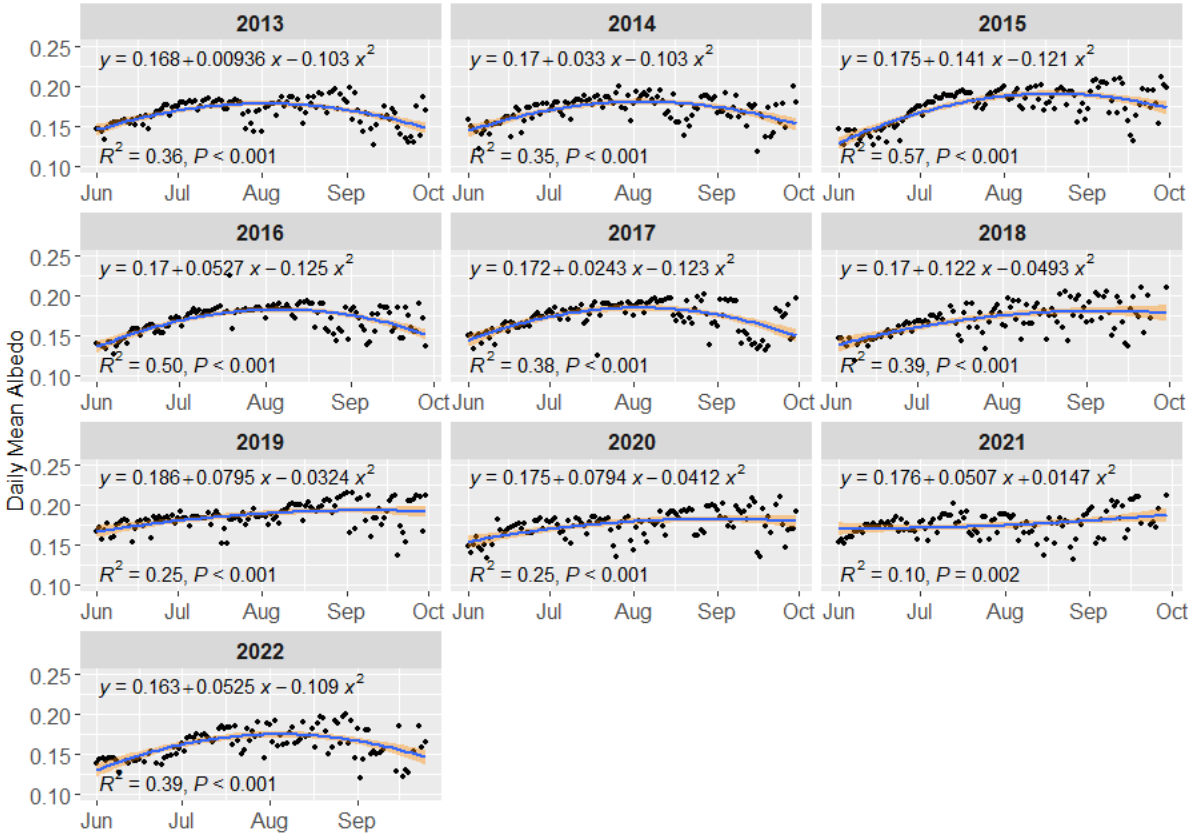

Figure 8: Daily mean albedo at AWS2 (black points) in the snow-free period. The equation, R^2 and P describe the smoothing (blue line) and its quality. The 95 % confidence interval is displayed in orange. Data: GEM (2023c).

the approximated quadratic function is postponed towards the end of August for 2013 to 2017 followed by a slight albedo decrease only. In 2019, the albedo increased roughly linear under low cloud conditions.

4.2 Spatial Variability of Albedometer Measurements

The measured data of the Albedometer differed between dates, study sites and surface characteristics. The descriptive statistics for albedo per study site are listed in Table 5. According to Kolmogorov-Smirnov-Test, the albedo per day was not normally distributed (p = 1.6e-06 for 29th August, p < 2.2e-16 for 30th August and 8th September), which was supported by the Q-Q plots and histograms. Overall, points dominated by lichen, *Salix glauca* or field horsetail (*Equisetum arvense*, hereafter *Equisetum*) measured on 30th August demonstrated the highest albedo (> 0.23) while the lowest values (< 0.10) were found at points with predominantly black soil or water surfaces in the footprint of the Albedometer.

Table 5: Descriptive statistics of the Albedometer measurements on Disko Island, Greenland in 2022.

Date	Site Name	Min	Median	Mean	Max	Standard deviation
29. Aug	Arctic Station	0.05	0.15	0.13	0.19	0.05
30. Aug	*Kuup Ilua* North	0.08	0.18	0.18	0.28	0.05
8. Sep	*Kuup Ilua* South	0.10	0.13	0.14	0.17	0.02

Generally, measurements close to each other or with similar surface characteristics were more alike than more distant ones with deviating surface characteristics. Figure 9 shows the Albedometer measurements in *Kuup Ilua*. In a day-wise comparison, the lowest albedo values in *Kuup Ilua* North were located above a creek, near the river on a flood plain with mostly bare soil and a small grass and *Salix glauca* cover and in a partly wet lateral branch of the river dominated by stones. The highest albedo in that area was above a white lichen patch with a decreasing trend with increasing *Betula nana*, *Salix glauca* and *Vaccinium* cover. The albedo of otherwise dominated areas lay in that range, which included the light green moss dominated patch in the west of the transect, a hummock dominated area with varying bare soil, grasses and *Salix glauca* cover in the eastern end of the transect and individual measurements above *Equisetum* and *Eriophorum spec.* dominated spots further in the east of the study site.

In *Kuup Ilua* South the lowest albedo was located in the western wetland (Patch 0 in Figure 9) with an increasing trend with increasing vegetation covering open water. The measurements in the northeast (Patch 4) lay in a similar range though the rather dry spot (TDR vwc raw data mean 34 %) with mixed vegetation dominated by *Betula nana*, *Vaccinium* and greyish, dead *Cassiope* was different. The highest albedo of the *Kuup Ilua* South measurements were located in the southwest in the water-saturated, grass dominated Patch 1 with some *Salix glauca* (TDR vwc raw data mean 70 %). There were no distinct differences between Patches 2 and 3, of which Patch 2 was dominated by hummocks and covered by a mix of low *Salix glauca* and other vegetation (TDR vwc raw data mean 50 %). Patch 3 had a dense, and with a height of 25 - 76 cm, a comparably high *Salix glauca* cover (TDR vwc raw data mean 42 %).

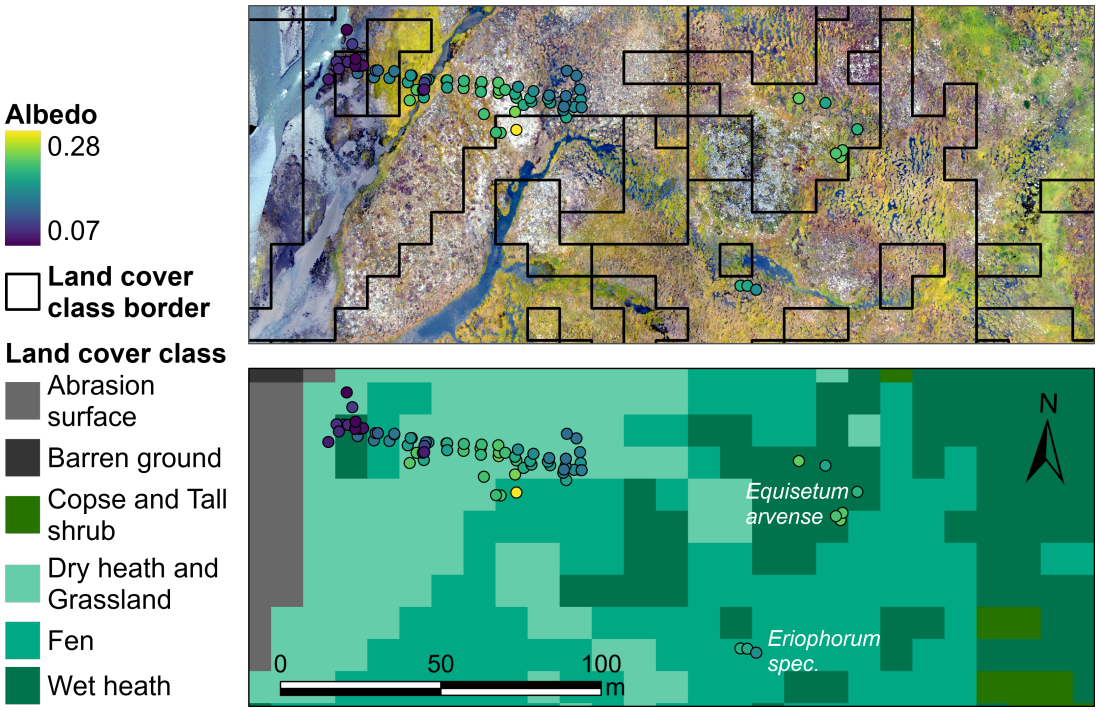

(a) *Kuup Ilua* North, albedo on 30th August 2022, clear-sky.

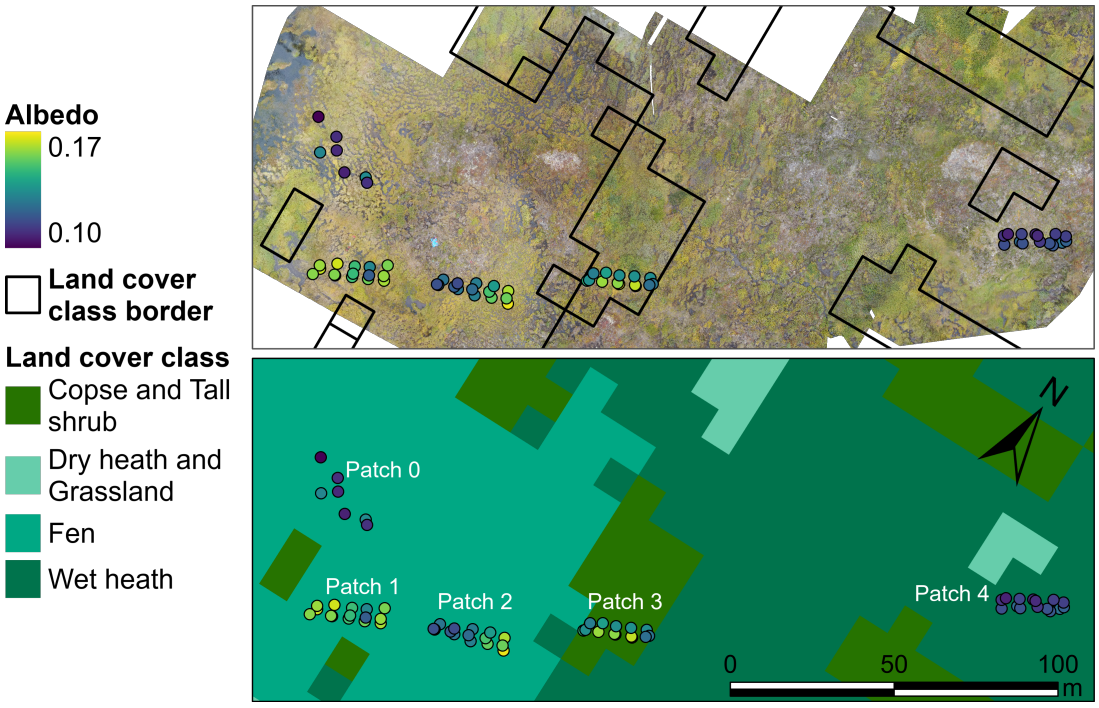

(b) *Kuup Ilua* South, albedo on 8th September 2022, cloudy.

Figure 9: Mean albedo of Albedometer measurements in *Kuup Ilua* and land cover classification. It should be noted that the river in the west of the Transect 2 and creeks are not classified as water but as part of neighbouring land cover classes. The black lines in the drone imagery base maps indicate the borders of the land cover classification from RUDD et al. (2021). The drone imagery base maps were recorded on (a) 7th September 2022 and (b) 8th September 2022 (SIMONE M. STUENZI and JENNIKA HAMMAR, orthoimage created with Pix4D).

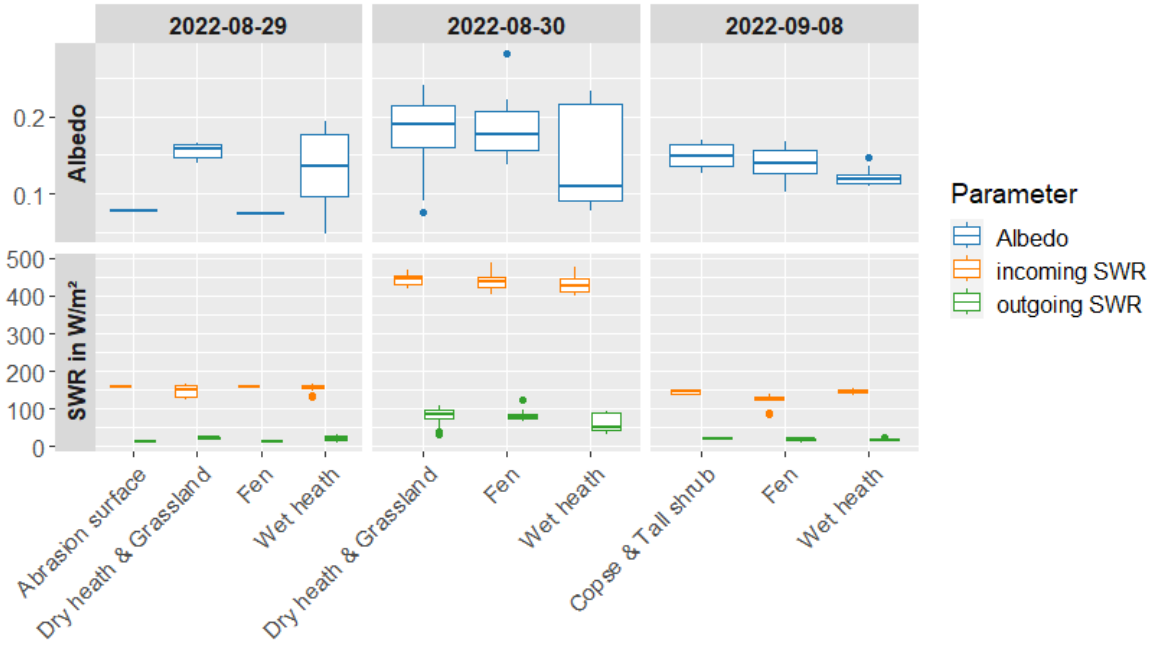

Figure 10: Daily distribution of albedo and SWR per land cover class from Albedometer measurements in the AOI The box represents the first and third quartile with the median as the middle line. The whiskers indicate the minimum and maximum values within the 1.5-times IQR distance to the boxes. The points are outliers beyond that range. The date is given in the format YYYY-MM-DD. Land cover classes based on RUDD et al. (2021).

Figure 10 displays the albedo and the incoming and outgoing SWR per land cover class and date. The incoming SWR of the cloudy days corresponded to approximately a third of the incoming SWR of the clear-sky day, while the proportion of the outgoing SWR of the cloudy days was reduced to roughly a quarter of the outgoing SWR of the clear-sky day. On 30th August, the clear-sky day tended to have a higher albedo with higher variability per land cover class. As albedo is ideally measured during clear-sky days, the focus of the Albedometer results with regard to land cover class are the measurements from *Kuup Ilua* North on 30th August.

Field measurements that were different in surface cover and albedo were combined in one land cover class from RUDD et al. (2021). Thus, the variability of points within a group of comparable surface characteristics as assessed in the field was lower than within a land cover class. The distribution of the albedo per land cover class is displayed in Figure 10, which depicts some differences regarding median albedo, IQR and location of outliers. According to Fligner-Killeen's Test the variances were homogeneous between the land cover classes ($\chi^2(2) = 5.73$, $p = 0.06$) on 30th August. The

Kruskal-Wallis Test and the Mann-Whitney-Wilcoxon-Test indicated that no significant differences of central tendencies of these classes existed ($p > 0.05$). However, in the class-wise descriptive statistics and in the boxplots per class it seems that wet heath differs to the fen and dry heath & grassland classes.

4.3 Variability and Comparison of Satellite-based Albedo

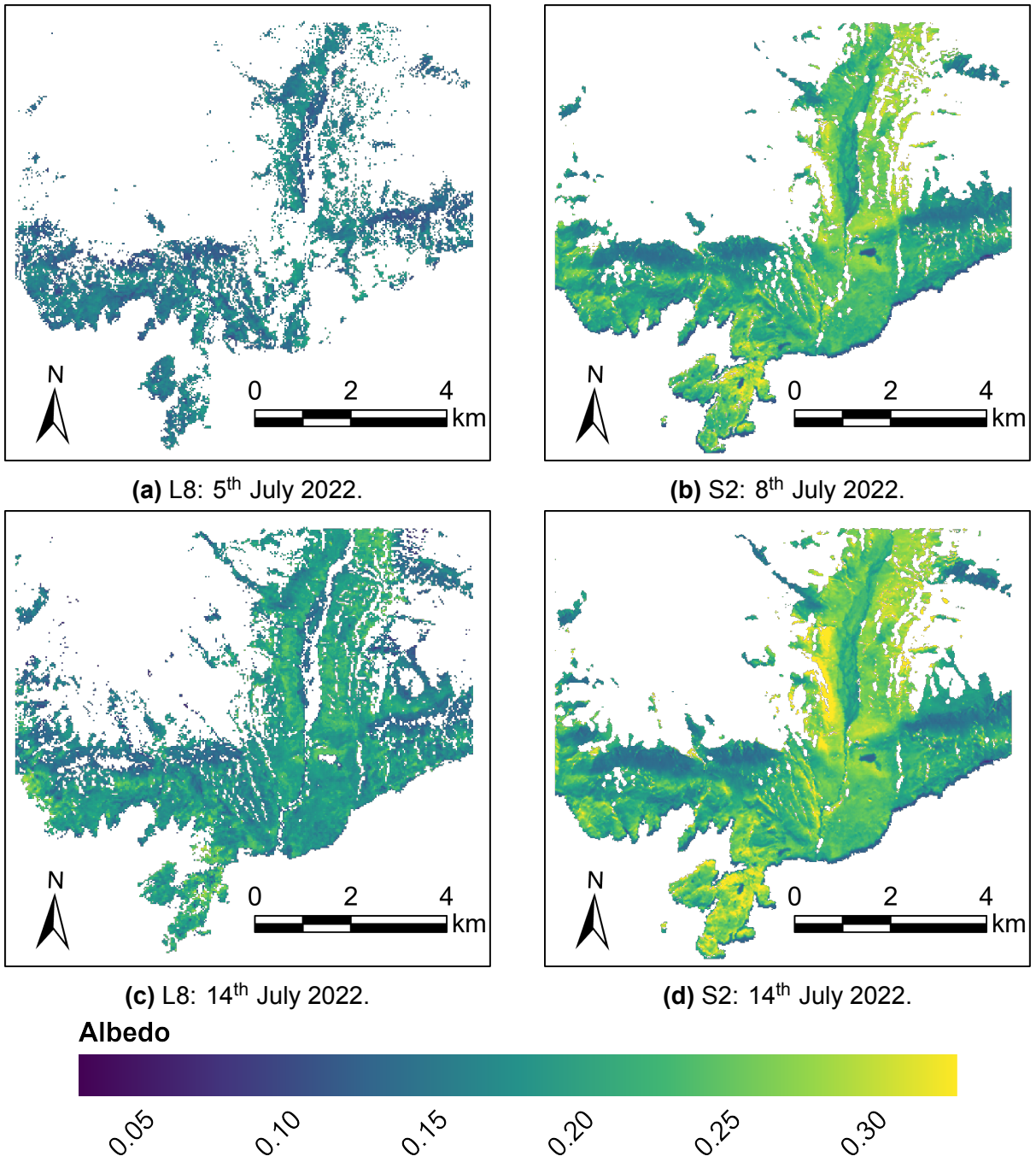

(a) L8: 5th July 2022.

(b) S2: 8th July 2022.

(c) L8: 14th July 2022.

(d) S2: 14th July 2022.

Figure 11: L8 and S2 based albedo on Disko Island, Greenland, of selected dates from the analysed study period in 2022. Albedo calculated with data from ESA, LAADS DAAC, LP DAAC and USGS.

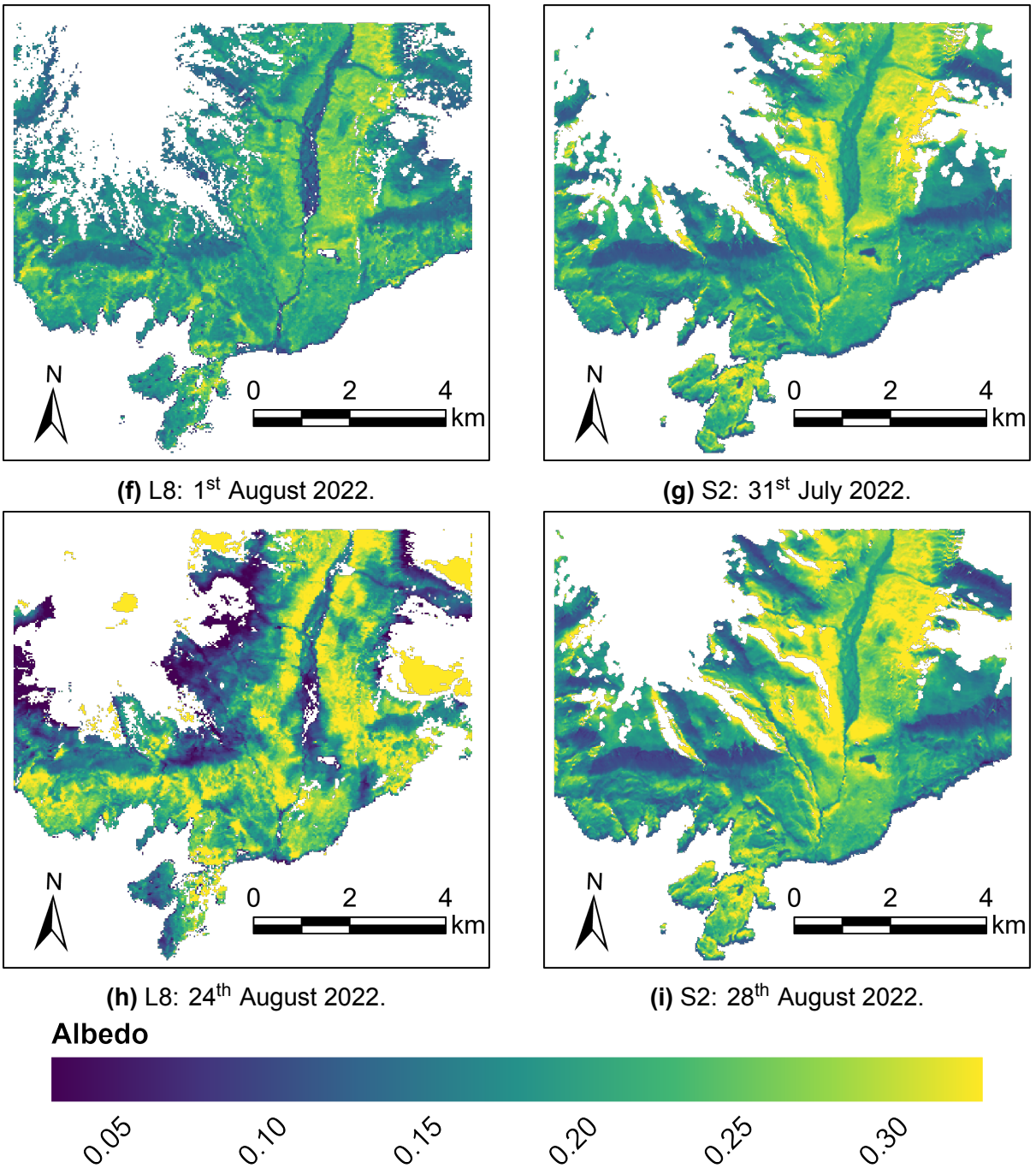

(f) L8: 1st August 2022.

(g) S2: 31st July 2022.

(h) L8: 24th August 2022.

(i) S2: 28th August 2022.

Figure 11: L8 and S2 based albedo on Disko Island, Greenland, of selected dates from the analysed study period in 2022 (continued). Albedo calculated with data from ESA, LAADS DAAC, LP DAAC and USGS.

The satellite-derived albedo varied over space and time. Figure 11 gives an impression of the satellite-based albedo for selected dates. This chapter describes the results from the analysis from the L8 and S2 albedo from 5th July to 4th September 2022. I excluded the other dates in June and September from further analysis, because they had either empty result grids or less than 2500 pixel in the whole scene. I discuss possible causes for this data loss in Chapter 5.4.

According to the Kolmogorov-Smirnov-Test, the scene-wide data did not follow a normal distribution ($p < 0.05$). This included the albedo, the nadir reflectance, NDMI, NDVI and NDWI. The Q-Q plots and histograms revealed that the albedo, the nadir reflectance and the NDMI followed approximately a normal distribution. The NDVI and NDWI either had a bimodal, left or right skewed distribution. Similarly, the class- and day-wise albedo was not normally distributed according to the Kolmogorov-Smirnov-Test($p < 0.05$). However, the histograms indicated that all L8 classes > 1000 pixels (abrasion surface, barren ground, dry heath & grassland and wet heath) tended to follow a normal distribution. In the S2 albedo, the classes abrasion surface, copse & tall shrub, dry heath & grassland, town and wet heath were approximately normally distributed. The class barren ground tended to follow a bimodal distribution, whereas fen was left skewed and water right skewed.

Correlation with Indices

The indices had significant correlations to each other and to albedo but with varying effect size. Table 6 lists the sensor-wide correlation coefficients. The NDVI and NDWI

Table 6: Sensor-wide correlations of L8 and S2 derived albedo and remote sensing indices in the AOI for the analysed study period. A p-value < 0.05 indicates that the correlation is statistically significant. Albedo calculated with data from ESA, LAADS DAAC, LP DAAC and USGS.

Sensor	Variables	Method	Coefficient	p-value
Landsat	Albedo ~ NDMI	Pearson	0.50	< 2.2e-16
Sentinel	Albedo ~ NDMI	Pearson	0.15	< 2.2e-16
Landsat	Albedo ~ NDVI	Spearman	0.67	< 2.2e-16
Sentinel	Albedo ~ NDVI	Spearman	0.45	< 2.2e-16
Landsat	Albedo ~ NDWI	Spearman	-0.67	< 2.2e-16
Sentinel	Albedo ~ NDWI	Spearman	-0.44	< 2.2e-16
Landsat	NDVI ~ NDWI	Spearman	-0.97	< 2.2e-16
Sentinel	NDVI ~ NDWI	Spearman	-0.99	< 2.2e-16
Landsat	NDVI ~ NDMI	Spearman	0.53	< 2.2e-16
Sentinel	NDVI ~ NDMI	Spearman	0.36	< 2.2e-16

were highly correlated with each other. Their correlation with albedo was very similar but with the opposite algebraic sign. The correlation between NDVI and NDMI was lower. Thus, I only present results from the class- and day-wise correlation of NDVI and NDMI to albedo.

The albedo was significantly correlated to NDVI and NDMI in most classes per day. The analysis resulted in five days with 20 observation classes for L8 and in seven days with 51 observation classes for S2. In this counting, I only considered land cover classes with > 1000 pixels and counted one of the eight classes multiple times if it occurred on several days. Among these, four classes were not significantly correlated with NDVI and two classes not with NDMI ($p > 0.05$). That were only the non-vegetated classes abrasion surface, barren ground and water.

The significant correlations over time are displayed in Figure 12. The classes abrasion surface, barren ground, town and water indicated mostly weak to medium correlations

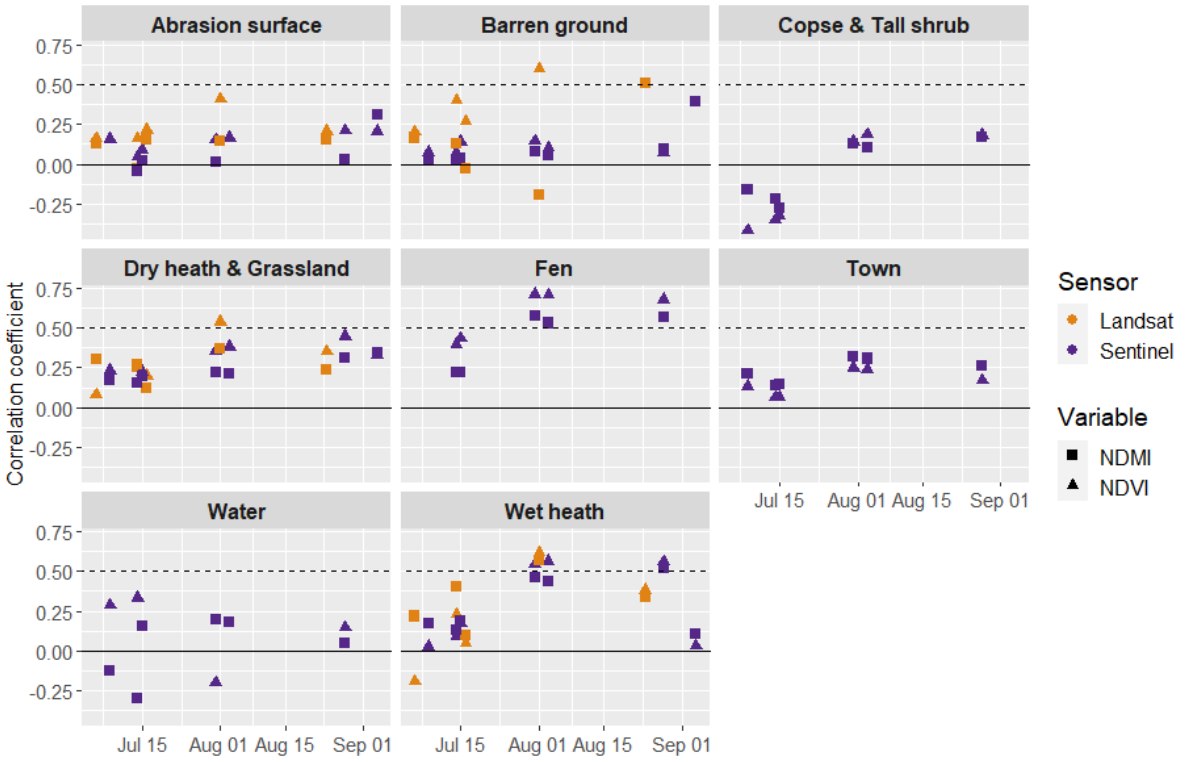

Figure 12: Correlation coefficients of albedo to NDVI and NDMI of significantly correlated classes in the AOI in 2022. The circles indicate the correlation of albedo and NDMI according to Pearson, the triangles the correlation of albedo and NDVI according to Spearman. For orientation of a change of sign and a strong correlation, the solid and dashed line display the zero and the 0.5 line respectively. Albedo calculated with data from ESA, LAADS DAAC, LP DAAC and USGS.

without a trend. The correlations in the vegetation classes tended to increase over time and then partly decreased again. This effect was very small in the dry heath & grassland class with mostly weak to medium correlations. When the correlations in the copse & tall shrub class changed algebraic sign from mid July to August, those of fen increased from a weak to a strong correlation. The correlation coefficients of wet heath could be approximated with a quadratic function, especially for S2. With my research interest in vegetation, I emphasise the vegetation classes when presenting the results of temporal and spatial variability.

Temporal Variability

The scene-wide mean albedo of L8 increased from 0.16 ± 0.02 on 5th July to 0.20 ± 0.08 on 24th August. With exception from 1st August whose standard deviation was smaller than on 16th July, the standard deviation increased over time. The scene-wide mean albedo of S2 was 0.21 ± 0.04 at the beginning of the observation period, on 8th July. It increased to 0.22 ± 0.05 on 15th July and then decreased to its minimum of 0.16 ± 0.05 on 4th September. Similar to L8, the standard deviation of S2 tended to increase over time, though at a smaller scale, and reached its maximum 0.06 on 28th August.

The vegetation classes followed the described trends of the scene. Their boxplots over time are displayed in Figure 13. The boxplots over time for the other classes are in the Appendix in Figure 20. The albedo tended to increase until the end of August. This was more pronounced in the L8 data (dry heath & grassland median 0.16-0.24, wet heath median 0.17-0.27), which had a lower albedo in the beginning of the observation period. The class-wise median albedo of S2 changed as follows in that time: copse & tall shrub 0.21-0.23, dry heath & grassland 0.21-0.16, fen 0.24-0.26, wet heath 0.22-0.18. The increase of the size of the whiskers and thus the variability was also more evident for L8. Bartlett's Test and Fligner-Killeen's Test showed that the variances of different days within a class were not homogeneous ($p < 0.05$). The Kruskal-Wallis Test and the Mann-Whitney-Wilcoxon-Test for each of the vegetation class pointed out that the central tendencies differed significantly ($p < 0.05$) for all days of L8 and most S2 days. No significant differences ($p > 0.05$) existed between 15 th July and 28th August in the fen and copse & tall shrub classes, between 8th July and 31st July in the wet heath class and between 31st July and 3rd August in the fen, copse & tall shrub and dry heath & grassland classes.

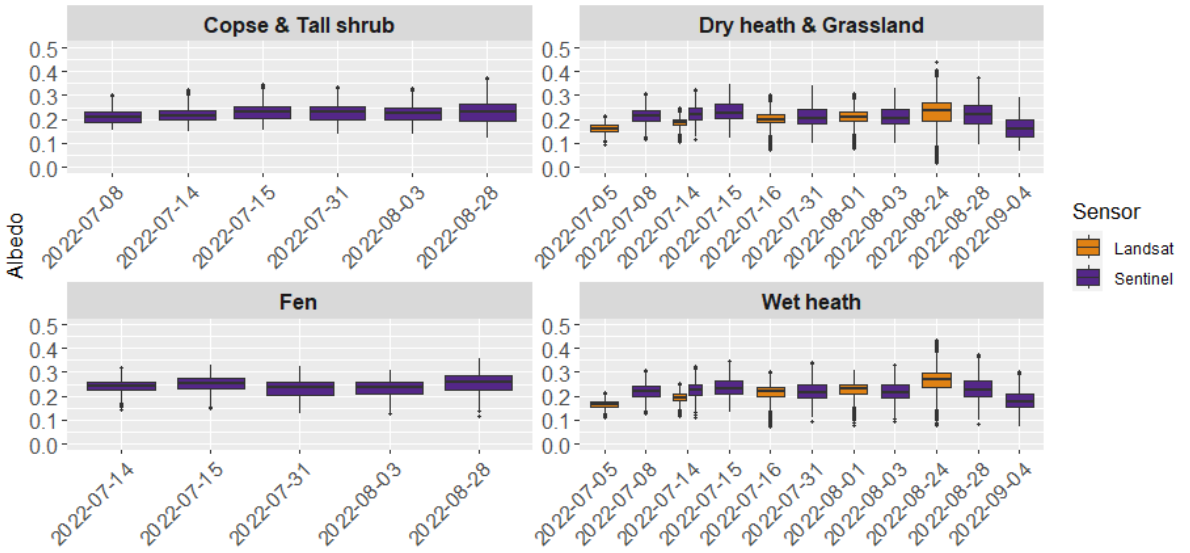

Figure 13: Albedo boxplots for vegetation classes > 1000 pixels after outlier removal in 2022. The box represents the first and third quartile with the median as the middle line. The whiskers indicate the minimum and maximum values within the 1.5-times IQR distance to the boxes. The points are outliers beyond that range. The date is given in the format YYYY-MM-DD. Albedo calculated with data from ESA, LAADS DAAC, LP DAAC and USGS.

Spatial Variability

The class-wise change of L8 and S2 mean albedo over time is shown in Figure 14. These statistics also include classes < 1000 pixels. While differences of the mean albedo between the classes increased over time for L8, the graphs of S2 stayed mainly parallel until the end of August. Similarly, differences of the standard deviation per class increased until the end of August to a greater extent for L8. In comparison of the vegetation classes, the rank of mean and standard deviation differed for L8 and S2. Copse & tall shrub had the highest (mean 0.17-0.28) and dry heath & grassland the lowest albedo (mean 0.16-0.23) in the L8 data. In the S2 data, fen had the highest (mean 0.20-0.25) and dry heath & grassland the lowest albedo (mean 0.16-0.23). While fen was the vegetation class with the mostly highest standard deviation in L8 (0.02-0.08), it had predominantly the lowest standard deviation in S2 (0.03-0.04). The standard deviations of the other classes were very similar to each other (0.02-0.04) in L8 until the beginning of August and in S2 (0.03-0.06).

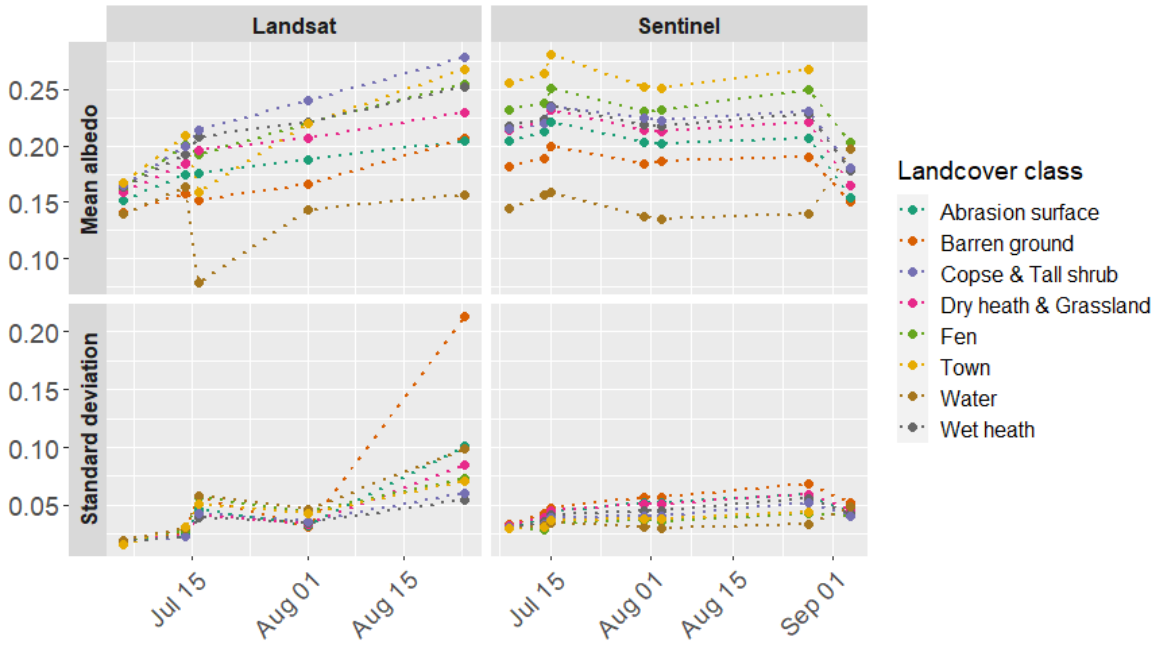

Figure 14: Temporal change of L8 and S2 albedo mean and standard deviation per land cover class in 2022, including classes < 1000 pixels. Albedo calculated with data from ESA, LAADS DAAC, LP DAAC and USGS.

The statistical tests revealed that significant differences existed between the classes within a day. According to Fligner-Killeen's Test, their variances were not homogeneous ($p < 0.05$). The Kruskal-Wallis Test showed that the central tendencies differed significantly ($p < 0.05$) for each day. In the pairwise Mann-Whitney-Wilcoxon-Test only S2's copse & tall shrub and dry heath & grassland classes on 15th July did not differ significantly ($p = 1$) as well as copse & tall shrub and wet heath on 28th August ($p = 1$).

Effect of the BRDF Correction

The albedo and the nadir reflectance coincided with each other to a great extent. The sensor-wise Pearson correlation coefficient was 0.98 ($p < 2.2e\text{-}16$) for L8 as well as S2. In Figure 15, three exemplary scenes per sensor display the relation of albedo and nadir reflectance. The relationship was similar for the other days, which are displayed in Figure 21 in the Appendix. The albedo was mostly above the nadir reflectance. For L8 as well as S2 the difference median, mean and standard deviation was 0.01. This offset increased over time and was more pronounced for higher albedo values. The L8 scenes of 16th July (Figure 21) and 24th August (Figure 15) are the only scene that display several pixels with a large offset.

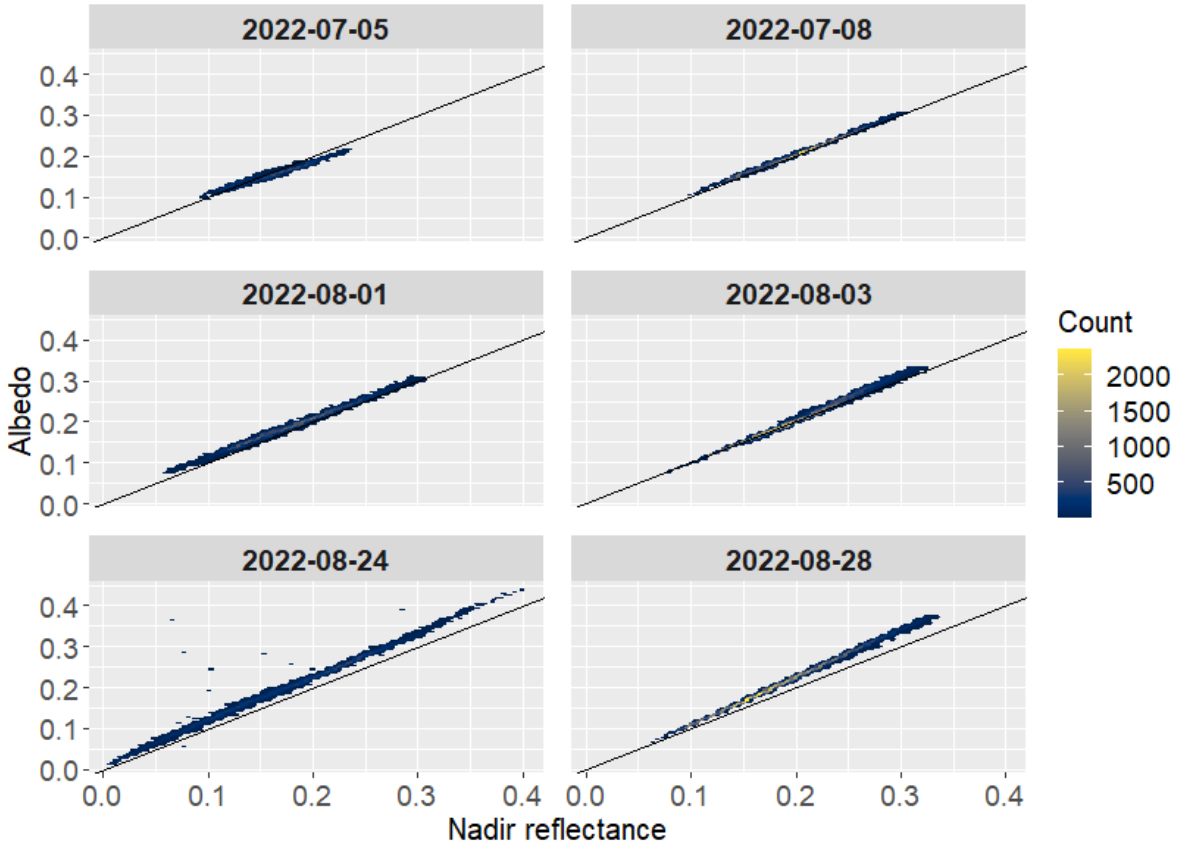

Figure 15: Scatterplots of albedo and nadir reflectance for selected dates of L8 on the left and S2 on the right column. The black line indicates where $\alpha = R(\Theta_v = 0)$. The date is given in the format YYYY-MM-DD. Albedo and nadir reflectance calculated with data from ESA, LAADS DAAC, LP DAAC and USGS.

The statistical tests indicated significant differences between the albedo and the nadir reflectance for almost all days. According to Bartlett's Test, their scene-wide variances were not homogeneous ($p < 0.05$). The Kruskal-Wallis Test revealed that there were significant differences between the central tendencies of albedo and nadir reflectance for most days ($p < 0.05$). Only on 31st July, there was no significant difference in the central tendency in the S2 data ($H(1) = 2.692$, $p = 0.1009$).

Assessment of non-changing Surfaces

The albedo of the assumed non-changing surfaces varied over time in L8 and S2. The mean and standard deviation of the albedo per shape is shown in Figure 16. In all cases, the S2 mean albedo was above that of L8. However, both sensors displayed a similar mean albedo trend in the Heliport and soccer field shapes. On average, the gravel around the Heliport had an albedo of 0.15 ± 0.02 for L8 and 0.21 ± 0.01 for S2, while the soccer field had an albedo of 0.17 ± 0.03 for L8 and 0.21 ± 0.01 for S2. The

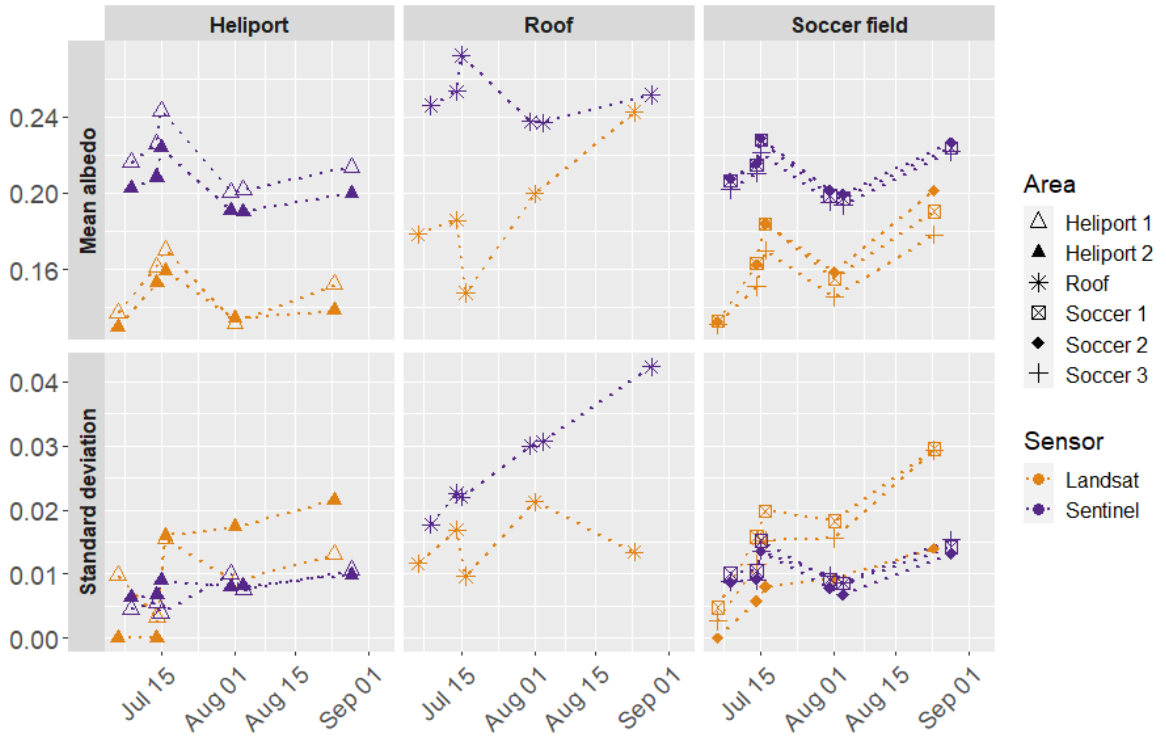

Figure 16: L8 and S2 derived albedo statistics of assumed non-changing surfaces in the AOI in the analysed study period in 2022. The numeration of areas refers to different shapes. Albedo calculated with data from ESA, LAADS DAAC, LP DAAC and USGS.

roof (L8: 0.19 ± 0.03, S2: 0.24 ± 0.03) displayed a diverging albedo trend. The five shapes above stones showed a larger variability and diverging trends in the sensor comparison, so they are excluded in Figure 16.

Comparison of Sensors

The albedo from the different sensors deviated from each other. Table 7 lists the mean albedo of the sensors and the assessment parameters as described in Chapter 3.4. These parameters are partly above the desired accuracy of 0.05 for surface albedo in climate modelling (HENDERSON-SELLERS and WILSON 1983). At AWS2, the albedo values of the satellite pixels were continuously larger (difference 0.03-0.07) than the AWS2 daily mean on the respective days. There, the RMSE of L8 was slightly above that of S2. In *Kuup Ilua* North, the L8 albedo from 24th August was mostly below the Albedometer measurements from 30th August (difference: min -0.13, max 0.04, median -0.05). The S2 albedo was mostly above the Albedometer, while values from the 4th September (difference: min -0.06, max 0.14, median 0.05) were closer to the Albedometer measurements than from 28th August (difference: min -0.03, max 0.20,

Table 7: Comparison metrics of sensor albedo in 2022. In the comparison of the local to the satellite sensors, I contrasted the value of the AWS2 or Albedometer footprint to the value of the satellite pixel of the AWS2 or Albedometer location. In the comparison of the Albedometer to the AWS2, I contrasted the Albedometer measurements in the wet heath class around AWS2 to the measurements from AWS2, which was located in the wet heath class. AWS2 data from GEM (2023c). Satellite albedo calculated with data from ESA, LAADS DAAC, LP DAAC and USGS.

Location	Dates	Sensor 1	Mean albedo 1	Sensor 2	Mean albedo 2	Parameter	
AWS2	all	L8 S2	0.24 0.23	AWS2	0.19	RMSE	0.06 0.04
Kuup Ilua North	24. Aug	L8	0.14	Albedo-meter	0.18	RMSE	0.06
	28. Aug	S2	0.26				0.10
	04. Sep	S2	0.22				0.06
AWS2	29. Aug	AWS2	0.16	Albedo-meter	0.13	d	0.05
AOI	05./08. Jul	L8	0.16	S2	0.20	RMSE	0.06
	14. Jul	L8	0.18	S2	0.21		0.05
	15./16. Jul	L8	0.19	S2	0.22		0.06
	31. Jul/01. Aug	L8	0.19	S2	0.20		0.05
	01./03. Aug	L8	0.19	S2	0.20		0.05
	24./28. Aug	L8	0.20	S2	0.21		0.14

median 0.08), whose RMSE was higher than that of the other compared dates. The Albedometer measurements in the wet heath class near AWS2 varied below and above the AWS2 data but were below it in average (difference: min -0.12, max 0.03, median -0.03). The mean deviation of those Albedometer measurements to the AWS2 daily mean was similar to the RMSE calculations of the satellite-based albedo at AWS2.

The differences of L8 and S2 albedo of nearby days varied over space and time, which is visible in Figure 17 for selected dates. The median difference ranged from 0.001 for the end of August to 0.05 for the beginning of July and was 0.02 for all comparisons, where positive values indicated that S2 was above L8. Figure 18 displays the coefficient of determination per model of the step-wise multiple regression analysis. For most pairs

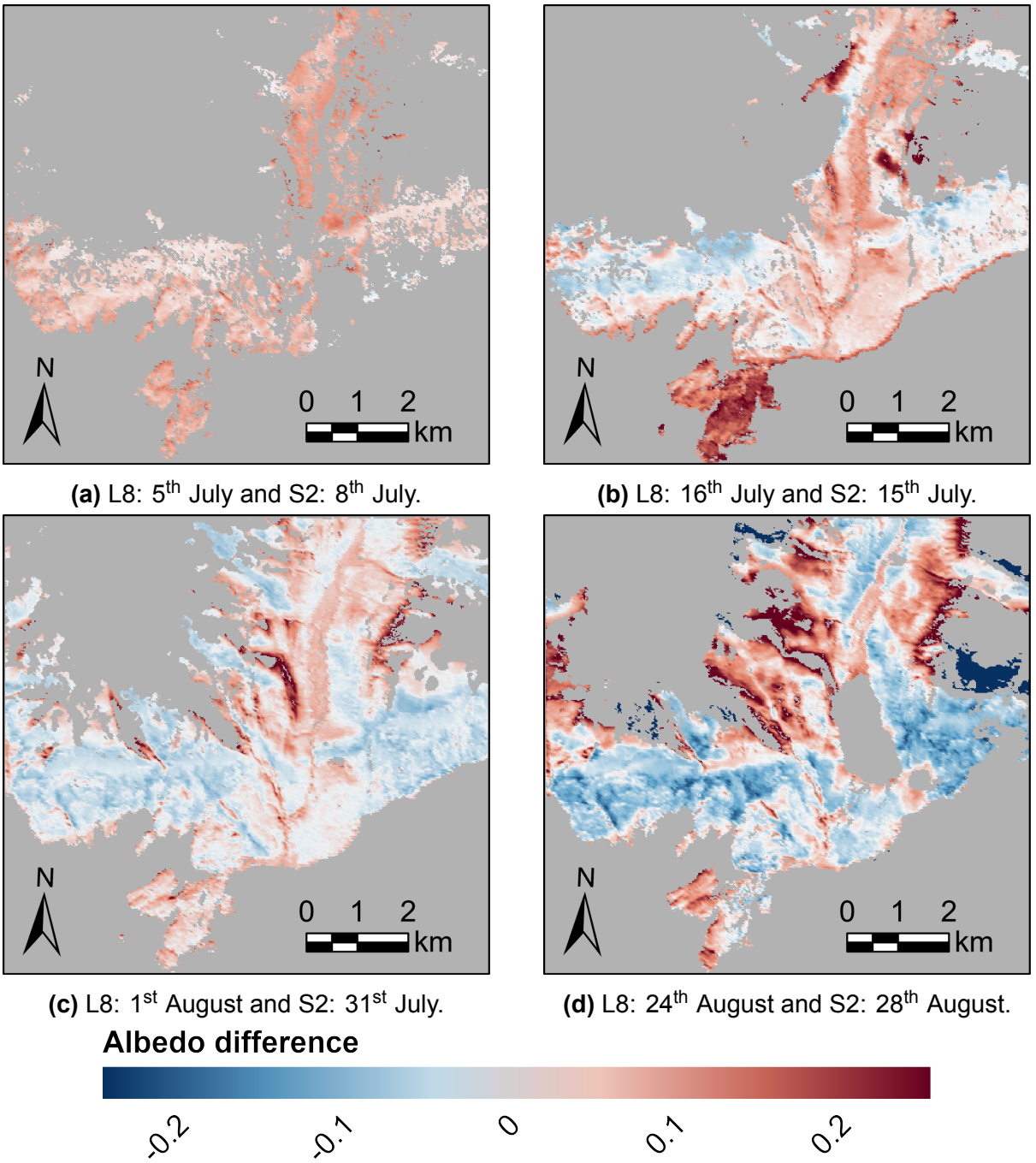

(a) L8: 5th July and S2: 8th July.

(b) L8: 16th July and S2: 15th July.

(c) L8: 1st August and S2: 31st July.

(d) L8: 24th August and S2: 28th August.

Figure 17: Albedo difference of L8 and S2 based albedo of selected dates in 2022. In each case, the L8 albedo was subtracted from the S2 albedo. Thus, red values indicate that S2 is higher than L8. On 24th August, a cloud shadow above *Kuup Ilua* was not detected, which led to lower values, which is visible in Figure 11 (h). This area was removed manually before analysing the albedo differences. No data pixles are displayed in grey. Albedo calculated with data from ESA, LAADS DAAC, LP DAAC and USGS.

of dates, S2 could explain the differences to a far larger extent than L8, whereas both sensors barely revealed any difference in comparison of the input bands. The day-wise order of the steps with comparison of the band-wise surface reflectance and white sky

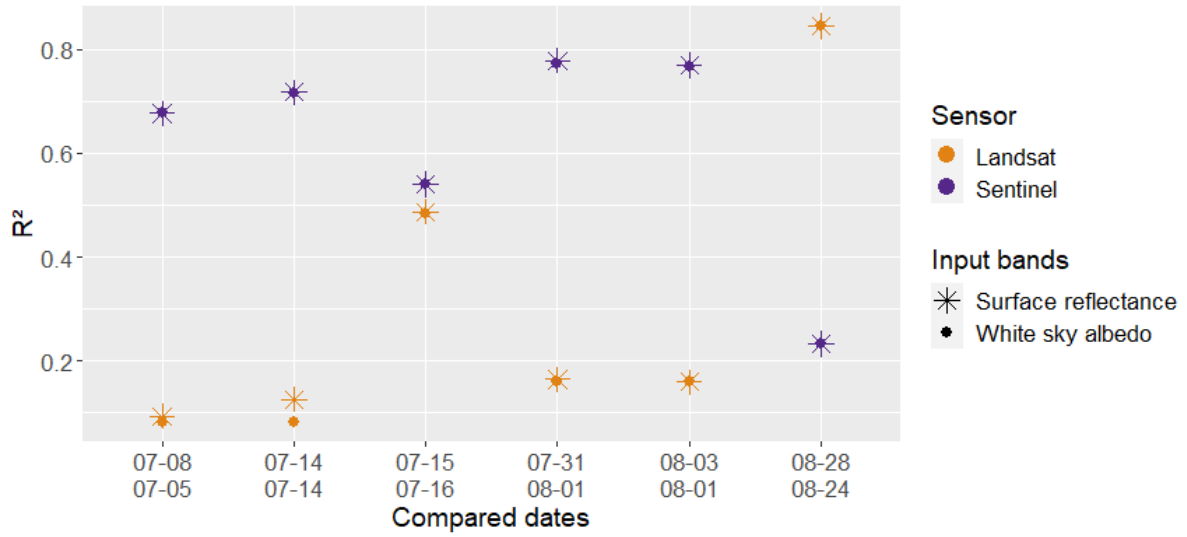

Figure 18: Coefficients of determination (R^2) of the step-wise multiple regression analysis of the albedo differences in 2022. In the separate models, the differences are explained by the sensors band-wise surface reflectance or white sky albedo. On the x-axis, the two compared dates are given in the format MM-DD, with the S2 date above the L8 date. Albedo calculated with data from ESA, LAADS DAAC, LP DAAC and USGS.

albedo is in the Appendix in Figure 22. L8 had varying bands as the first step but nearly the same order for the surface reflectance and white sky albedo bands. On the contrary, S2 had a more diverging order for the bands except the blue band, which was selected as step one in all S2 models.

5 Discussion

5.1 Temporal Variability of AWS Albedo

The monthly albedo at AWS2 showed a seasonal pattern. The high albedo values from October to May occurred due to the high albedo of snow in this period. Though snow depth, which I used in the correlation, does not causally influence albedo as snow cover does, a higher snow depth at AWS2 was an indicator for a higher snow cover in the sensor footprint. Thus, the correlation was acceptable to get a rough impression. The slightly decreasing trends of monthly albedo in November, October, April and May suggested that the snow period might shorten over time. This interpretation should be taken with caution because no significance could be determined due to the limited data availability. However, this is in line with Liu et al. (2023), who found that spring started earlier and autumn ended later in *Kuup Ilua* in model simulations under various climate

changes scenarios. As the interannual variability was relatively high in October and May in my data, the onset and end of the snow period varied from 2013 to 2022, which was also observed by LIU et al. (2023) from 2016 to 2020 in a S2 analysis. Though records are not yet available, the variability became apparent with the unusual late snow event in June 2023 (personal communication with NAALU (JULIANE) MØLGAARD from Qeqertarsuaq, 6th September 2023).

Compared to the annual amplitude, the seasonal change of monthly and daily albedo in the snow-free period was small. The monthly albedo from June to September stayed at a similar level without a visible or statistical trend over the ten years. This is in line with PLEKHANOVA et al. (2022), who assessed the mid-summer snow-free albedo in the Arctic with MODIS data for the period 2000–2021. They found that 82 % of the Arctic land surface did not exhibit a significant trend, which included the location of AWS2. While 14 % of the pan-Arctic area showed a positive trend in their analysis, 4 % showed a negative one. However, the significant changes over the whole study period were very low (median: 0.014) (PLEKHANOVA et al. 2022).

Within the snow-free period, the daily albedo followed approximately a quadratic function with a maximum around the beginning of August. The albedo increased in June and July independent from cloud cover. As Disko Island has dark soil, the increase of albedo can likely be explained by the covering effect of the vegetation. This effect has been discussed in previous studies (JUSZAK et al. 2014; BLOK et al. 2011). Towards autumn, the albedo decreased in six years and stayed at similar levels in four years. Vegetation changes might have led to some decrease in the second half of the vegetation period. Especially, *Betula nana* changes its colour from green to dark red and brown in the study area from August to September, which is depicted in Figure 4.

However, albedo increases with increasing SZA in theory, which was confirmed in models (WUTTKE et al. 2006; WANG et al. 2005). This was not observed in all studies when albedo decreased with increasing SZA or revealed no relation to SZA in cloudy conditions (WUTTKE et al. 2006; HUANG et al. 2019). In my analysis, the albedo decrease from August to September was reduced or disappeared when I removed days with a cloud cover > 30 %. Thus, the cloud cover likely dissolved the influence of the SZA on albedo to a certain extent in some years. In 2019, the albedo increased almost linearly for days with lower cloud cover. This indicates that the effect of vegetation on

the seasonal change of albedo is small and difficult to detect in the second half of the snow-free period. Whether the albedo increase in the first half of the snow-free period was rather linked to vegetation changes or SZA cannot be assessed with the available AWS2 data, but will be examined in Chapter 5.3.

5.2 Spatial Variability of Albedometer Measurements

The Albedometer measurements differed between surface characteristics, land cover classes and cloud cover. All Albedometer measurements varied between 0.05 and 0.28 with a daily median of 0.15 (29th August Arctic Station), 0.18 (30th August *Kuup Ilua* North) and 0.13 (8th September *Kuup Ilua* South). When considering individual measurements and their surface characteristics, these are roughly in line with values mentioned in literature. RASCHKE and OHMURA (2005) assessed the Arctic tundra albedo in summer from June to August. Their values for albedo ranged from 0.07 to 0.22 with a modal value of 0.15. Following the basic principles described in HUISSTEDEN (2020c), my measurements above open water were below 0.10. Vegetation mostly displayed albedo values below 0.20, though some light-coloured vegetation, e.g. lichens (HUISSTEDEN 2020c) led to higher values (0.22 to 0.28).

Previous studies have examined the effect of specific vegetation or shrub canopy on summer albedo in the Arctic. The green biomass increases the albedo to a certain extent as significant differences were found between wet sedge and tussock tundra (ECK et al. 1997) and barren ground and wetland tundra in comparison to other vegetation classes (BLOK et al. 2011). The canopy of shrubs can reduce the albedo as the radiation gets trapped in the structure. THOMPSON et al. (2004) showed this in their analysis with a decreasing albedo in a vegetation gradient from tundra to boreal forest. However, JUSZAK et al. (2014) found that the canopy effect in the tundra is small, whereas other factors such as soil type or the replaced vegetation could be more influential on the albedo in the context of shrubification. BLOK et al. (2011) found that a higher fractional cover of *Betula nana* was associated with a lower albedo, which WILLIAMSON et al. (2016) found for *Salix pulchra*. Contrary to that, *Betula glandulosa* reached comparable or higher albedo in comparison to *Carex*, *Dryas* and lichen sites without shrubs (WILLIAMSON et al. 2016). However, their *Betula glandulosa* site seemed to be influenced by other vegetation to a non-negligible extent as depicted in photos they supplied.

Thus, their finding about *Betula glandulosa* might rather be related to the set up of the pyranometer than the different *Betula* species compared to BLOK et al. (2011).

In comparison, my measurements of the same day are partly in line with the effects of vegetation and canopy discussed in literature. Points with vegetation covering surface water had a higher albedo near the river of *Kuup Ilua* North and in the wetland of *Kuup Ilua* South than points with less vegetation. The unexpected low albedo in the dry Patch 4 of *Kuup Ilua* South was probably caused by the vegetation colour as the dead *Cassiope* and the autumnal reddish brown *Betula nana* and *Vaccinium* contributed to a dark background colour. The vegetation likely also outweighed the influence of soil moisture in the water-saturated Patch 1 with a comparably high albedo. Contrary to the expected canopy effect, there were no significant differences of points with varying *Salix glauca* cover and height in *Kuup Ilua* South. At the time of the Albedometer measurements, the *Salix glauca* leaves were partly autumnal yellow or had fine white hairs, which might have opposed the decreasing effect of the canopy structure, which agrees with the finding of JUSZAK et al. (2014) that other factors than canopy complexity might be more influential. However, these interpretations of the vegetation should be considered with caution as the number of measurements was limited, the cloud conditions were not ideal in *Kuup Ilua* South and many spots were a mix of vegetation with quite different colour and structure.

Points with different field-assessed surface characteristics lay partly in the same land cover class from RUDD et al. (2021). Under cloudy conditions, the outgoing SWR was reduced to a larger extent than the incoming SWR compared to the clear-sky day, which can explain the generally lower albedo on the cloudy days. Based on the clear-sky measurements, the median per class was 0.11 for wet heath, 0.18 for fen and 0.19 for dry heath & grassland. These values are slightly below the field measurements by LANGER et al. (2011) in northern Siberia from 2007 and 2008, who detected 0.15 for wet and 0.20 for dry tundra sites. That the median wet heath value was below that of the dry heath & grassland matches the expectation that moisture decreases the albedo. However, as the vegetation at these points was different, it remained unclear, which was the dominating effect. In the fen class, described as water logged by KARAMI et al. (2018), the light colours of lichens, moss and *Eriophorum spec.* likely outweighed the decreasing effect of moisture as the class had rather high values. Unfortunately, I

had no vwc data from 30th August that could support or object that. All three classes had a comparable large range of the whiskers or outliers. This can be explained with the small-scale heterogeneity of the landscape and the resolution of the land cover classification as some points would better fit the description of another class.

5.3 Variability and Comparison of Satellite-based Albedo

Correlation with Indices

The albedo was significantly correlated to NDMI, NDVI and NDWI to varying extent. As NDVI and NDWI were highly correlated with each other, I refrained from analysing latter, because it would not offer new insights. As they were designed to map completely different features, I expected this. However, their correlation to albedo could have been more variable than just having a switched algebraic sign. In the class- and day-wise comparison of the NDMI's and NDVI's correlation to albedo, the correlation coefficients of the vegetation classes were generally higher and less randomly distributed than in the non-vegetation classes. In the vegetation classes both indices followed a similar pattern, which differed as follows. Dry heath & grassland had a predominantly weak to medium positive correlation. Copse & tall shrub had a weak correlation but changed its algebraic sign from negative in mid July to positive in August, when the positive correlation in the fen class increased from being weak to strong. Similarly, the mostly positive correlation in wet heath increased but then decreased again towards the end of the vegetation period.

The temporal change of the correlation between NDVI, the vegetation's greenness, and albedo supports some of the vegetation effects discussed in 5.2. As vegetation developed leaves in the first half of the vegetation period, its effect on increasing albedo when covering surface water, dark or wet ground had to develop. This applied to the fen and wet heath class with generally wet conditions. In the copse & tall shrub class, the change of algebraic sign could be linked to the canopy. In the beginning of the growing season when the leaves just started to develop, the canopy could exert its decreasing effect on albedo. Onwards the peak growing season, after the leaves fully covered the structure of the branches, the decreasing effect disappeared.

BLOK et al. (2011) did not observe a significant relationship between albedo and NDVI

in their field data. In their MODIS analysis, with regard to all land cover classes, only a study area in western Siberia revealed a significant negative relationship between maximum NDVI and minimum white sky albedo (Pearson's r = -0.65, $p < 0.05$). Their study regions in eastern Siberia, Alaska and Nunavut had a negative but not significant relationship (r = -0.46, -0.58 and -0.22, respectively, $p > 0.05$). Reasons that my results diverged from their findings could be related to the spatial resolution, as BLOK et al. (2011) used MODIS products with 250 and 500 m pixel size. Additionally, their setup with correlating maximum NDVI and minimum white sky albedo of a month-long period might have introduced a bias by provoking a negative relationship.

Moisture in soil or surface water generally decreases the albedo. High NDMI values indicate moist vegetation. Some background noise from soil moisture could occur (GAO 1996). However, I assumed this to be negligible as the fraction of bare soil was low in the vegetated areas and the soil of non-vegetated areas was mostly dry. Contrary to the general expectation of moisture decreasing albedo, the NDMI was predominantly positively correlated with albedo and followed a similar pattern as the coefficients of NDVI. This indicates that the moisture of the vegetation had no relevant influence on the albedo in my data. However, the summer was very rainy in 2022 and the study area generally has a sufficient water supply so that I had no comparison with vegetation experiencing drought stress. As drought stress influences leaf area, it could alter albedo of leaf-growing vegetation (AVETISYAN et al. 2021). GUAN et al. (2020) observed varying relationships between aridness, vegetation and albedo in different climate zones, which highlights again that the albedo-vegetation interaction is complex. Thus, the analysis could result in different findings when conducted over multiple summers, in regions with more variable moisture conditions or in another climate zone.

Temporal Variability

The albedo from L8 and S2 varied differently over time. While the scene-wide L8 mean albedo increased until the end of August, S2 reached its maximum in mid July. In the vegetation classes, the median albedo followed the scene-wide trend of the respective sensor. The standard deviations of both sensors tended to increase over time. Contrary to my expectation, that of L8 was 0.02 higher at the end of August even though S2 had a higher spatial resolution.

With regard to the influence of the SZA on albedo (WUTTKE et al. 2006; WANG et al.

2005), discussed in 5.1, the expected increase over time was notable in the L8 data. The increasing variability in L8, visible in the boxplots and supported by the statistical tests, could be linked to the SZA and some cloud cover at end of August. The S2 data fluctuated around 0.23 in July and August, which was not in agreement with the statistical test results that variances were not homogeneous and central tendencies differed significantly for most days. This mismatch was likely linked to the large sample size as the test assessed small differences as significant. However, these differences might not be large enough to be relevant in reality. Thus, it is questionable whether S2 could depict the seasonal increase of albedo in the vegetation period. In the September scene, when SZA was at its maximum, the S2 albedo decreased, likely caused by some cloud cover on that day (WUTTKE et al. 2006; HUANG et al. 2019).

Spatial Variability

In comparison of land cover classes independent of pixel size, their differences of albedo mean and standard deviation increased over time in the L8 data but less so for S2. In the vegetation classes of L8, copse & tall shrub had the highest (mean 0.17-0.28), and dry heath & grassland the lowest albedo (mean 0.16-0.23) for the majority of the observation period. This is not in line with the in Chapter 5.2 discussed effects of vegetation classes that shrubs could decrease albedo by trapping radiation in the canopy structure (THOMPSON et al. 2004; BLOK et al. 2011) and that dry tundra had a higher albedo than wet tundra (ECK et al. 1997; LANGER et al. 2011). However, in the analysis from BLOK et al. (2011), shrub tundra had a similar albedo as graminoid tundra, which is comparable to the class dry heath & grassland, in two of the four study areas, which again indicates that the effect of shrubs on albedo is complex. Thus, the positive climate forcing of shrubs, which has been discussed in literature (AARTSMA et al. 2021; PEARSON et al. 2013), likely varies on spatiotemporal scales. If I excluded fen and copse & tall shrub from my comparison, which had < 1000 pixels, it still remained puzzling that the mean albedo of wet heath was 0.01-0.02 above that of dry heath & grassland. This is also not in line with the Albedometer, where the median albedo of wet heath was below dry heath & grassland. A reason for this could be that the classes were unevenly distributed over varying aspect and slopes, which influenced the reflection geometry. A future analysis that considers aspect and slope could verify that.

In S2, the mean fen albedo was 0.01-0.04 above the other three quite similar vegetation classes, which does not fit the literature, either. A possible reason for both sensors could be their too coarse spatial resolution in this heterogeneous landscape. Sub-pixel size features that did not fit its land cover class likely biased the albedo. However, this does not explain the diverging albedo patterns of the same class in a sensor comparison or that L8's variability was higher though it had a coarser spatial resolution.

The statistical tests resulted in significant differences in variance and central tendencies between the vegetation classes. This has implications for models and vegetation changes. Assuming a fixed albedo of vegetation in models could cause uncertainty and vegetation changes could alter the energy budget of the landscape. However, due to the large sample size, the tests might have assessed small changes as significant, which were not relevant for reality.

In an interim conclusion, L8 seemed more suitable at displaying the local temporal and spatial variability for albedo than S2. The expected increase over time was visible in L8 but not in S2. Both sensors did not result in the expected land cover class albedo values and partly diverged from another. In the following, I discuss the extent of the sensor differences.

Effect of the BRDF Correction

In theory, the BRDF correction is necessary to achieve realistic albedo values, especially in regions or during time periods when the SZA is large (QU et al. 2015). In my analysis, the albedo and the nadir reflectance were generally similar (Pearson's r 0.98). Over time, thus with increasing SZA, the albedo was increasingly above the nadir reflectance. This is in line with several studies that found that the nadir reflectance often underestimated the surface albedo, which was dependent on scattering and viewing geometry (TILSTRA et al. 2021; LIU et al. 2020; ZHANG et al. 2018; LORENTE et al. 2018). For small SZA ($< 30\,°$), when geometric scattering dominated, the nadir reflectance tended to overestimate the albedo, while it tended to underestimate the albedo for large SZA ($> 50\,°$) ZHANG et al. (2018). In my data, the SZA was $> 50\,°$ from the end of July onwards but never below $30\,°$.

Within a scene, the offset of albedo to nadir reflectance increased with larger nadir reflectance values. This was likely related to the surface roughness. Higher albedo

or nadir reflectance values were mostly located in vegetated land cover classes, while lower values were represented in the classes abrasion surface and barren ground to a larger extent. Vegetation leads to volumetric scattering, so that the Lambertian assumption is less accurate in comparison to non-vegetated surfaces (LIU et al. 2020; LORENTE et al. 2018). This emphasises the necessity to apply the BRDF correction when investigating the surface albedo in Arctic tundra regions.

Assessment of non-changing Surfaces

The albedo of the assumed non-changing surfaces differed over time in L8 and S2 to a varying extent. The roof and stone shapes displayed a larger variability (standard deviation 0.03) and partly diverging trends in the sensor comparison. Reasons for that could be related to the tilt angle of the roof and the surface roughness of the stones. WANG, ZENDER, et al. (2016) investigated the bias on radiation fluxes and albedo caused by surface tilt. LAMARE et al. (2023) found that the effect of surface roughness on reflection is interdependent on SZA. Thus, the scattering effect of the roof and stone areas was susceptible to small changes in view and sun geometry. So, I could not validate them as suitable to assess the effect of the atmosphere on albedo. Shapes of the gravel area near the Heliport and of the soccer field varied less (standard deviation 0.01-0.03) and followed a similar path in the sensor comparison. If their surface properties were actually not changing, their variability over time approximately represented the atmospheric influence on albedo. However, no in-situ data over time were available for these areas that could validate this hypothesis. And both areas were likely exposed to some variation in surface properties, such as colour changes with wetness and stored moisture in the artificial lawn of the soccer field.

Comparison of Sensors

The satellite sensors displayed differences to the locally measured albedo, for all study sites and acquisition times where a comparison was possible. The comparison of the AWS2 and Albedometer resulted in a mean absolute deviation of 0.05. Reasons could be related to the various footprint size and sensor specific aspects as also the local sensors were subjected to uncertainties. The RMSE of L8 was 0.06 to the AWS2 as well as the Albedometer. This RMSE is larger than findings in literature that combined Landsat with MODIS BRDF. SHUAI et al. (2014) used Landsat TM and ETM+ in the Pacific Northwest region of the United States and achieved a RMSE below 0.02. However,

they applied narrow to broadband coefficients developed for Landsat TM and ETM+ with data from spectral libraries. WANG, ERB, et al. (2016) developed the coefficients used here, and calculated an RMSE of 0.02 for snow-free sites using L8 in burned study sites in Alaska's boreal forest. ERB et al. (2022) evaluated the L8 based albedo for the circumpolar domain, using the coefficients from WANG, ERB, et al. (2016). Considering all SZA they resulted in a RMSE of 0.05, which could be improved to 0.04 for SZA $< 70°$ (ERB et al. 2022). The RMSE increased when ERB et al. (2022) applied WANG, ERB, et al. (2016)'s coefficients in a larger region. This indicates that the coefficients might be fitted to conditions in the region they were designed for but could lead to larger uncertainties when applied in other regions. That might be one reason, why my L8 albedo resulted in a higher RMSE. For the comparison of L8 with the Albedometer data, I used the scene with the closest date, 24th August. Unfortunately, this day had a cloud shadow in *Kuup Ilua* North, which led to visibly lower values in that area. Thus, the agreement of L8 and the Albedometer might have been better on a clear-sky day.

For S2, my analysis revealed a RMSE of 0.04 for the AWS2 and 0.06 and 0.10 for the Albedometer. These values are above the findings in other studies. LI et al. (2018) developed the narrow to broadband coefficients separately for snow-covered and snow-free surfaces with study sites in the United States between 34 -48 °N. They resulted in a RMSE of 0.02, while the BRDF corrected albedo tended to underestimate the albedo of in-situ pyranometers (LI et al. 2018). BERTONCINI et al. (2022) applied their coefficients for snow-covered surfaces at the glacier Columbia Icefield in the Canadian Rockies (52.17 °N). They achieved a RMSE of 0.03. Opposite to LI et al. (2018), their albedo tended to overestimate the in-situ data (BERTONCINI et al. 2022). This supports the discussed impact of the BRDF correction depending on SZA and surface type.

In the comparison of L8 and S2, the differences in albedo varied over space and time. The RMSE was mostly 0.05-0.06 for compared dates, which is comparable with BARLETTA et al. (2022) who reported RMSE values of 0.04-0.05 for L8 and S2. With a median difference of 0.02, the S2 albedo was mostly above that of L8 in my data. This is not in line with studies that lacked a consideration of anisotropy. BARTMIŃSKI and SIŁUCH (2022) analysed the broadband nadir reflectance for agricultural areas in Poland, where L8 resulted in higher values than S2 on several days. Similarly, BARLETTA et al. (2022) found a higher mean nadir reflectance in L8 in urban areas of

Bari, Italy and Berlin, Germany. NAEGELI et al. (2017) took anisotropy into account and compared the L8 and S2 albedo of two Swiss glaciers. As in my analysis, S2 tended to be above L8 but their deviations were only minor so that they suggested the sensor combination was suitable (NAEGELI et al. 2017). Additionally, they compared the L8 and S2 albedo with Airborne Prism Experiment data, which offered 248 bands and 2 m spatial resolution, and analysed the influence of spectral and spatial resolution. They found that the spectral resolution was more influential on albedo than spatial resolution (NAEGELI et al. 2017).

The differences between L8 and S2 might have been related to a particular band. In my step-wise multiple regression analysis of sensor differences dependent on narrowband surface reflectance or white sky albedo, the S2 bands could explain the differences to a far larger extent than the L8 bands on four days. On one day, the sensors had a similar coefficient of determination; on one day the L8 bands explained the differences to a far larger extent than the S2 bands. The BRDF correction did not influence these results considerably. Strikingly, in each S2 model, the blue band could explain the differences to a greater extent than the other bands. The blue band is susceptible to atmospheric effects influencing scattering (WEN et al. 2019). The analysis had the limitation that the atmosphere likely changed considerably in the comparison of scenes from different dates. However, on 14th July, where the acquisition time was about half an hour apart, the S2 models also explained the difference to a greater extent (R^2 0.72 and 0.71; L8 R^2 0.13 and 0.08). Thus, this finding fits in the context of limitations of atmospheric correction in high latitudes, which was observed in studies that compared the L8 and S2 narrowband reflectance in the Arctic RUNGE and GROSSE (2019) and CHEN and ZHU (2022).

RUNGE and GROSSE (2019) analysed the surface reflectance of L8 and S2 at three sites in Eastern Siberia (62 - 73 °N). The blue band had the least correlation between the sensors, both for the acquired and the adjusted reflectance (Pearson correlation coefficient: blue 0.89, other bands 0.94-0.97) and a similar RMSE as the other bands (blue 0.01, other bands 0.01-0.02) (RUNGE and GROSSE 2019). Applying the 'Harmonized Landsat and Sentinel-2' product did not improve the agreement so that RUNGE and GROSSE (2019) recommended regionally-fitted adjustment parameters when using L8 and S2 interoperably. CHEN and ZHU (2022) compared the top of atmosphere (TOA)

and surface reflectance of L8 and S2 in Alaska (60 - 70 °N). The blue band had a comparably high coefficient of determination (blue 0.84, other bands 0.51-0.85) in the surface reflectance but, with the broad NIR band of S2, the highest RMSE (blue and broad NIR 0.10, other bands 0.04-0.09) (CHEN and ZHU 2022). For all bands, the agreement between sensors was generally smaller in the surface reflectance compared to TOA values (CHEN and ZHU 2022). This is line with the general knowledge that atmospheric correction is less accurate in high latitude regions (LI et al. 2020).

Summarising the discussed aspects of the BRDF and differences between L8 and S2, the following insights emerge. The BRDF correction had the same effect for both sensors as albedo was increasingly above nadir reflectance over time and with larger nadir reflectance. The effect size likely varied due to SZA and surface roughness. Both satellite sensors deviated to local pyranometer measurements. The differences between L8 and S2 could be explained by S2's blue band to a large extent, which suggested uncertainties in the atmospheric correction. Based on my previous finding that L8 was better in reproducing the temporal and spatial variability than S2, I conclude that L8 performed better in my analysis of albedo on Disko Island, Greenland.

5.4 Methodological Limitations and Outlook

Albedo measurements and the albedo derivation from satellite imagery are sensitive to environmental factors. The resulting methodological limitations of this thesis can be broadly separated into data quality, regional features and conceptional limitations.

The data quality was influenced by sensor specific aspects and by cloud cover. The Albedometer measurements might had some uncertainties caused by an imprecise levelling of the sensors, which was investigated in previous studies (WUTTKE et al. 2006; GRENFELL et al. 1994). Dust or water droplets could have influenced the AWS2 sensor, which I prevented for the Albedometer data collection by cleaning it before measuring. The weather conditions in summer 2022 severely limited the quantity of clear-sky days. Some cloud cover in the satellite imagery could not be avoided completely. The quality control for L8 failed to detect all cloud shadows, which was noticeable on 24th August with decreased albedo values for *Kuup Ilua*. Nevertheless, I decided to include this date as it was the highest-quality L8 scene available around the dates of the Albedometer data collection. In that regard, S2 had an advantage with its higher temporal resolu-

tion, as this increased the chance of clear-sky scenes. The MODIS BRDF product is provided daily but is calculated based on 16 days. Good BRDF data did not cover the whole AOI on each observation day, which could be related to cloud cover. Additionally, YANG et al. (2022) found that the temporal smoothing caused uncertainty. When deriving the direct radiation share, I used the global average AOT on days without good MODIS data. To get an impression of the uncertainty caused, I calculated the albedo of the day with the largest difference to the global average AOT (31st July: 0.198; global average: 0.120). The direct radiation share deviated by 7-12 %, but the albedo RMSE was only 0.0005. Thus, the lack of good AOT data caused negligible uncertainties.

Regional features that influenced uncertainty included the high latitude and the heterogeneous landscape. With its high latitude, the study area featured a rather high SZA. CHEN and ZHU (2022) found that a high SZA caused a bias in the surface reflectance as atmospheric correction is generally less accurate in these regions due to high SZAs (LI et al. 2020). The landscape in the AOI was heterogeneous on a small scale. Thus, the albedo of a satellite pixel or in the Albedometer footprint was an average of all sub-pixel size features and in some cases not representative for a specific, homogeneous surface unit. In the land cover classification, sub-pixel size features of a different class could not be addressed. This shortcoming became apparent as Albedometer points lay in a class that disagreed with the description of the field data collection. Further, the heterogeneous landscape had implications for the conceptional limitations, which is explained in the next paragraph.

The applied methodology for the satellite derived albedo showed conceptional limitations due to the combination with MODIS BRDF and due to the narrow to broadband conversion. As SHUAI et al. (2011) proposed, I combined MODIS with L8 and S2 based on the coverage of a surface reflectance class within a MODIS cell. Only ”pure” MODIS cells were used, where > 60 % were covered with one L8 or S2 class. Thus, the BRDF data for a class were influenced by other classes to a certain extent and not all L8 and S2 classes had BRDF data. The lack of BRDF data led to a reduction of data, which became apparent when I changed the spatial resolution of S2. At first, I loaded the VIS bands in the available 10 m pixel size. Afterwards, I loaded them in 20 m pixel size, in which the broad NIR and SWIR bands were available. For the coarser resolution, the albedo result covered a larger proportion of the AOI, especially on 31st July 2022. In

the classification of surface reflectance, I chose to take six classes in order to limit data loss, which I expected with more classes in the heterogeneous landscape. BERTONCINI et al. (2022) proposed an iterative procedure to determine the best number of classes on a daily basis and found that the number of classes led to uncertainties in albedo of < 0.05. Thus, some uncertainties in my analysis could be related to the number of classes, which could be improved by more classes at cost of spatial coverage.

For the narrow to broadband conversion of albedo, I applied coefficients from other studies specifically developed for L8 and S2. I thereby eliminated the error which could have occurred with coefficients designed for a different sensor because band shifts in a newer generation, e.g. from Landsat could increase uncertainty (NAEGELI et al. 2017). However, the applied coefficients were derived in a different region (L8 Alaska, S2 Contiguous United States). Using them in Greenland likely caused some uncertainty due to differences in atmospheric conditions like aerosols. This was probably a larger issue for S2 with coefficients from the mid-latitudes.

The above mentioned challenges in the derivation of satellite-based albedo and in the comparability of L8 and S2 should be considered in future analyses. Challenges in the context of the high latitude and SZA, could be addressed by adding a SZA correction in the preprocessing (TRAVERSA et al. 2021) or by applying a TOA based method as CHEN and ZHU (2022) recommended. The analysis could be modified to gain an intensified comprehension of the albedo-land surface feedback in summer. As the reflectance varies across the spectrum, a separate analysis of NDVI and albedo in the VIS, NIR and SWIR part of the spectrum could contribute to our understanding of the relationship between albedo and different vegetation.

6 Summary and Conclusion

The albedo is an important component in the energy budget and is influenced by surface characteristics, the sun and view geometry as well as the atmospheric state. In the Arctic, in-situ observations are limited but satellite remote sensing offers nearly continuous observations. However, nadir-viewing satellites often do not achieve realistic albedo values, which can be overcome by including BRDF data from multi-angular observation platforms. In this thesis, I evaluated how the land surface albedo varied on

spatial and temporal scales during the snow-free period in the southern tip of Disko Island in West Greenland. I analysed AWS data from 2013 to 2022 to examine the temporal variability and conducted albedo measurements with a mobile sensor in 2022 to assess the spatial heterogeneity. I derived the L8 and S2 based albedo with inclusion of MODIS BRDF and narrow to broadband conversion for the period of June to September 2022. In the data analysis, I examined the temporal and spatial variability in the satellite albedo with regard to different vegetation classes and analysed the effect of the BRDF and the agreement of L8 and S2.

Due to climate change, shrubs spread polewards in the Arctic and are expected to continue to do so in the near-future. As a negative relationship between shrub height or abundance to albedo was observed in summer, some studies argued that shrubs could cause a positive climate forcing. In my analysis, the albedo of shrubs was not notably smaller than other vegetation types but partly 0.01-0.05 above them in both the mobile measurements and the satellite-derived albedo. The satellite-based albedo revealed temporally variable, significant correlations of albedo and NDVI and NDMI in all vegetation classes. However, the correlation in the class copse & tall shrub was only medium or weak and partly positive. This agrees with previous studies that found that it is not clear to what extent shrubification actually alter the summer time albedo and the micro-climate on varying spatiotemporal scales. Thus, there is a need for a deeper understanding of the role of shrubs in albedo feedback mechanisms entailing thorough field data that serves as a foundation for validating models and satellite data.

In the field of Earth observation, it has become of increasing interest to combine data from different satellite sensors to produce longer time series or higher spatiotemporal resolutions. Land surface models have failed to reproduce the observed seasonal variability of albedo in the snow-free tundra, which implies uncertainties in climate projections. In my analysis, the BRDF corrected albedo was on average 0.01 higher than nadir reflectance. L8 was better in reproducing the expected temporal and spatial variability of albedo than S2, which displayed less variability and seemed to be more sensitive to atmospheric effects. In order to ensure relevant outcomes, BRDF and TOA data should be implemented when analysing albedo in the snow-free tundra and when jointly using L8 and S2 in high latitude regions to overcome the bias of atmospheric effects.

Acknowledgements

The success of this thesis was only possible with the support and encouragement of my supervisors Simone Stuenzi and Julia Boike and the SPARC group at the Alfred Wegener Institute, Helmholtz Centre for Polar and Marine Research. I am very grateful to Julia for giving me the opportunity to join her on expedition for this thesis. An important thank you to Bill Cable and Niko Bornemann for technical and logistical support with the albedometer before, during and after the expedition. Thanks to several people for the successful field experience and the good mood despite the rain: Julia, Simone, Niko, Brian Groenke, Lars Kutzbach (Universität Hamburg), Torsten Sachs (German Research Centre for Geosciences) and the team of the Arctic Station, University of Copenhagen in Qeqertarsuaq (arktiskstation.ku.dk). After the expedition the SPARC group gave me a warm welcome and supported me with valuable advice regarding questions, data analysis, writing and the poster presentation at the European Conference on Permafrost. For that, a special thanks to Inge Grünberg and Jennika Hammar and my peers Marie Rolf, Maybrit Goldau, Luisa Näke and Daniela Hollenbach.

Data Credit

The basemap was supplied by GOOGLE EARTH and OPENSTREETMAP CONTRIBUTORS (https://www.openstreetmap.org/copyright). Landsat 8 Collection 2 Level 2 data sets courtesy of the USGS (https://www.usgs.gov/.) The S2 MSIL2A data set, produced from ESA remote sensing data, was retrieved from the Copernicus Open Access Hub and the Copernicus Data Space Ecosystem. The MODIS/Terra+Aqua BRDF/Albedo Model Parameters Daily L3 Global, version 6.1 data sets were acquired from NASAs LP DAAC, located at the USGS Earth Resources Observation and Science (EROS) Center in Sioux Falls, South Dakota (https://lpdaac.usgs.gov/). The MODIS/Terra Aerosol 5-Min L2 Swath 10km and the MODIS/Terra Aerosol Cloud Water Vapor Ozone Daily L3 Global 1 Deg. CMG data sets were acquired from the LAADS DAAC, located in the Goddard Space Flight Center in Greenbelt, Maryland (https://ladsweb.nascom.nasa.gov/). The SZA of the Albedometer field data collection was estimated with an solar calculator provided by the National Oceanic and Atmospheric Administration Global Monitoring Laboratory, Boulder, Colorado, USA (https://gml.noaa.gov). During the imagery processing, data from DANISH AGENCY FOR DATA SUPPLY AND INFRASTRUCTURE (2023) were used. Weather station data from the Greenland Ecosystem Monitoring Programme were provided by the Department of Bioscience, Aarhus University, Denmark in collaboration with Department of Geosciences and Natural Resource Management, Copenhagen University, Denmark and Asiaq – Greenland Survey, Nuuk, Greenland. The ArcticDEM was provided by the Polar Geospatial Center under NSF-OPP awards 1043681, 1559691, and 1542736. The land cover classification data were kindly provided by RUDD et al. (2021).

References

AARTSMA, PETER, JOHAN ASPLUND, ARVID ODLAND, STEFANIE REINHARDT, and HANS RENSSEN (2021). “Microclimatic comparison of lichen heaths and shrubs: shrubification generates atmospheric heating but subsurface cooling during the growing season”. In: *Biogeosciences* 18.5, pp. 1577–1599. DOI: 10.5194/bg-18-1577-2021.

ALFRED WEGENER INSTITUTE, HELMHOLTZ CENTRE FOR POLAR AND MARINE RESEARCH (2022). *World Radiation Monitoring Center - Baseline Surface Radiation Network - Objectives*. https://bsrn.awi.de/project/objectives/. Last access 5-February-2024.

AVETISYAN, DANIELA, DENITSA BORISOVA, and EMILIYA VELIZAROVA (2021). “Integrated Evaluation of Vegetation Drought Stress through Satellite Remote Sensing”. In: *Forests* 12.8, Art. No. 974. DOI: 10.3390/f12080974.

BARLETTA, CARLO, ALESSANDRA CAPOLUPO, and EUFEMIA TARANTINO (2022). “Exploring the Potentialities of Landsat 8 and Sentinel-2 Satellite Data for Estimating the Land Surface Albedo in Urban Areas Using GEE Platform”. In: *Computational Science and Its Applications – ICCSA 2022 Workshops*. Ed. by Osvaldo Gervasi, Beniamino Murgante, Sanjay Misra, Ana Maria A. C. Rocha, and Chiara Garau. Cham, Switzerland, pp. 435–449. DOI: 10.1007/978-3-031-10545-6_30.

BARTMIŃSKI, PIOTR and MARCIN SIŁUCH (2022). “Mapping the albedo of the active surface at different stages of the growing season using data from various sources”. In: *Remote Sensing Applications: Society and Environment* 28, Art. No. 100818. DOI: 10.1016/j.rsase.2022.100818.

BERTONCINI, ANDRÉ, CAROLINE AUBRY-WAKE, and JOHN W. POMEROY (2022). “Large-area high spatial resolution albedo retrievals from remote sensing for use in assessing the impact of wildfire soot deposition on high mountain snow and ice melt”. In: *Remote Sensing of Environment* 278, Art. No. 113101. DOI: 10.1016/j.rse.2022.113101.

BISKABORN, BORIS K., SHARON L. SMITH, JEANNETTE NOETZLI, BEIDRUN MATTHES, GONÇALO VIEIRA, DMITRY A. STRELETSKIY, PHILIPPE SCHOENEICH, VLADIMIR E. ROMANOVSKY, ANTONI G. LEWKOWICZ, ANDREY ABRAMOV, MICHEL ALLARD, JULIA BOIKE, WILLIAM L. CABLE, BANNE H. CHRISTIANSEN, REYNALD DELALOYE, BERNHARD DIEKMANN, DMITRY DROZDOV, BERND ETZELMÜLLER, GUIDO GROSSE, MAURO GUGLIEL-

MIN, THOMAS INGEMAN-NIELSEN, KETIL ISAKSEN, MAMORU ISHIKAWA, MARGARETA JOHANSSON, BALLDOR JOHANNSSON, ANSEOK JOO, DMITRY KAVERIN, ALEXANDER KHOLODOV, PAVEL KONSTANTINOV, TIM KRÖGER, CHRISTOPHE LAMBIEL, JEAN-PIERRE LANCKMAN, DONGLIANG LUO, GALINA MALKOVA, IAN MEIKLEJOHN, NATALIA MOSKALENKO, MARC OLIVA, MARCIA PHILLIPS, MIGUEL RAMOS, A. BRITTA K. SANNEL, DMITRII SERGEEV, CATHY SEYBOLD, PAVEL SKRYABIN, ALEXANDER VASILIEV, QINGBAI WU, KENJI YOSHIKAWA, MIKHAIL ZHELEZNYAK, and HUGUES LANTUIT (2019). "Permafrost is warming at a global scale". In: *Nature Communications* 10, Art. No. 264. DOI: 10.1038/s41467-018-08240-4.

BLOK, DAAN, GABRIELA SCHAEPMAN-STRUB, HARM BARTHOLOMEUS, MONIQUE M.P.D. HEIJMANS, TROFIM C. MAXIMOV, and FRANK BERENDSE (2011). "The response of Arctic vegetation to the summer climate: relation between shrub cover, NDVI, surface albedo and temperature". In: *Environmental Research Letters* 6.3, Art. No. 035502. DOI: 10.1088/1748-9326/6/3/035502.

BONAFONI, STEFANIA and ALIIHSAN SEKERTEKIN (2020). "Albedo Retrieval From Sentinel-2 by New Narrow-to-Broadband Conversion Coefficients". In: *IEEE Geoscience and Remote Sensing Letters* 17.9, pp. 1618–1622. DOI: 10.1109/LGRS.2020.2967085.

BRENNING, ALEXANDER, DONOVAN BANGS, and MARC BECKER (2022). *RSAGA: SAGA Geoprocessing and Terrain Analysis*. R package version 1.4.0. https://CRAN.R-project.org/package=RSAGA.

CAMPBELL SCIENTIFIC, INC., ed. (2024). *CNR4 Net Radiometer. Product Manual*. Version January 2024. Logan, UT, USA. https://s.campbellsci.com/documents/us/manuals/cnr4.pdf. Last access 31-January-2024.

CANADELL, JOSEP G.and PEDRO M.S. MONTEIRO, MARCOS H. COSTA, LETICIA COTRIM DA CUNHA, PETER M. COX, ALEXEY V. ELISEEV, STEPHANIE HENSON, MASAO ISHII, SAMUEL JACCARD, CHARLES KOVEN, ANNALEA LOHILA, PRABIR K. PATRA, SHILONG PIAO, JOERI ROGELJ, STEPHEN SYAMPUNGANI, SÖNKE ZAEHLE, and KIRSTEN ZICKFELD (2021). "Global Carbon and other Biogeochemical Cycles and Feedbacks". In: *Climate Change 2021: The Physical Science Basis. Contribution of Working Group I to the Sixth Assessment Report of the Intergovernmental Panel on Climate Change*. Ed. by V.and P. Zhaiand A. Piraniand S.L. Connorsand C. Péanand S. Bergerand N. Caudand Y. Chenand L. Goldfarband M.I. Gomisand M. Huangand K. Leitzelland E. Lonnoyand J.B.R. Matthewsand T.K. Maycockand T. Waterfieldand O. Yelekçiand

R. Yuand Masson-Delmotte and B. Zhou. Cambridge, United Kingdom and New York, NY, USA. Chap. 5, pp. 673–816. DOI: 10.1017/9781009157896.007.

CHALMERS, JAMES A., T. CHRISTOPHER R. PULVERTAFT, CHRISTIAN MARCUSSEN, and ASGER K. PEDERSEN (1999). "New insight into the structure of the Nuussuaq Basin, central West Greenland". In: *Marine and Petroleum Geology* 16.3, pp. 197–224. DOI: 10.1016/S0264-8172(98)00077-4.

CHEN, JIANG and WEINING ZHU (2022). "Comparing Landsat-8 and Sentinel-2 top of atmosphere and surface reflectance in high latitude regions: case study in Alaska". In: *Geocarto International* 37.20, pp. 6052–6071. DOI: 10.1080/10106049.2021.1924295.

CONRAD, OLAF, BENJAMIN BECHTEL, MERLE BOCK, HELGE DIETRICH, ELKE K. FISCHER, LARS GERLITZ, JAN WEHBERG, VOLKER WICHMANN, and JÜRGEN BÖHNER (2015). "System for Automated Geoscientific Analyses (SAGA)". In: *Geoscientific Model Development* 8.7, pp. 1991–2007. DOI: 10.5194/gmd-8-1991-2015.

COPERNICUS (2022a). *Copernicus Sentinel data*. https://scihub.copernicus.eu. Processed by ESA. Last access 16-July-2023.

COPERNICUS (2022b). *Copernicus Sentinel data*. https://dataspace.copernicus.eu/explore-data. Processed by ESA. Last access 15-October-2023.

D'IMPERIO, LUDOVICA, MARIE F. ARNDAL, CECILIE S. NIELSEN, BO ELBERLING, and INGER K. SCHMIDT (2018). "Fast Responses of Root Dynamics to Increased Snow Deposition and Summer Air Temperature in an Arctic Wetland". In: *Frontiers in Plant Science* 9, Art. No. 1258. DOI: 10.3389/fpls.2018.01258.

DANISH AGENCY FOR DATA SUPPLY AND INFRASTRUCTURE (2023). *Greenland coast*. https://dataforsyningen.dk/. Last access 02-February-2023.

DEUTSCHER WETTERDIENST (2021). *Surface Radiation and Albedo*. https://www.cmsaf.eu/EN/Overview/OurProducts/Surface_Radiation_Albedo/Surface_Radiation_Products_node.html. Last access 9-July-2023.

ECK, THOMAS F., DONALD W. DEERING, and LEE A. VIERLING (1997). "Arctic tundra albedo and its estimation from spectral hemispheric reflectance". In: *International Journal of Remote Sensing* 18.17, pp. 3535–3549. DOI: 10.1080/014311697216784.

EICHLER, SARAH E. (2022). "Portable apparatus for high spatial and temporal resolution of in situ real-time surface albedo measurement in agricultural fields". In: *Environmental Science: Advances* 1 (3), pp. 297–304. DOI: 10.1039/D1VA00051A.

ENVIRONMENTAL SYSTEMS RESEARCH INSTITUTE (2024). *ArcGIS Pro*. https://www.esri.com/en-us/arcgis/products/arcgis-pro/overview. Last access 7-February-2024.

ERB, ANGELA M., ZHAN LI, QINGSONG SUN, IAN PAYNTER, ZHUOSEN WANG, and CRYSTAL B. SCHAAF (2022). "Evaluation of the Landsat-8 Albedo Product across the Circumpolar Domain". In: *Remote Sensing* 14.21, Art. No. 5320. DOI: 10.3390/rs14215320.

ESA (2015). *Sentinel-2 User Handbook*. https://sentinel.esa.int/documents/247904/685211/Sentinel-2_User_Handbook. Last access 9-July-2023.

ESA (2020). *Methods*. http://www.globalbedo.org/methods.php. Last access 9-July-2023.

FENG, SHUNAN, JOSEPH MITCHELL COOK, ALEXANDRE MAGNO ANESIO, LIANE G. BENNING, and MARTYN TRANTER (2023). "Long time series (1984–2020) of albedo variations on the Greenland ice sheet from harmonized Landsat and Sentinel 2 imagery". In: *Journal of Glaciology* 69.277, pp. 1225–1240. DOI: 10.1017/jog.2023.11.

FORD, JAMES D. and CHRISTINA GOLDHAR (2012). "Climate change vulnerability and adaptation in resource dependent communities: a case study from West Greenland". In: *Climate Research* 54.2, pp. 181–196. DOI: 10.3354/cr01118.

GALLET, JEAN-CHARLES, FLORENT DOMINE, LUC ARNAUD, GHISLAIN PICARD, and JOEL SAVARINO (2011). "Vertical profile of the specific surface area and density of the snow at Dome C and on a transect to Dumont D'Urville, Antarctica – albedo calculations and comparison to remote sensing products". In: *The Cryosphere* 5.3, pp. 631–649. DOI: 10.5194/tc-5-631-2011.

GAO, BO-CAI (1996). "NDWI—A normalized difference water index for remote sensing of vegetation liquid water from space". In: *Remote Sensing of Environment* 58.3, pp. 257–266. DOI: 10.1016/S0034-4257(96)00067-3.

GEM (2023a). *ClimateBasis Disko - Precipitation - Precipitation - 60min sample (mm)*. Asiaq – Greenland Survey, Nuuk, Greenland. DOI: 10.17897/638X-3Z89.

GEM (2023b). *GeoBasis Disko - Meteorology - AS-CloudCover*. Department of Bioscience, Aarhus University, Denmark; Department of Geosciences, Natural Resource Management, Copenhagen University, Denmark; and Asiaq – Greenland Survey, Nuuk, Greenland. DOI: 10.17897/NJTX-6M44.

GEM (2023c). *GeoBasis Disko - Meteorology - AWS2-Meteorology*. Department of Bioscience, Aarhus University, Denmark; Department of Geosciences, Natural Re-

source Management, Copenhagen University, Denmark; and Asiaq – Greenland Survey, Nuuk, Greenland. DOI: 10.17897/CSZT-F010.

GEM (2023d). *GeoBasis Disko - Snow - AWS2-SnowDepth*. Department of Bioscience, Aarhus University, Denmark; Department of Geosciences, Natural Resource Management, Copenhagen University, Denmark; and Asiaq – Greenland Survey, Nuuk, Greenland. DOI: 10.17897/SCXW-S288.

GOOGLE EARTH and OPENSTREETMAP CONTRIBUTORS (2023). *[Integrated as web map in ArcGIS Pro]*. http://mt0.google.com/vt/lyrs=s&hl=en&x={x}&y={y}&z={z}. Last access 23-July-2023.

GRENFELL, THOMAS C. (2011). "Albedo". In: *Encyclopedia of Snow, Ice and Glaciers*. Ed. by Vijay P. Singh, Pratap Singh, and Umesh K. Haritashya. Dordrecht, The Netherlands, pp. 23–35. DOI: 10.1007/978-90-481-2642-2_14.

GRENFELL, THOMAS C., STEPHEN G. WARREN, and PETER C. MULLEN (1994). "Reflection of solar radiation by the Antarctic snow surface at ultraviolet, visible, and near-infrared wavelengths". In: *Journal of Geophysical Research: Atmospheres* 99.D9, pp. 18669–18684. DOI: doi.org/10.1029/94JD01484.

GRID-ARENDAL/NUNATARYUK (2020). *Permafrost in the Northern Hemisphere*. https://www.grida.no/resources/13519. Last access 21-December-2023.

GUAN, YANLONG, HONGWEI LU, CHUANG YIN, YUXUAN XUE, YELIN JIANG, YU KANG, LI HE, and JANNE HEISKANEN (2020). "Vegetation response to climate zone dynamics and its impacts on surface soil water content and albedo in China". In: *Science of The Total Environment* 747, Art. No. 141537. DOI: 10.1016/j.scitotenv.2020.141537.

HENDERSON-SELLERS, ANN and M. F. WILSON (1983). "Surface albedo data for climatic modeling". In: *Reviews of Geophysics* 21.8, pp. 1743–1778. DOI: 10.1029/RG021i008p01743.

HOLLESEN, JØRGEN, AGATA BUCHWAL, GRZEGORZ RACHLEWICZ, BIRGER U. HANSEN, MARC O. HANSEN, OLE STECHER, and BO ELBERLING (2015). "Winter warming as an important co-driver for *Betula nana* growth in western Greenland during the past century". In: *Global Change Biology* 21.6, pp. 2410–2423. DOI: 10.1111/gcb.12913.

HUANG, CHUAN J., FANGLI QIAO, SIYU CHEN, YUHUAN XUE, and JINGSONG GUO (2019). "Observation and Parameterization of Broadband Sea Surface Albedo". In: *Journal of Geophysical Research: Oceans* 124.7, pp. 4480–4491. DOI: 10.1029/2018JC014444.

HUISSTEDEN, JACOBUS VAN (2020a). “Introduction”. In: *Thawing Permafrost: Permafrost Carbon in a Warming Arctic*. Cham, Switzerland. Chap. 1, pp. 1–50. DOI: 10.1007/978-3-030-31379-1_1.

HUISSTEDEN, JACOBUS VAN (2020b). “Permafrost Carbon Quantities and Fluxes”. In: *Thawing Permafrost: Permafrost Carbon in a Warming Arctic*. Cham, Switzerland. Chap. 4, pp. 179–274. DOI: 10.1007/978-3-030-31379-1_4.

HUISSTEDEN, JACOBUS VAN (2020c). “The Energy Balance of Permafrost Soils and Ecosystems”. In: *Thawing Permafrost: Permafrost Carbon in a Warming Arctic*. Cham, Switzerland. Chap. 2, pp. 51–106. DOI: 10.1007/978-3-030-31379-1_2.

HUISSTEDEN, JACOBUS VAN (2020d). “Vegetation Change”. In: *Thawing Permafrost: Permafrost Carbon in a Warming Arctic*. Cham, Switzerland. Chap. 6, pp. 367–432. DOI: 10.1007/978-3-030-31379-1_6.

HUKSEFLUX, THERMAL SENSORS B.V. (2002). *USER MANUAL SRA01, Second class albedometer*. Delft, The Netherlands.

IPA (n.d.). *What is Permafrost?* https://www.permafrost.org/what-is-permafrost/. Last access 22-August-2023.

JUSZAK, INGE, ANGELA M. ERB, TROFIM C. MAXIMOV, and GABRIELA SCHAEPMAN-STRUB (2014). “Arctic shrub effects on NDVI, summer albedo and soil shading”. In: *Remote Sensing of Environment* 153, pp. 79–89. DOI: 10.1016/j.rse.2014.07.021.

KARAMI, MOJTABA, ANDREAS WESTERGAARD-NIELSEN, SIGNE NORMAND, URS A. TREIER, BO ELBERLING, and BIRGER U. HANSEN (2018). “A phenology-based approach to the classification of Arctic tundra ecosystems in Greenland”. In: *ISPRS Journal of Photogrammetry and Remote Sensing* 146, pp. 518–529. DOI: 10.1016/j.isprsjprs.2018.11.005.

KINNE, STEFAN (2019). “The MACv2 aerosol climatology”. In: *Tellus B: Chemical and Physical Meteorology* 71.1, Art. No. 1623639. DOI: 10.1080/16000889.2019.1623639.

KOKHANOVSKY, ALEXANDER A. (2021). “The Broadband Albedo of Snow”. In: *Frontiers in Environmental Science* 9, Art. No. 757575. DOI: 10.3389/fenvs.2021.757575.

LAMARE, MAXIM L., JOHN D. HEDLEY, and MARTIN D. KING (2023). “The effects of surface roughness on the calculated, spectral, conical–conical reflectance factor as an alternative to the bidirectional reflectance distribution function of bare sea ice”. In: *The Cryosphere* 17.2, pp. 737–751. DOI: 10.5194/tc-17-737-2023.

LANGER, MORITZ, SEBASTIAN WESTERMANN, SINA MUSTER, KONSTANZE PIEL, and JULIA BOIKE (2011). “The surface energy balance of a polygonal tundra site in northern Siberia – Part 1: Spring to fall”. In: *The Cryosphere* 5.1, pp. 151–171. DOI: 10.5194/tc-5-151-2011.

LANTZ, BJÖRN (2013). “The large sample size fallacy”. In: *Scandinavian Journal of Caring Sciences* 27.2, pp. 487–492. DOI: 10.1111/j.1471-6712.2012.01052.x.

LEVY, ROB, CHRISTINA HSU, and et al. (2015). *MODIS Atmosphere L2 Aerosol Product. MOD04_L2*. NASA MODIS Adaptive Processing System, Goddard Space Flight Center, USA. DOI: 10.5067/MODIS/MOD04_L2.061. Last access 28-August-2023.

LI, HAO, XIANQIANG HE, YAN BAI, PALANISAMY SHANMUGAM, YOUNG-JE PARK, JIA LIU, QIANKUN ZHU, FANG GONG, DIFENG WANG, and HAIQING HUANG (2020). “Atmospheric correction of geostationary satellite ocean color data under high solar zenith angles in open oceans”. In: *Remote Sensing of Environment* 249, Art. No. 112022. DOI: 10.1016/j.rse.2020.112022.

LI, ZHAN, ANGELA M. ERB, QINGSONG SUN, YAN LIU, YANMIN SHUAI, ZHUOSEN WANG, PETER BOUCHER, and CRYSTAL B. SCHAAF (2018). “Preliminary assessment of 20-m surface albedo retrievals from sentinel-2A surface reflectance and MODIS/VIIRS surface anisotropy measures”. In: *Remote Sensing of Environment* 217, pp. 352–365. DOI: 10.1016/j.rse.2018.08.025.

LIANG, SHUNLIN (2001). “Narrowband to broadband conversions of land surface albedo I: Algorithms”. In: *Remote Sensing of Environment* 76.2, pp. 213–238. DOI: 10.1016/S0034-4257(00)00205-4.

LIU, SONG, PIETER VALKS, GAIA PINARDI, JIAN XU, ATHINA ARGYROULI, RONNY LUTZ, L. GIJSBERT TILSTRA, VINCENT HUIJNEN, FRANÇOIS HENDRICK, and MICHEL VAN ROOZENDAEL (2020). “An improved air mass factor calculation for nitrogen dioxide measurements from the Global Ozone Monitoring Experiment-2 (GOME-2)”. In: *Atmospheric Measurement Techniques* 13.2, pp. 755–787. DOI: 10.5194/amt-13-755-2020.

LIU, YIJING, PEIYAN WANG, BO ELBERLING, and ANDREAS WESTERGAARD-NIELSEN (2023). “Drivers of contemporary and future changes in Arctic seasonal transition dates for a tundra site in coastal Greenland”. In: *Global Change Biology* 30.1, Art. No. e17118. DOI: 10.1111/gcb.17118.

LORENTE, ALBA, K. FOLKERT BOERSMA, PIET STAMMES, L. GIJSBERT TILSTRA, ANDREAS RICHTER, HUAN YU, SAID KHARBOUCHE, and JAN-PETER MULLER (2018). "The importance of surface reflectance anisotropy for cloud and NO_2 retrievals from GOME-2 and OMI". In: *Atmospheric Measurement Techniques* 11.7, pp. 4509–4529. DOI: 10.5194/amt-11-4509-2018.

LP DAAC (n.d.). *MODIS Overview.* https://lpdaac.usgs.gov/data/get-started-data/collection-overview/missions/modis-overview/. Last access 02-August-2023.

LUCHT, WOLFGANG, CRYSTAL B. SCHAAF, and ALAN H. STRAHLER (2000). "An algorithm for the retrieval of albedo from space using semiempirical BRDF models". In: *IEEE Transactions on Geoscience and Remote Sensing* 38.2, pp. 977–998. DOI: 10.1109/36.841980.

NAEGELI, KATHRIN, ALEXANDER DAMM, MATTHIAS HUSS, HENDRIK WULF, MICHAEL SCHAEPMAN, and MARTIN HOELZLE (2017). "Cross-Comparison of Albedo Products for Glacier Surfaces Derived from Airborne and Satellite (Sentinel-2 and Landsat 8) Optical Data". In: *Remote Sensing* 9.2, Art. No. 110. DOI: 10.3390/rs9020110.

NASA (2023a). *AppEEARS*. https://appeears.earthdatacloud.nasa.gov/. Last access 22-July-2023.

NASA (2023b). *Find Data - LAADS DAAC*. https://ladsweb.modaps.eosdis.nasa.gov/search/. Last access 28-August-2023.

NATIONAL OCEANIC AND ATMOSPHERIC ADMINISTRATION GLOBAL MONITORING LABORATORY (2024). *NOAA Solar Calculator*. https://gml.noaa.gov/grad/solcalc/. Last access 7-February-2024.

NITZE, INGMAR and GUIDO GROSSE (2016). "Detection of landscape dynamics in the Arctic Lena Delta with temporally dense Landsat time-series stacks". In: *Remote Sensing of Environment* 181, pp. 27–41. DOI: 10.1016/j.rse.2016.03.038.

OBU, JAROSLAV, SEBASTIAN WESTERMANN, ANDREAS KÄÄB, and ANNETT BARTSCH (2018). *Ground Temperature Map, 2000-2016, Northern Hemisphere Permafrost*. Data set. Alfred Wegener Institute, Helmholtz Centre for Polar and Marine Research, Bremerhaven. DOI: 10.1594/PANGAEA.888600.

OVERDUIN, P. PAUL, THOMAS SCHNEIDER VON DEIMLING, FREDERIEKE MIESNER, MIKHAIL N. GRIGORIEV, CAROLYN D. RUPPEL, ALEXANDER VASILIEV, HUGUES LANTUIT, BENNET JUHLS, SEBASTIAN WESTERMANN, and SEBASTIAN LABOOR (2020). *Subma-*

rine Permafrost Map (SuPerMAP), modeled with CryoGrid 2, Circum-Arctic. Data set. Supplement to: Overduin, Pier Paul; Schneider von Deimling, Thomas; Miesner, Frederieke; Grigoriev, Mikhail N; Ruppel, Carolyn D; Vasiliev, Alexander A; Lantuit, Hugues; Juhls, Bennet; Westermann, Sebastian (2019): Submarine Permafrost Map in the Arctic Modeled Using 1-D Transient Heat Flux (SuPerMAP). Journal of Geophysical Research: Oceans, 124(6), 3490-3507, https://doi.org/10.1029/2018JC014675. DOI: 10.1594/PANGAEA.910540.

PEARSON, RICHARD G., STEVEN J. PHILLIPS, MICHAEL M. LORANTY, PIETER S. A. BECK, THEODOROS DAMOULAS, SARAH J. KNIGHT, and SCOTT J. GOETZ (2013). "Shifts in Arctic vegetation and associated feedbacks under climate change". In: *NATURE CLIMATE CHANGE* 3.7, pp. 673–677. DOI: 10.1038/NCLIMATE1858.

PITHAN, FELIX and THORSTEN MAURITSEN (2014). "Arctic amplification dominated by temperature feedbacks in contemporary climate models". In: *Nature Geoscience* 7, pp. 181–184. DOI: 10.1038/ngeo2071.

PLATNICK, STEVE, MICHAEL D. KING, and PAUL A. HUBANKS (2015). *MODIS Atmosphere L3 Daily Product. MOD08_D3*. NASA MODIS Adaptive Processing System, Goddard Space Flight Center, USA. DOI: 10.5067/MODIS/MOD08_D3.061. Last access 28-August-2023.

PLEKHANOVA, ELENA, JIN-SOO KIM, JACQUELINE OEHRI, ANGELA M. ERB, CRYSTAL B. SCHAAF, and GABRIELA SCHAEPMAN-STRUB (2022). "Mid-summer snow-free albedo across the Arctic tundra was mostly stable or increased over the past two decades". In: *Environmental Research Letters* 17.12, Art. No. 124026. DOI: 10.1088/1748-9326/aca5a1.

PORTER, CLAIRE, PAUL MORIN, IAN HOWAT, MYOUNG-JON NOH, BRIAN BATES, KENNETH PETERMAN, SCOTT KEESEY, MATTHEW SCHLENK, JUDITH GARDINER, KAREN TOMKO, MICHAEL WILLIS, COLE KELLEHER, MICHAEL CLOUTIER, ERIC HUSBY, STEVEN FOGA, HITOMI NAKAMURA, MELISA PLATSON, JR. WETHINGTON MICHAEL, CATHLEEN WILLIAMSON, GREGORY BAUER, JEREMY ENOS, GALEN ARNOLD, WILLIAM KRAMER, PETER BECKER, ABHIJIT DOSHI, CRISTELLE D'SOUZA, PAT CUMMENS, FABIEN LAURIER, and MIKKEL BOJESEN (2018). *ArcticDEM*. Version 3. Harvard Dataverse. DOI: 10.7910/DVN/OHHUKH.

POSIT TEAM (2022). *RStudio: Integrated Development Environment for R*. Version 2022.12.0.353. Posit Software, PBC. Boston, MA, USA. http://www.posit.co/.

PREVIDI, MICHAEL, KAREN L. SMITH, and LORENZO M. POLVANI (2021). “Arctic amplification of climate change: a review of underlying mechanisms”. In: *Environmental Research Letters* 16.9, Art. No. 093003. DOI: 10.1088/1748-9326/ac1c29.

PROFESSOR CRYSTAL SCHAAF'S LAB (2023). *MODIS User Guide V006 and V006.1. MCD43A1 BRDF/Albedo Model Parameters Product*. University of Massachusetts Boston, School for the Environment. Boston, MA, USA. https://www.umb.edu/spectralmass/v006/mcd43a1-brdf-albedo-model-parameters-product/. Last access 02-August-2023.

QIN, DAHE, TANDONG YAO, YONGJIAN DING, and JIAWEN REN (2021a). “Interactions Between Cryosphere and the Other Spheres”. In: *Introduction to Cryospheric Science*. Ed. by Dahe Qin, Tandong Yao, Yongjian Ding, and Jiawen Ren. Singapore, Singapore. Chap. 8, pp. 253–314. DOI: 10.1007/978-981-16-6425-0_8.

QIN, DAHE, TANDONG YAO, YONGJIAN DING, and JIAWEN REN (2021b). “Physical Properties of the Cryosphere”. In: *Introduction to Cryospheric Science*. Ed. by Dahe Qin, Tandong Yao, Yongjian Ding, and Jiawen Ren. Singapore, Singapore. Chap. 4, pp. 107–140. DOI: 10.1007/978-981-16-6425-0_4.

QU, YING, SHUNLIN LIANG, QIANG LIU, TAO HE, SUHONG LIU, and XIAOWEN LI (2015). “Mapping Surface Broadband Albedo from Satellite Observations: A Review of Literatures on Algorithms and Products”. In: *Remote Sensing* 7.1, pp. 990–1020. DOI: 10.3390/rs70100990.

R CORE TEAM (2022). *R: A Language and Environment for Statistical Computing*. Version 4.2.1. R Foundation for Statistical Computing. Vienna, Austria. https://www.R-project.org/.

RANTANEN, MIKA, ALEXEY Y. KARPECHKO, ANTTI LIPPONEN, KALLE NORDLING, OTTO HYVÄRINEN, KIMMO RUOSTEENOJA, TIMO VIHMA, and ARI LAAKSONEN (2022). “The Arctic has warmed nearly four times faster than the globe since 1979”. In: *Communications Earth & Environment* 3, Art. No. 168. DOI: 10.1038/s43247-022-00498-3.

RASCHKE, EHRHARD and ATSUMU OHMURA (2005). “Radiation budget of the climate system”. In: *Observed global climate*. Ed. by M. Hantel. Vol. 6. Group V: Geophysics, Landolt-Börnstein Numerical and Functional Relationships in Science and Technology. Chap. 4, pp. 4.1–4.42.

ROUJEAN, JEAN-LOUIS, MARC LEROY, and PIERRE-YVES DESCHAMPS (1992). “A bidirectional reflectance model of the Earth's surface for the correction of remote sens-

ing data". In: *Journal of Geophysical Research: Atmospheres* 97.D18, pp. 20455–20468. DOI: 10.1029/92JD01411.

RUDD, DANIEL A., MOJTABA KARAMI, and RASMUS FENSHOLT (2021). "Towards High-Resolution Land-Cover Classification of Greenland: A Case Study Covering Kobbefjord, Disko and Zackenberg". In: *Remote Sensing* 13.18, Art. No. 3559. DOI: 10.3390/rs13183559.

RUNGE, ALEXANDRA and GUIDO GROSSE (2019). "Comparing Spectral Characteristics of Landsat-8 and Sentinel-2 Same-Day Data for Arctic-Boreal Regions". In: *Remote Sensing* 11.14, Art. No. 1730. DOI: 10.3390/rs11141730.

SALOMON, JONATHAN G., CRYSTAL B. SCHAAF, ALAN H. STRAHLER, FENG GAO, and YUFANG JIN (2006). "Validation of the MODIS bidirectional reflectance distribution function and albedo retrievals using combined observations from the aqua and terra platforms". In: *IEEE Transactions on Geoscience and Remote Sensing* 44.6, pp. 1555–1565. DOI: 10.1109/TGRS.2006.871564.

SCHAAF, CRYSTAL B. and ZHUOSEN WANG (2021). *MODIS/Terra+Aqua BRDF/Albedo Daily L3 Global - 500m V061*. distributed by NASA EOSDIS Land Processes DAAC. DOI: 10.5067/MODIS/MCD43A3.061. Last access 9-July-2023.

SERREZE, MARK C. and ROGER G. BARRY (2014). "Physical Characteristics and Basic Climatic Features". In: *The Arctic Climate System*, pp. 23–64. DOI: 10.1017/CBO9781139583817.005.

SHUAI, YANMIN, JEFFREY G. MASEK, FENG GAO, and CRYSTAL B. SCHAAF (2011). "An algorithm for the retrieval of 30-m snow-free albedo from Landsat surface reflectance and MODIS BRDF". In: *Remote Sensing of Environment* 115.9, pp. 2204–2216. DOI: 10.1016/j.rse.2011.04.019.

SHUAI, YANMIN, JEFFREY G. MASEK, FENG GAO, CRYSTAL B. SCHAAF, and TAO HE (2014). "An approach for the long-term 30-m land surface snow-free albedo retrieval from historic Landsat surface reflectance and MODIS-based a priori anisotropy knowledge". In: *Remote Sensing of Environment* 152, pp. 467–479. DOI: https://doi.org/10.1016/j.rse.2014.07.009.

SIGSGAARD, CHARLOTTE, ed. (2022). *Guidelines and Sampling Procedures for the Geographical Monitoring Program GeoBasis Disko*. Version June 2022. Department of Geosciences and Natural Resource Management (IGN), University of Copen-

hagen. Copenhagen, Denmark. https://g-e-m.dk/fileadmin/g-e-m/GEM/GeoBasisDisko_Manual_June_2022.pdf. Last access 14-December-2023.

SONG, RUI, JAN-PETER MULLER, and ALISTAIR FRANCIS (2021). "A Method of Retrieving 10-m Spectral Surface Albedo Products from Sentinel-2 and MODIS data". In: *2021 IEEE International Geoscience and Remote Sensing Symposium IGARSS*, pp. 2381–2384. DOI: 10.1109/IGARSS47720.2021.9554356.

SONG, RUI, JAN-PETER MULLER, SAID KHARBOUCHE, and WILLIAM WOODGATE (2019). "Intercomparison of Surface Albedo Retrievals from MISR, MODIS, CGLS Using Tower and Upscaled Tower Measurements". In: *Remote Sensing* 11.6, Art. No. 644. DOI: 10.3390/rs11060644.

STRAHLER, ALAN H., WOLFGANG LUCHT, CRYSTAL B. SCHAAF, TREVOR TSANG, FENG GAO, and JAN-PETER MULLER (1999). "MODIS BRDF/Albedo Product : Algorithm Theoretical Basis Document Version 5.0". In: https://modis.gsfc.nasa.gov/data/atbd/atbd_mod09.pdf. Last access 10-July-2023.

STUENZI, SIMONE M. and GABRIELA SCHAEPMAN-STRUB (2020). "Vegetation Trajectories and Shortwave Radiative Forcing Following Boreal Forest Disturbance in Eastern Siberia". In: *Journal of Geophysical Research: Biogeosciences* 125.6, Art. No. e2019JG005395. DOI: 10.1029/2019JG005395.

TEDESCO, MARCO (2015). "Remote sensing and the cryosphere". In: *Remote Sensing of the Cryosphere*. Ed. by Marco Tedesco. Chichester, United Kingdom. Chap. 1, pp. 1–16. DOI: 10.1002/9781118368909.ch1.

THOMPSON, C., JASON BERINGER, F. STUART CHAPIN III, and ANTHONY D. MCGUIRE (2004). "Structural complexity and land-surface energy exchange along a gradient from arctic tundra to boreal forest". In: *Journal of Vegetation Science* 15.3, pp. 397–406. DOI: 10.1111/j.1654-1103.2004.tb02277.x.

TILSTRA, LIEUWE G., OLAF N. E. TUINDER, PING WANG, and PIET STAMMES (2021). "Directionally dependent Lambertian-equivalent reflectivity (DLER) of the Earth's surface measured by the GOME-2 satellite instruments". In: *Atmospheric Measurement Techniques* 14.6, pp. 4219–4238. DOI: 10.5194/amt-14-4219-2021.

TOMASI, CLAUDIO, BOYAN H. PETKOV, ANGELO LUPI, MAURO MAZZOLA, CHRISTIAN LANCONELLI, and ISMAIL GULTEPE (2020). "Radiation in the Arctic Atmosphere and Atmosphere – Cryosphere Feedbacks". In: *Physics and Chemistry of the Arctic Atmo-*

sphere. Ed. by Alexander Kokhanovsky and Claudio Tomasi. Cham, Switzerland. Chap. 10, pp. 591–672. DOI: 10.1007/978-3-030-33566-3_10.

TRAVERSA, GIACOMO, DAVIDE FUGAZZA, ANTONELLA SENESE, and MASSIMO FREZZOTTI (2021). "Landsat 8 OLI Broadband Albedo Validation in Antarctica and Greenland". In: *Remote Sensing* 13.4, Art. No. 799. DOI: 10.3390/rs13040799.

USGS (2019). *Landsat 8 (L8) Data Users Handbook*. https://d9-wret.s3.us-west-2.amazonaws.com/assets/palladium/production/s3fs-public/atoms/files/LSDS-1574_L8_Data_Users_Handbook-v5.0.pdf. Last access 9-July-2023.

USGS (2022). *EarthExplorer*. https://earthexplorer.usgs.gov/. Courtesy of the U.S. Geological Survey. Last access 16-July-2023.

VERMOTE, ERIC F., DIDIER TANRE, JEAN-LUC DEUZE, MAURICE HERMAN, and JEAN-JACQUES MORCETTE (1997). "Second Simulation of the Satellite Signal in the Solar Spectrum, 6S: an overview". In: *IEEE Transactions on Geoscience and Remote Sensing* 35.3, pp. 675–686. DOI: 10.1109/36.581987.

VICENT, JORGE, JOCHEM VERRELST, NEUS SABATER, LUIS ALONSO, JUAN P. RIVERA-CAICEDO, LUCA MARTINO, JORDI MUÑOZ-MARÍ, and JOSÉ MORENO (2020). "Comparative analysis of atmospheric radiative transfer models using the Atmospheric Look-up table Generator (ALG) toolbox (version 2.0)". In: *Geoscientific Model Development* 13.4, pp. 1945–1957. DOI: 10.5194/gmd-13-1945-2020.

WALSH, JOHN E. (2021). "Arctic Climate Change, Variability, and Extremes". In: *Arctic Hydrology, Permafrost and Ecosystems*. Ed. by Daqing Yang and Douglas L. Kane. Cham, Switzerland. Chap. 1, pp. 3–23. DOI: 10.1007/978-3-030-50930-9_1.

WANG, WENSHAN, CHARLES S. ZENDER, DIRK VAN AS, PAUL C. J. P. SMEETS, and MICHIEL R. VAN DEN BROEKE (2016). "A Retrospective, Iterative, Geometry-Based (RIGB) tilt-correction method for radiation observed by automatic weather stations on snow-covered surfaces: application to Greenland". In: *The Cryosphere* 10.2, pp. 727–741. DOI: 10.5194/tc-10-727-2016.

WANG, ZHUO, MICHAEL BARLAGE, XUBIN ZENG, ROBERT E. DICKINSON, and CRYSTAL B. SCHAAF (2005). "The solar zenith angle dependence of desert albedo". In: *Geophysical Research Letters* 32.5, Art. No. L05403. DOI: 10.1029/2004GL021835.

WANG, ZHUOSEN, ANGELA M. ERB, CRYSTAL B. SCHAAF, QINGSONG SUN, YAN LIU, YUN YANG, YANMIN SHUAI, KIMBERLY A. CASEY, and MIGUEL O. ROMÁN (2016). "Early spring post-fire snow albedo dynamics in high latitude boreal forests using Landsat-

8 OLI data". In: *Remote Sensing of Environment* 185, pp. 71–83. DOI: 10.1016/j.rse.2016.02.059.

WANG, ZHUOSEN, CRYSTAL B. SCHAAF, MARK J. CHOPPING, ALAN H. STRAHLER, JINDI WANG, MIGUEL O. ROMÁN, ADRIAN V. ROCHA, CURTIS E. WOODCOCK, and YANMIN SHUAI (2012). "Evaluation of Moderate-resolution Imaging Spectroradiometer (MODIS) snow albedo product (MCD43A) over tundra". In: *Remote Sensing of Environment* 117, pp. 264–280. DOI: 10.1016/j.rse.2011.10.002.

WANNER, WILLIAM, X. LI, and ALAN H. STRAHLER (1995). "On the derivation of kernels for kernel-driven models of bidirectional reflectance". In: *Journal of Geophysical Research: Atmospheres* 100.D10, pp. 21077–21089. DOI: 10.1029/95JD02371.

WANNER, WILLIAM, ALAN H. STRAHLER, B. HU, PHILIP E. LEWIS, JAN-PETER MULLER, X. LI, CRYSTAL B. SCHAAF, and MICHAEL J. BARNSLEY (1997). "Global retrieval of bidirectional reflectance and albedo over land from EOS MODIS and MISR data: Theory and algorithm". In: *Journal of Geophysical Research: Atmospheres* 102.D14, pp. 17143–17161. DOI: 10.1029/96JD03295.

WEN, GUOYONG, ALEXANDER MARSHAK, WANJUAN SONG, YURI KNYAZIKHIN, MATTI MÕTTUS, and DONG WU (2019). "A Relationship Between Blue and Near-IR Global Spectral Reflectance and the Response of Global Average Reflectance to Change in Cloud Cover Observed From EPIC". In: *Earth and Space Science* 6.8, pp. 1416–1429. DOI: 10.1029/2019EA000664.

WENDISCH, MANFRED, ANDRÉ EHRLICH, and PETER PILEWSKIE (2021). "Satellite and Aircraft Remote Sensing Platforms". In: *Springer Handbook of Atmospheric Measurements*. Ed. by Thomas Foken. Cham, Switzerland. Chap. 37, pp. 1053–1066. DOI: 10.1007/978-3-030-52171-4_37.

WESTERMANN, SEBASTIAN, CLAUDE R. DUGUAY, GUIDO GROSSE, and ANDREAS KÄÄB (2015). "Remote sensing of permafrost and frozen ground". In: *Remote Sensing of the Cryosphere*. Ed. by Marco Tedesco. Chichester, United Kingdom. Chap. 13, pp. 307–344. DOI: 10.1002/9781118368909.ch13.

WILLIAMSON, ANDREW G., ALISON F. BANWELL, IAN C. WILLIS, and NEIL S. ARNOLD (2018). "Dual-satellite (Sentinel-2 and Landsat 8) remote sensing of supraglacial lakes in Greenland". In: *The Cryosphere* 12.9, pp. 3045–3065. DOI: 10.5194/tc-12-3045-2018.

WILLIAMSON, SCOTT N., ISABEL C. BARRIO, DAVID S. HIK, and JOHN A. GAMON (2016). "Phenology and species determine growing-season albedo increase at the altitudinal limit of shrub growth in the sub-Arctic". In: *Global Change Biology* 22.11, pp. 3621–3631. DOI: doi.org/10.1111/gcb.13297.

WORLD METEOROLOGICAL ORGANIZATION (2018). *Guide to Instruments and Methods of Observation, Volume I – Measurement of Meteorological Variables*. Geneva, Switzerland.

WU, SHENGBIAO, JIANGUANG WEN, DONGQIN YOU, DALEI HAO, XINGWEN LIN, QING XIAO, QINHUO LIU, and JEAN-PHILIPPE GASTELLU-ETCHEGORRY (2018). "Characterization of Remote Sensing Albedo Over Sloped Surfaces Based on DART Simulations and In Situ Observations". In: *Journal of Geophysical Research: Atmospheres* 123.16, pp. 8599–8622. DOI: 10.1029/2018JD028283.

WUTTKE, SIGRID, GUNTHER SECKMEYER, and GERT KÖNIG-LANGLO (2006). "Measurements of spectral snow albedo at Neumayer, Antarctica". In: *Annales Geophysicae* 24.1, pp. 7–21. DOI: 10.5194/angeo-24-7-2006.

YANG, GANG, JIYAN WANG, JUNNAN XIONG, ZHIWEI YONG, CHONGCHONG YE, HUAIZHANG SUN, JUN LIU, YU DUAN, YUFENG HE, and WEN HE (2021). "An Algorithm for the Retrieval of High Temporal-Spatial Resolution Shortwave Albedo from Landsat-8 Surface Reflectance and MODIS BRDF". In: *Remote Sensing* 13.20, Art. No. 4150. DOI: 10.3390/rs13204150.

YANG, JIAN, YANMIN SHUAI, JUNBO DUAN, DONGHUI XIE, QINGLING ZHANG, and RUISHAN ZHAO (2022). "Impact of BRDF Spatiotemporal Smoothing on Land Surface Albedo Estimation". In: *Remote Sensing* 14.9, Art. No. 2001. DOI: 10.3390/rs14092001.

ZHANG, HU, ZITI JIAO, LEI CHEN, YADONG DONG, XIAONING ZHANG, YI LIAN, DA QIAN, and TIEJUN CUI (2018). "Quantifying the Reflectance Anisotropy Effect on Albedo Retrieval from Remotely Sensed Observations Using Archetypal BRDFs". In: *Remote Sensing* 10.10, Art. No. 1628. DOI: 10.3390/rs10101628.

ZHANG, TINGJUN, J. ALAN HEGINBOTTOM, ROGER G. BARRY, and JERVON BROWN (2000). "Further statistics on the distribution of permafrost and ground ice in the Northern Hemisphere". In: *Polar Geography* 24.2, pp. 126–131. DOI: 10.1080/10889370009377692.

ZHANG, WENXIN, PER-ERIK JANSSON, CHARLOTTE SIGSGAARD, ALISTAIR MCCONNELL, MATHILDE MANON JAMMET, ANDREAS WESTERGAARD-NIELSEN, MAGNUS LUND, THO-

MAS FRIBORG, ANDERS MICHELSEN, and BO ELBERLING (2019). “Model-data fusion to assess year-round CO2 fluxes for an arctic heath ecosystem in West Greenland (69°N)”. In: *Agricultural and Forest Meteorology* 272–273, pp. 176–186. DOI: 10.1016/j.agrformet.2019.02.021.

A Appendices

A.1 List of Equations

BRDF Model

$$R_\lambda(\Theta_s,\Theta_v,\phi) = f_{iso,\lambda} + f_{vol,\lambda}\cdot K_{vol}(\Theta_s,\Theta_v,\phi) + f_{geo,\lambda}\cdot K_{geo}(\Theta_s,\Theta_v,\phi) \tag{1}$$

Equal Albedo to Nadir Reflectance Ratios

$$\bar{\alpha}_\lambda \approx \frac{\alpha_{m,\lambda}}{R_{m,\lambda}} \approx \frac{\alpha_{lan,\lambda}}{R_{lan,\lambda}} \approx \frac{\alpha_{sen,\lambda}}{R_{sen,\lambda}} \tag{2}$$

Footprint Diameter of Pyranometers

$$\varnothing_{footprint} = 2\cdot h\cdot \tan(\frac{FoV}{2}) \tag{3}$$

MODIS Nadir Reflectance

$$R_{\lambda,m}(\Omega_{lan/sen}) = R_\lambda(\Theta_s = \Theta_{s,lan/sen}, \Theta_v = 0, \phi = 0) \tag{4}$$

RossThick Kernel

$$K_{vol} = \frac{(\pi/2-\xi)\cos\xi + \sin\xi}{\cos\Theta_s + \cos\Theta_v} - \frac{\pi}{4} \tag{5}$$

with

$$\cos\xi = \cos\Theta_s\cdot\cos\Theta_v + \sin\Theta_s\cdot\sin\Theta_v\cdot\cos\phi \tag{6}$$

LiSparse kernel

$$\begin{aligned} K_{geo} = {} & O(\Theta_s,\Theta_v,\phi) - \sec\Theta_s - \sec\Theta_v \\ & + \frac{1}{2}\cdot(1+\cos\xi)\cdot\sec\Theta_s\cdot\sec\Theta_v \end{aligned} \tag{7}$$

with

$$O = \frac{1}{\pi}\cdot(t - \sin t\cdot\cos t)\cdot(\sec\Theta_s + \sec\Theta_v) \tag{8}$$

$$\cos t = \frac{h}{b}\cdot\frac{\sqrt{D^2 + (\tan\Theta_s\cdot\tan\Theta_v\cdot\sin\phi)^2}}{\sec\Theta_s + \sec\Theta_v} \tag{9}$$

$$D = \sqrt{\tan^2\Theta_s + \tan^2\Theta_v - 2\cdot\tan\Theta_s\cdot\tan\Theta_v\cdot\cos\phi} \tag{10}$$

MODIS Black Sky Albedo

$$\begin{aligned}\alpha_{bs,m,\lambda}(\Theta_{s,lan/sen}) = f_{iso,\lambda}\cdot(g_{0iso} + g_{1iso}\cdot\Theta^2_{s,lan/sen} + g_{2iso}\cdot\Theta^3_{s,lan/sen}) + \\ f_{vol,\lambda}\cdot(g_{0vol} + g_{1vol}\cdot\Theta^2_{s,lan/sen} + g_{2vol}\cdot\Theta^3_{s,lan/sen}) + \\ f_{geo,\lambda}\cdot(g_{0geo} + g_{1geo}\cdot\Theta^2_{s,lan/sen} + g_{2geo}\cdot\Theta^3_{s,lan/sen})\end{aligned} \tag{11}$$

MODIS White Sky Albedo

$$\alpha_{ws,m,\lambda} = f_{iso,\lambda}\cdot g_{iso} + f_{vol,\lambda}\cdot g_{vol} + f_{geo,\lambda}\cdot g_{geo} \tag{12}$$

Black Sky A/N ratio

$$\bar{\alpha}_{bs,m,\lambda}(\Omega_{lan/sen}) = \frac{\alpha_{bs,m,\lambda}(\Theta_{s,lan/sen})}{R_{m,\lambda}(\Omega_{lan/sen})} \tag{13}$$

White Sky A/N ratio

$$\bar{\alpha}_{ws,m,\lambda}(\Omega_{lan/sen}) = \frac{\alpha_{ws,m,\lambda}}{R_{m,\lambda}(\Omega_{lan/sen})} \tag{14}$$

Landsat/Sentinel Black Sky Albedo

$$\alpha_{bs,lan/sen,\lambda} = \bar{\alpha}_{bs,m,\lambda}(\Omega_{lan/sen})\cdot R_{lan/sen,\lambda} \tag{15}$$

Landsat/Sentinel White Sky Albedo

$$\alpha_{ws,lan/sen,\lambda} = \bar{\alpha}_{ws,m,\lambda}(\Omega_{lan/sen})\cdot R_{lan/sen,\lambda} \tag{16}$$

Landsat/Sentinel Narrow Band Blue Sky Albedo

$$\alpha_{lan/sen,\lambda} = \alpha_{bs,lan/sen,\lambda}\cdot dir_\lambda + \alpha_{ws,lan/sen,\lambda}\cdot(1 - dir_\lambda) \tag{17}$$

Landsat Broadband Blue Sky Albedo

$$\begin{aligned}\alpha_{lan} = \alpha_{lan,b2} \cdot 0.2453 + \alpha_{lan,b3} \cdot 0.0508 + \alpha_{lan,b4} \cdot 0.1804 + \\ \alpha_{lan,b5} \cdot 0.3081 + \alpha_{lan,b6} \cdot 0.1332 + \\ \alpha_{lan,b7} \cdot 0.0521 + 0.0011\end{aligned} \tag{18}$$

Sentinel Broadband Blue Sky Albedo

$$\begin{aligned}\alpha_{sen} = \alpha_{sen,b2} \cdot 0.2688 + \alpha_{sen,b3} \cdot 0.0362 + \alpha_{sen,b4} \cdot 0.1501 + \\ \alpha_{sen,b8} \cdot 0.3045 + \alpha_{sen,b11} \cdot 0.1644 + \\ \alpha_{sen,b12} \cdot 0.0356 - 0.0049\end{aligned} \tag{19}$$

Landsat Broadband Nadir Reflectance

$$\begin{aligned}R_{lan}(\Theta_v = 0) = SR_{lan,b2} \cdot 0.356 + SR_{lan,b4} \cdot 0.130 + SR_{lan,b5} \cdot 0.373 + \\ SR_{lan,b6} \cdot 0.085 + SR_{lan,b7} \cdot 0.072 - 0.0018\end{aligned} \tag{20}$$

Sentinel Broadband Nadir Reflectance

$$\begin{aligned}R_{sen}(\Theta_v = 0) = SR_{sen,b2} \cdot 0.2266 + SR_{sen,b3} \cdot 0.1236 + SR_{sen,b4} \cdot 0.1573 + \\ SR_{sen,b8A} \cdot 0.3417 + SR_{sen,b11} \cdot 0.1170 + SR_{sen,b12} \cdot 0.0338\end{aligned} \tag{21}$$

Indices

$$NDMI = \frac{NIR - SWIR1}{NIR + SWIR1} \tag{22}$$

$$NDVI = \frac{NIR - RED}{NIR + RED} \tag{23}$$

$$NDWI = \frac{Green - NIR}{Green + NIR} \tag{24}$$

RMSE

$$RMSE = \sqrt{\frac{\sum_{i=1}^{n} (\alpha_i - \hat{\alpha}_i)^2}{n}} \tag{25}$$

Mean Absolute Deviation

$$d = \frac{\sum_{i=1}^{n} |\hat{\alpha}_i - \alpha_{AWS}|}{n} \tag{26}$$

A.2 Additional Tables

Table 8: Satellite bands and wavelength of used data products (USGS 2019; ESA 2015; LP DAAC n.d.).

	Landsat 8			**Sentinel 2**			**MODIS**		
band	band	wavelength		band	wavelength		band	wavelength	
name	no.	central (nm)	bandwidth (nm)	no.	central (nm)	bandwidth (nm)	no.	central (nm)	bandwidth (nm)
blue	2	482	60	2	490	65	3	469	20
green	3	562	57	3	560	35	4	555	20
red	4	655	37	4	665	30	1	645	50
NIR	5	865	28	8A	865	21	2	859	35
SWIR1	6	1609	85	11	1610	90	6	1640	24
SWIR2	7	2201	187	12	2190	180	7	2130	50

Table 9: Input variables and direct radiation fraction output of the 6S simulations. I set the view zenith and relative azimuth angles to 0 ° and selected a marine aerosol model for all simulations. Italic AOT values refer to the selected global average, when no good MODIS data were available. I ran the simulations for the L8 and S2 bands, defined by their minimum and maximum wavelength. The output included a number of parameters. Here only the relevant direct solar radiation fraction is listed. Data: LEVY et al. (2015), PLATNICK et al. (2015), USGS (2019), and ESA (2015).

Scene		**Input**				**Output: direct solar radiation fraction**					
product	date as YYYY-MM-DD	AOT at 550 nm	ozone in atm-cm	water vapor in g/cm^2	Θ_s in degree	blue	green	red	NIR	SWIR1	SWIR2
L8	2022-06-28	*0.120*	0.389	1.890	46.4	0.692	0.762	0.804	0.845	0.879	0.901
S2	2022-06-28	*0.120*	0.389	1.890	45.6	0.706	0.764	0.810	0.846	0.881	0.902
L8	2022-07-05	*0.120*	0.376	0.988	47.0	0.690	0.760	0.803	0.843	0.870	0.900
S2	2022-07-08	0.059	0.398	1.449	46.5	0.766	0.828	0.876	0.911	0.937	0.949
L8	2022-07-14	*0.120*	0.371	1.285	48.1	0.686	0.757	0.800	0.841	0.876	0.898
S2	2022-07-14	*0.120*	0.371	1.285	47.3	0.700	0.759	0.806	0.843	0.878	0.900
S2	2022-07-15	*0.120*	0.404	1.214	47.5	0.699	0.758	0.805	0.842	0.878	0.899
L8	2022-07-16	*0.120*	0.422	1.063	48.4	0.685	0.756	0.799	0.840	0.876	0.898
S2	2022-07-31	0.198	0.349	1.632	50.7	0.610	0.667	0.714	0.753	0.799	0.833
L8	2022-08-01	*0.120*	0.349	1.429	51.8	0.670	0.744	0.789	0.832	0.869	0.892
S2	2022-08-03	*0.120*	0.380	1.621	51.5	0.683	0.745	0.794	0.833	0.870	0.893
L8	2022-08-24	*0.120*	0.373	0.855	58.7	0.631	0.713	0.762	0.810	0.851	0.877
S2	2022-08-28	0.124	0.414	1.059	59.4	0.634	0.703	0.758	0.802	0.845	0.872
S2	2022-09-04	*0.120*	0.314	2.020	62.0	0.619	0.692	0.750	0.796	0.840	0.868

A.3 Additional Figures

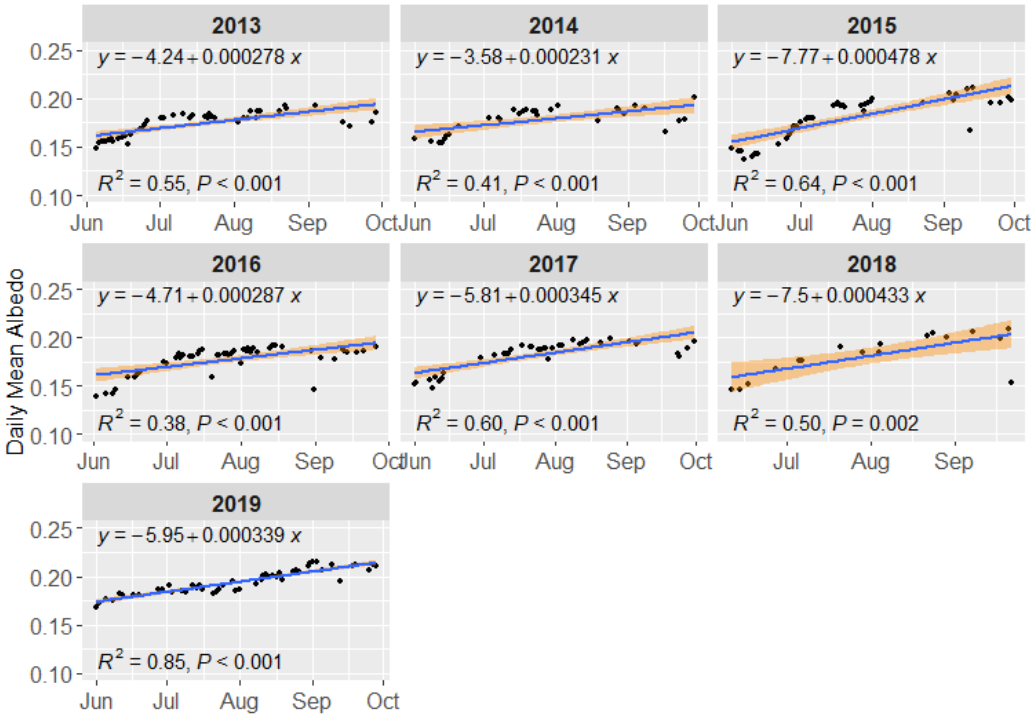

(a) Cloud cover < 30 % at noon.

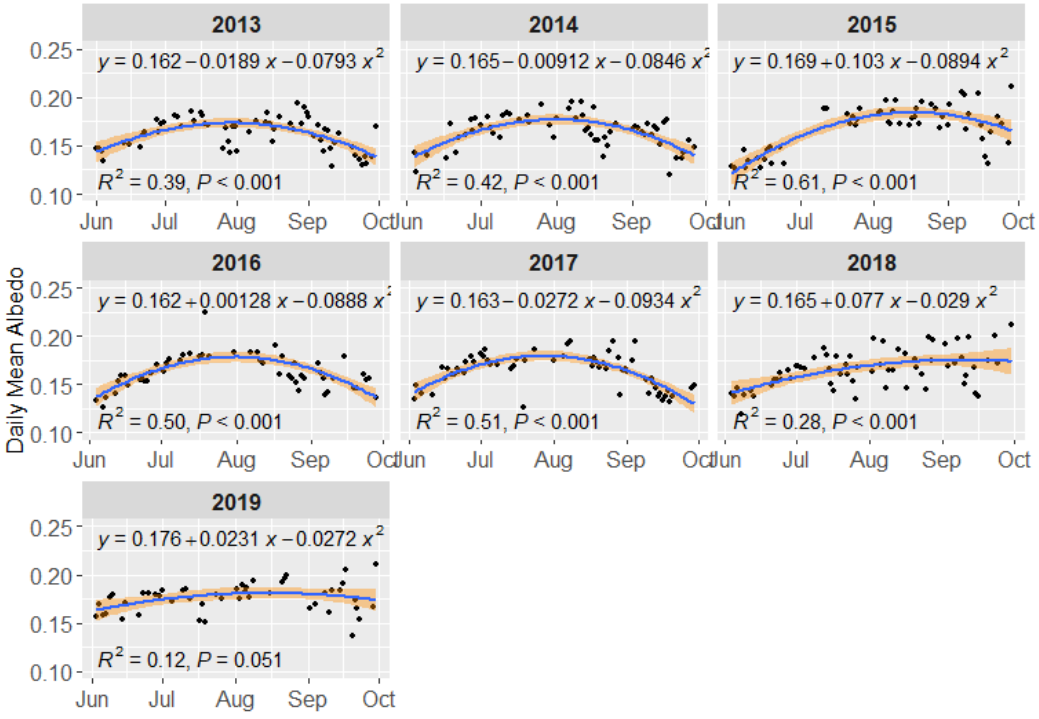

(b) Cloud cover > 70 % at noon.

Figure 19: Daily mean albedo at AWS2 (black points) in the snow-free period with low and high cloud cover. The equation, R^2 and P describe the smoothing (blue line) and its quality. The 95 % confidence interval is displayed in orange. Data: GEM (2023c) and GEM (2023b).

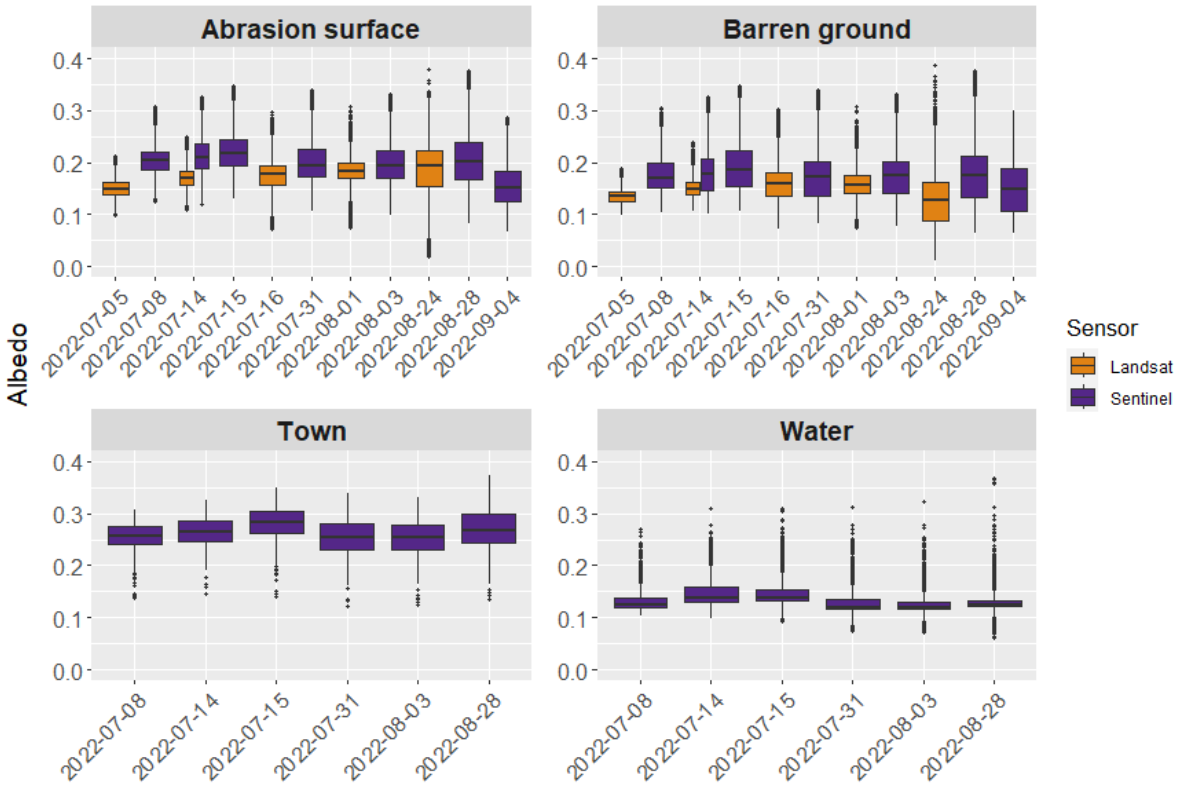

Figure 20: Albedo boxplots for non-vegetated classes > 1000 pixels after outlier removal in 2022. The box represents the first and third quartile with the median as the middle line. The whiskers indicate the minimum and maximum values within the 1.5-times IQR distance to the boxes. The points are outliers beyond that range.

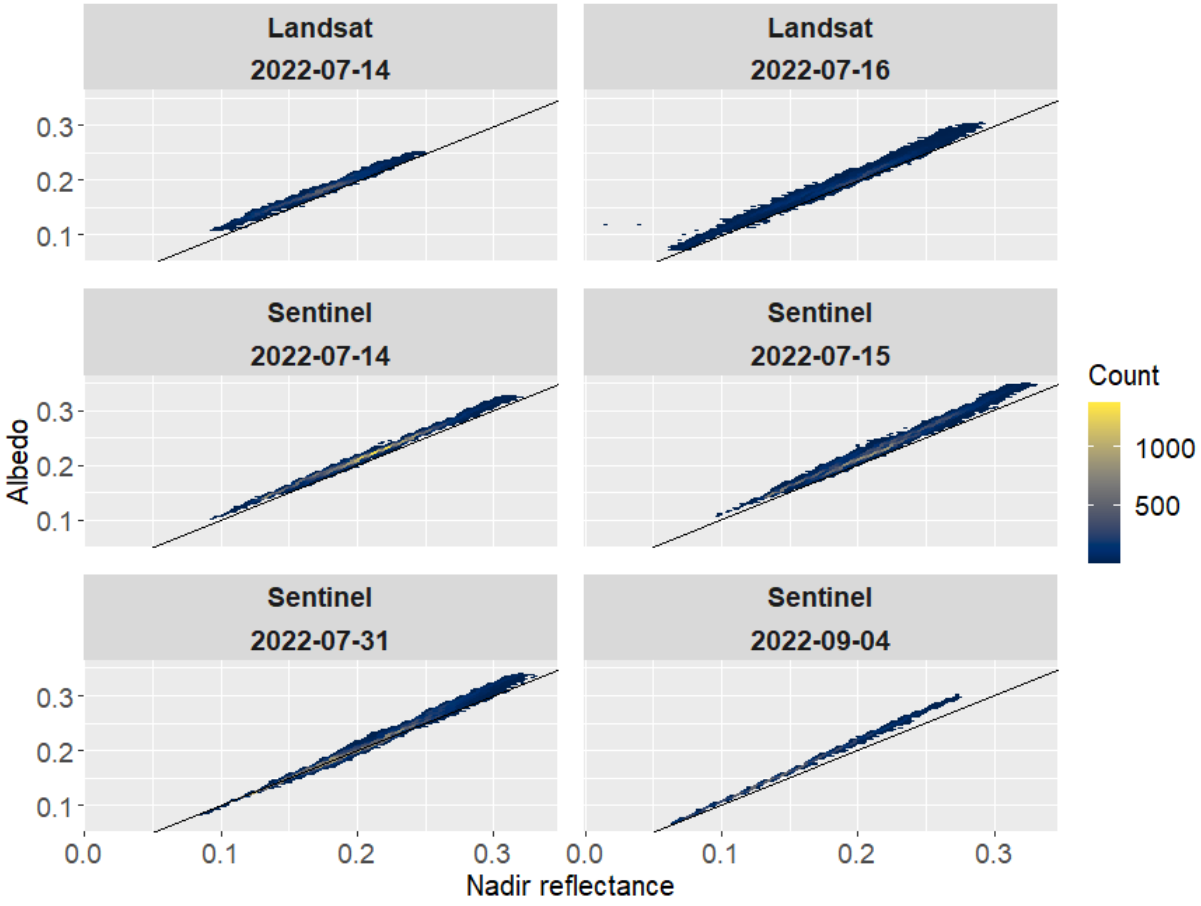

Figure 21: Scatterplots of albedo and nadir reflectance for additional dates. The black line indicates where $\alpha = R(\Theta_v = 0)$.

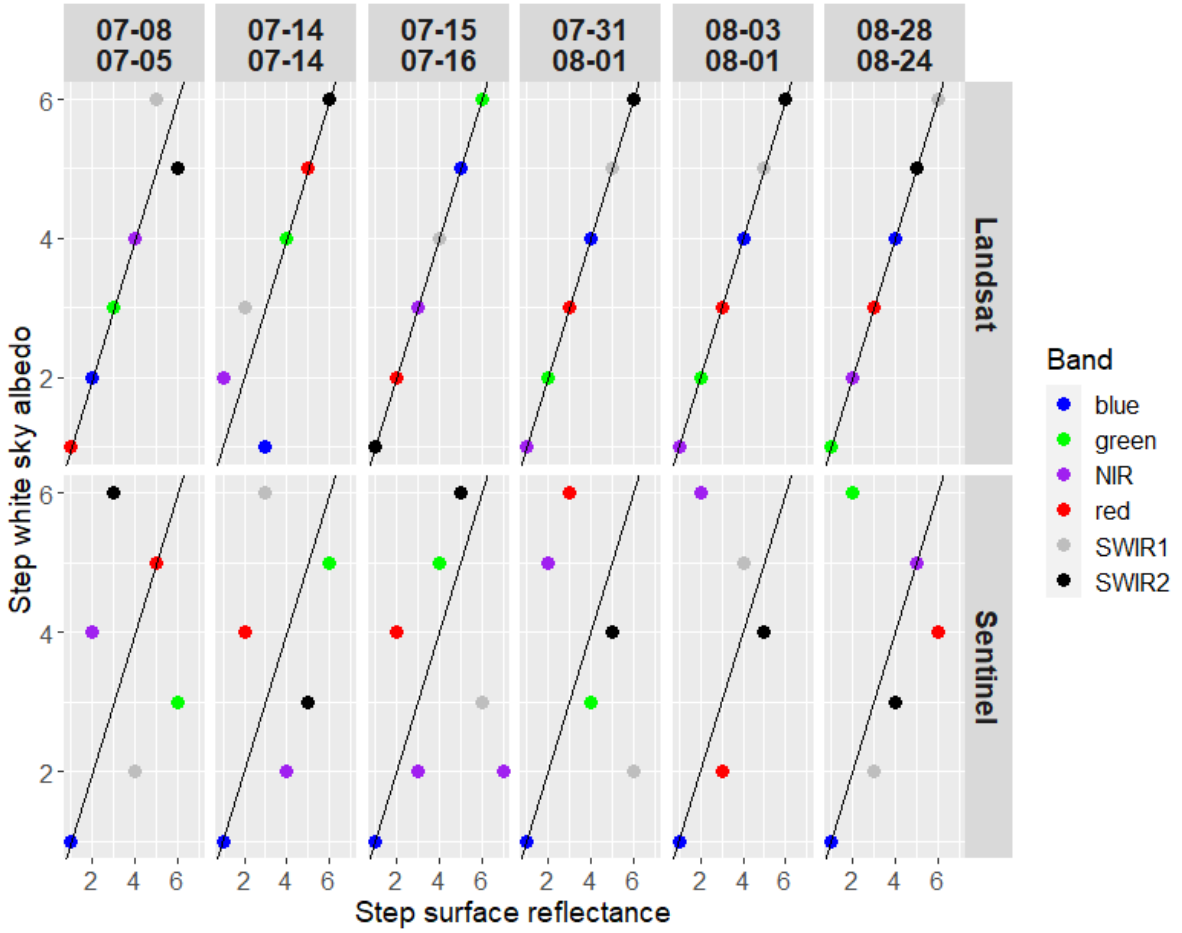

Figure 22: Comparison of surfaces reflectance and white sky albedo steps in step-wise multiple regression analysis of the albedo differences in 2022. In the separate models, the differences are explained by the sensors band-wise surface reflectance or white sky albedo. In the top of the figure, the two compared dates are given in the format month-day, with the S2 date above the L8 date. In the surface reflectance model of S2 of 15th and 16th July, the NIR band was removed from the model in the 7th step so that it appears twice.

Versicherung an Eides statt

Hiermit versichere ich an Eides statt, dass ich die vorliegende Arbeit im Studiengang M.Sc. Geographie selbstständig verfasst und keine anderen als die angegebenen Hilfsmittel – insbesondere keine im Quellenverzeichnis nicht benannten Internet-Quellen – benutzt habe. Alle Stellen, die wörtlich oder sinngemäß aus Veröffentlichungen entnommen wurden, sind als solche kenntlich gemacht. Ich versichere weiterhin, dass ich die Arbeit vorher nicht in einem anderen Prüfungsverfahren eingereicht habe.

Einer Veröffentlichung der vorliegenden Arbeit in der zuständigen Fachbibliothek des Fachbereichs stimme ich nicht zu.

Hamburg, 09.02.2024